MOLECULE TRANSPORT IN NANOPORES WITH APPLICATIONS TO WATER PURIFICATION, POWER GENERATION AND DISEASE DIAGNOSIS

BY

MOHAMMAD HEIRANIAN

DISSERTATION

Submitted in partial fulfillment of the requirements
for the degree of Doctor of Philosophy in Theoretical and Applied Mechanics
in the Graduate College of the
University of Illinois at Urbana-Champaign, 2020

Urbana, Illinois

Doctoral Committee:

Professor Narayana R. Aluru, Chair
Professor Rashid Bashir
Professor SungWoo Nam
Professor Diwakar Shukla

Abstract

High performance water transport in nanopores has drawn a great deal of attention in a variety of applications, such as water desalination, power generation and biosensing. A single-layer MoS_2 nanopore is shown, here, to possess high water transport rate and strong salt rejection rate making it ideal for water desilation. High water transport enhancement factors in carbon-based nanopores have been reported over the classical Hagen-Poiseuille (HP) equation which does not account for the physics of transport at molecular scale. Instead, comparing the experimentally measured transport rates to that of a theory, that accounts for the microscopic physics of transport, would result in enhancement factors approaching unity. Here, molecular corrections are introduced into HP equation by considering the variation of key hydrodynamical properties (viscosity and friction) with thickness and diameter of pores in ultrathin graphene and finite-length carbon nanotubes (CNTs) using Green-Kubo relations and molecular dynamics (MD) simulations. The corrected HP (CHP) theory, successfully predicts the permeation rates from non-equilibrium MD pressure driven flows. The previously reported enhancement factors over no-slip HP (of the order of 1000) approach unity when the permeations are normalized by the CHP flow rates.

In a follow-up study, we revisit Sampson's theory after more than a century to account for the surface chemistry of nanopores by incorporating slippage and interfacial viscosity variation into the original Sampson's theory. The HP theory works for flow in infinitely long tubes where end effects are neglected. In 1891, Ralph Allen Sampson came up with a formula, known as Sampson formula, within the fluid mechanics framework to describe flow in an infinitesimally thin orifice. Zeev Dagan, Sheldon Weinbaum and Robert Pfeffer published an article in the *Journal of Fluid Mechanics* in 1982, where the HP and Sampson formulas were combined to successfully describe flow in circular tubes of finite length.

Although the Sampson formula is a powerful theory for end effects, it has been shown to lack accuracy for relatively small-radius pores (e.g., nanopores in single-layer graphene membranes) since it does not account for the molecular interface chemistry. We show that the corrected Sampson's theory is able to accurately describe flow in ultrathin nanopores when compared to the data from molecular dynamics simulations. Combining our corrected Sampson formula with the HP equation, we can remarkably predict flow in not only ultrathin pores but also finite-length pores such as carbon nanotubes.

We also explored the structure and dynamics of aqueous ions in nanopores. At the nanopore interfaces, properties of ions are shown to differ largely from those of predicted by the classical ionic layering models (e.g., Gouy-Chapman electric double layer (EDL)) when the thickness of the nanopore is scaled down to the limit of ultrathin membranes (e.g, single-layer graphene). Here, using extensive molecular dynamics, the structure and dynamics of aqueous ions inside nanopores are studied for different thicknesses, diameters and surface charge densities of carbon-based nanopores (ultrathin graphene and finite-length carbon nanotubes (CNTs)). The ion concentration and diffusion coefficient in ultrathin nanopores show no indication of Stern layer formation (an immobile counter-ionic layer) as the counter-ions and nanopore atoms are weakly correlation with time compared to the strong correlation in thick nanopores. Adsorption constants of counter-ions onto the nanopore surface are shown to be many orders of magnitudes smaller than that of thick nanopores. The vanishing counter-ion adsorption in ultrathin nanopores explains the lack of Stern layer formation leading to fast dynamics of ions with picosecond scale residence times.

Finally, we investigated DNA transport through biological nanopores. Distinguishing bases of nucleic acids by passing them through nanopores has so far primarily relied on electrical signals – specifically, ionic currents through the nanopores. However, the low signal-to-noise ratio makes detection of ionic currents difficult. We show that the initially closed Mechano-Sensitive Channel of Large Conductance (MscL) protein pore opens for single stranded DNA (ssDNA) translocation under an applied electric field. As each nucleotide translocates through the pore, a unique mechanical signal is observed – specifically,

the tension in the membrane containing the MscL pore is different for each nucleotide. In addition to the membrane tension, we found that the ionic current is also different for the 4 nucleotide types. The initially closed MscL adapts its opening for nucleotide translocation due to the flexibility of the pore. This unique operation of MscL provides single nucleotide resolution in both electrical and mechanical signals.

To my family and friends

Acknowledgements

I would like to gratefully thank my adviser, Professor Narayana R. Aluru, for his tremendous supervision and guidance. Nothing could have been achieved without his critical and scientific assessment of my work. I also appreciate the time, encouragement and support he has always offered me throughout my graduate years. My special thanks are extended to Professor Emad Tajkhorshid, and Professor Diwakar Shukla for their time and thoughtful feedback.

I would also like to thank Professor Rashid Bashir, Professor SungWoo Nam, Professor Amir Barati Farimani, Professor Aleksandra Radenovic, Professor Andy Sarles, and Professor Nadia Mason for their wonderful guidance and collaborations.

I am also very thankful for the great support I received from the Computational Multiscale Nanosystems group during my Ph.D.

I would like to acknowledge the financial support by AFOSR, NSF, DOE and the Beckman Institute for Advanced Science and Technology. I also need to acknowledge the use of the parallel computing resource Blue Waters provided by the University of Illinois and National Center for Supercomputing Applications (NCSA).

I am deeply thankful to my loving and supporting partner Melissa, parents Abbas and Touba, and my siblings Mehdi, Maliheh, Vajiheh and Farzaneh. Their unconditional love and support have always kept me advancing towards my goals.

TABLE OF CONTENTS

CHAPTER 1: Introduction

1.1 Nanopore Technology

Nanopores are pores of nanometer size in membranes. Nanopores are abundantly found in biological protein pores (*e.g.*, MspA, MscL and alpha-hemolysin) embedded within a lipid bilayer. Nanopores can also be fabricated by creating a nanometer-diameter hole in synthetic materials (*e.g.*, graphene, molybdenum disulfide (MoS_2) and silicon). Thanks to the ultra-small size of nanopores, single molecules (*e.g.*,water, ions, DNA and biological molecules) can be transported through the pores. The single molecule transport in nanopores has opened up opportunities to design energy-efficient membranes for water desalination[1], power generation[2] and biomolecule detection[3-5]. As the diameter of the nanopore approaches the size of the hydrated ions, various types of ions can be rejected by nanoporous membranes promising efficient water desalination. When nanopores in ultrathin membranes are used, ultra-fast water transport is achieved leading to high performance and efficient water desalination. Power generation from the chemical potential gradient between seawater and river water is a clean method of harvesting energy known as “blue energy”. Under a chemical potential gradient resulting from a salt gradient, power is generated when electrolytes diffuse down the gradient through selective (charged) nanoporous membranes. Because of the selectivity, more counter-ions diffuse across the nanopores resulting in a net electric current. Nanopores in ultrathin materials are preferable as flux scales inversely with the thickness of the membrane. In recent years, nanopore-sequencing technology has matured to an extent where it is now used in the industry (e.g. Oxford Nanopore, Genia) as a long-read, single base resolution, and label-free detection platform. The parallel use of thousands of pores and the ability to read a chain of DNA thousands of times empower the sequencing technology with single base resolution. Specifically, with the advances in data alignment, machine learning and data processing, the fast and long-read sequencing features obtained from the nanopore-sequencing technology have become practicable since multiple readings and statistical learning can alleviate the problem of noise in detection.[6-10] Ionic current and residence time (signal bandwidth) of each base in the nanopore are the primary detection signatures, which are used as features in data classification.[11-13] However, the fact that these signals overlap with each other for different DNA bases, has inspired scientists to propose other signal types or to functionalize the existing nanopores and discover new materials for improved signal resolution.[3,14] The conventional Si_3N_4 pore and other solid state nanopores have a thickness of several nanometers[7] limiting the single base recognition of biological molecules.[8,11] The thickness of these membranes results in the encapsulation of multiple DNA/amino acid bases/residues, making it difficult to decompose the signal associated with each base.[4,15-18] Therefore, nanopores in ultrathin membranes are promising candidates to improve the signal as a single DNA/amino acid residue can be encapsulated within thin nanopores.

1.2 Structure of the Dissertation

The current thesis is consists of five studies for transport of water, ions and DNA molecules through nanopores. Each chapter includes a separate section for introduction, methods, results and discussion, and conclusion of the study. Appendix (A, B, C, D and E) contains supporting details for the materials discussed in the main chapters of the thesis.

In the second chapter, Molybdenum Disulphide (MoS_2) single layer membrane is introduced as a promising material for water desalination. Nanopores in MoS_2 result in very fast water transport rates while the ions are rejected effectively. In the third chapter, the effect of thickness and diameters of nanopores in carbon-based membranes (graphene and carbon nanotubes (CNTs)) on the hydrodynamical properties is studied. The scaling behavior is then employed to correct the Hagen-Poiseuille (HP) theory for flow in circular nanopores. In the fourth chapter, Sampson's theory for the hydrodynamic resistance across a zero-length orifice, which was developed over a century ago, is revisited and corrected for the finite slippage and interfacial viscosity variation near the pore wall. The corrected Sampson's theory can accurately predict the hydrodynamic resistance from experiments. In the fifth chapter, the structure and dynamics of aqueous ions in finite-length nanopores are studied. In the sixth chapter, a mechano-sensitive biological nanopore (MscL) is introduced as a possible nanopore for DNA sequencing. The mechano-sensitive feature of the pore gives rise to a new type of single in the form of mechanical tension. The mechanical tension and ionic current combined can be used to improve the detection sensitivity.

CHAPTER 2: Water Desalination with a Single-Layer MoS_2 Nanopore

2.1 Introduction

Producing fresh water is currently a great challenge facing the society.[19-22] High capital costs and low efficiency of current desalination technology motivate the need for advances in desalination technology.[23,24] Approximately, half of the current desalination plants use Reverse Osmosis (RO) technologies.[20,23] RO based on traditional polymeric membranes faces several challenges including slow water transport.[25,26] Advances in nanotechnology open up opportunities to design energy-efficient membranes for water desalination.[27,28] Nanopores with diameters ranging from a few Angstroms to several nanometers can be drilled in membranes to fabricate molecular sieves.[29-31] As the diameter of the nanopore approaches the size of the hydrated ions, various types of ions can be rejected by nanoporous membranes promising efficient water desalination. Among nanoscale materials, graphene and carbon nanotubes were extensively studied for both water transport and desalination.[32-36] Graphene, a single-atom thick membrane (0.34 nm), was demonstrated to have several orders of magnitude higher flux rates compared to conventional zeolite membranes.[24,29,33,34,37,38] Since water flux through a membrane scales inversely with the membrane's thickness,[29] graphene is attractive over most other materials due to its single-atom thickness.[30,34]

It has been shown that chemical functionalization of a graphene nanopore (e.g., adding hydroxyl groups) can enhance its permeability,[37,38] but reduces desalination efficiency.[37] Hydroxyl groups provide hydrophilic sites at the edge of the pore, which give rise to the attraction of water molecules and enhanced flux due to denser packing of water inside the pore.[37] Adding precise functional groups to the edge of nanopores requires complex fabrication[39]; therefore, identifying a single-atom thick membrane with hydrophilic sites can lead to further advances in water desalination technology.

Recently, a nanopore in a single-layer MoS_2 has been investigated for DNA sequencing and has been shown to provide better results compared to graphene nanopores.[27,40] Compared to graphene, a MoS_2 single-layer has two types of atoms, *i.e*. Molybdenum (Mo) and Sulfur (S). A single-layer MoS_2 has a thickness of about 1.0 nm [41] and is a mechanically strong material with an effective Young's modulus of 270 +/- 100 GPa, that is comparable to that of steel.[42] The possibility to craft the pore edge with Mo, S or both provides flexibility to design the nanopore with desired functionality. Recently, it has been shown that a nozzle-like structure of protein channels and other nanoscale membranes enhances water permeation.[43] The fish-bone structure of MoS_2 makes it amenable for a nozzle-like sub-nanometer pore for fast water permeation.[43]

Although theoretical studies of membrane efficiency are important in desalination technology, there are other aspects concerning fabrication and manufacturability of membranes such as large-area synthesis with defect-free, well-defined sealed membranes and precise pore generation that need to be addressed. Using a highly focused electron beam, and transmission electron microscope (TEM), versatile nanopores with diameters ranging from 1-10 nm were sculpted successfully in MoS_2 membranes.[9] Waduge *et al.*[44] reported that a large area, well-sealed membrane with nanopores as tiny as 2.8 nm can be fabricated. Compared to graphene, the contamination of these membranes can be lower as carbon atoms in graphene are more susceptible to contamination during chemical vapor deposition (CVD) growth. Feng *et al.*[45] also achieved high quality scalable fabrication of nanopores in a single-layer MoS_2 with sub-nanometer precision using electrochemical reaction (ECR). Several other studies have been performed on the synthesis of large-area MoS_2 monolayers.[46-55] Recently, a few groups[47,52,55] have successfully used CVD to produce highly crystalline MoS_2 of centimeter dimensions. In another study[54], a refined CVD method was proposed to create high-quality monolayer MoS_2 crystals in which the grain boundaries of MoS_2 were faceted more strongly than that of graphene resulting in mechanically more stable MoS_2 monolayers. Membrane sealing also plays an essential role in synthesis of large-area membranes required in desalination. Waduge *et al.*[44] showed that their CVD approach resulted in almost fully sealed MoS_2 membranes. Combination of these results[27,31,44-55] and the recent focus on single layer MoS_2 fabrication is promising for the large scale manufacturing of a single-layer MoS_2.

Here, we demonstrate that a single-layer MoS_2 can effectively separate ions from water. Using molecular dynamics simulations, we investigate water desalination in MoS_2 as a function of pore size, chemistry, geometry and applied hydrostatic pressure.

2.2 Results

A typical simulation box consists of a single-layer MoS_2, a graphene sheet (acting as a rigid piston to apply the external pressure), water and ions (Figure 2.1a). Here, three pore edge types for MoS_2 are considered to study the effect of terminating atoms and pore chemistry on the rate of water permeation and ion rejection. The first type of pore, which is labeled as Mixed in this study, is a combination of molybdenum and sulfur atoms. The other two pore types are labeled as Mo-only and S-only as these are terminated by molybdenum and sulfur atoms, respectively (Figure 2.1b). Water fluxes through various MoS_2 nanopores as a function of the applied pressure gradient are presented in Figure 2.2a. Three MoS_2 pore types (Mixed, Mo-only and S-only) were studied to explore their rejection rate and flux. In order to investigate the relative performance of MoS_2 over other 2D materials, a graphene nanopore which has been shown to be promising for water desalination, is also considered.[29,37] For the sake of comparison, the three MoS_2 pores and the graphene pore have approximately equivalent accessible pore areas (Mixed, A=55.45 Å^2, Mo-only, A=56.42 Å^2, S-only, A=57.38 Å^2 and graphene, A=59.67 Å^2). Our results indicate that the Mo-only pore has the highest rate of water permeation followed by the Mixed, S-only and the graphene pore for all the applied pressures (Figure 2.2a). Water flux through the Mixed pore is intermediary between Mo-only and S-only nanopores. The higher water fluxes through MoS_2 nanopores compared to graphene nanopores imply that for a desired water flux a smaller applied pressure is needed with MoS_2 nanopores. Later, in this paper, we will explain the physical chemistry and geometrical foundations of MoS_2 pore that give rise to higher flux.

2.2.1 Salt Rejection Efficiency

The other important aspect in water desalination is the ability of the membrane to reject ions. The percentage of total ions rejected by the MoS_2 and graphene pores are plotted as a function of the applied pressure in Figure 2.2b. The rejection is calculated after 1700 water molecules have filtered through the pores for all pressures. Pore sizes ranging from 20 to 60 $Å^2$ are considered for the three types of MoS_2 pores. The ion rejection decreases at higher pressures as high pressures induce higher forces on the ions giving rise to more ion translocation events. The ion rejection of small pores (e.g. 18.02 $Å^2$) is found to be 100% for all types of pores. For larger pore sizes, ions escape through the pore reducing the rejection efficiency. For the pores with equivalent areas (Mixed, A=55.45 $Å^2$, Mo-only, A=56.42 $Å^2$, S-only, A=57.38 $Å^2$ and graphene, A=59.67 $Å^2$), the general trend for ion rejection is quite similar regardless of the type of the pore (Figure 2.2b). In other words, ion rejection is mainly dependent on the pore area and the type of the pore plays a less important role, e.g. for the four pores considered, the difference in rejection is less than 10% even at a high pressure of 350 MPa.

As shown in Figure 2.2c, the water filtration rate increases sharply as the pore area increases from ~20 to ~50 $Å^2$. The sharp change in the water flow rate is due to the formation of single-file chain of water in small pores (~20 $Å^2$). As shown in ref. 11, the water flow rate is considerably reduced because of the weak hydrogen-bonding in single-file chains. For efficient water desalination, pore sizes should be chosen such that both the ion rejection and water filtration rate are optimized since very small pores lack high permeation rates and large pores (wider than 60 $Å^2$) fail to effectively reject ions.

As observed by Cohen-Tangui *et al*.[37] for graphene, the polarizability of water also has a little effect on ion rejection in MoS_2 nanopores. To introduce the effect of polarization, the flexible SPC/F model[56] was used. The ion rejection percentages associated with the flexible water model are within 2% of those modeled with the SPC/E water.

2.2.2 Permeation Coefficient

To quantify the water permeability through various pores, we compute the permeability coefficient, p, across the pore. For dilute solutions,[57]

$$p = \frac{J_{\mathrm{w}}}{-V_{\mathrm{w}}\Delta C_{\mathrm{s}} + \dfrac{V_{\mathrm{w}}}{N_{\mathrm{A}}k_{\mathrm{B}}T}\Delta P} \tag{2.1}$$

where J_{w} is the flux of water (# ns^{-1}), V_{w} is the molar volume of water (18.91 mL mol^{-1}), ΔC_{s} is the concentration gradient of the solute (1.0 M), N_{A} is the Avogadro number, k_{B} is the Boltzmann constant, T is the temperature (300 K) and ΔP is the applied hydrodynamic pressure (MPa). The permeability coefficients of the Mixed, Mo-only, S-only and graphene pores were calculated to be 71.64 # ns^{-1}, 83.61 # ns^{-1}, 62.69 # ns^{-1} and 59.32 # ns^{-1}, respectively. These coefficients are expected to also hold true for small applied pressures (less than 10 MPa), which are normally used in water desalination, since the relationship between the external pressure and the rate of water permeation is observed to be quite linear (Figure 2.2a). Previous studies[58, 59] also show that water flux in small nanochannels is linear with respect to external pressure. The permeation rates through various pores (Mo-only > Mixed > S-only > Graphene) can also be explained by the energy barrier that a water molecule needs to overcome to enter the pore. These barriers were computed to be $\Delta E_{\text{Mo-only}} = 8.50\ k_{\mathrm{B}}T$, $\Delta E_{\text{Mixed}} = 8.84\ k_{\mathrm{B}}T$, $\Delta E_{\text{S-only}} = 9.01\ k_{\mathrm{B}}T$, $\Delta E_{\text{Graphene}} = 11.05\ k_{\mathrm{B}}T$ which are consistent with the results in Figure 2.2a. The details on the energy barrier calculations are documented in Appendix A.

2.2.3 Physical Chemistry and Geometry of the Pore

Water flux (Q) is a function of density (ρ) inside the pore, velocity (V) of water through the pore and the area of the pore (A), ($Q = \rho \cdot V \cdot A$). In water desalination, increasing the area of the pore limits the salt rejection capability of the pore. As the area of the pore increases, the efficiency of rejection decreases,[43] leaving ρ and V as the control parameters to increase water flux through the pore.

As shown above, Mo-only pore exhibits the highest rate of water permeation. This can be explained by the higher water density (ρ) and velocity (V) in the Mo-only pore compared to those of the S-only and Mixed pores (Figure 2.3a, Figure 2.3b and Figure 2.3c). The average density of water follows the order of Mo-only>Mixed> S-only (1.47 g cm^{-3}, 1.37 g cm^{-3} and 1.31 g cm^{-3}, respectively). The denser packing of water molecules at the Mo-only pore can be attributed to the hydrophilic nature of Mo sites[60] at the edge of the nanopore, which attracts water molecules to the pore interior. It has been shown that Molybdenum surface has a water contact angle close to 0° (Molybdenum is a transition metal with a large atomic diameter).[60] Attraction of water molecules toward Mo sites becomes more obvious by comparing the Mixed and S-only pores densities (Figure 2.3a). In the Mixed pore, the existence of 50% Mo sites gives rise to higher density in the center of the pore compared to that of S-only pore (Figure 2.3a).

Next, we explored the velocity profiles in the pore for all the three different pores. The velocities are also higher in Mo-only pores compared to Mixed and S-only pores (Figure 2.3c). The average velocity of water is 8.26 m s^{-1}, 7.53 m s^{-1} and 7.51 m s^{-1} for Mo-only, Mixed and S-only pores, respectively.

To shed deeper insight into the physical understanding of why the velocity of Mo-only pore is higher compared to Mixed and S-only pores, we computed velocity profiles at the sites of S and Mo for both pore types of Mo-only and S-only (Figure 2.4a and Figure 2.4b). This is achieved by binning both pore types at Mo and S sites and averaging velocity at each point for a large number of sets of simulations. We observed that in the Mo-only pore, the velocity is higher at Mo site compared to the S sites. Unlike Mo-only pore, we did not observe the velocities to be higher in Mo site in the S-only pore, (Figure 2.4a and Figure 2.4b) which implies that the arrangement of Mo and S sites matter for velocity profiles. (see Appendix A for more evidence on geometry dependency of the velocity in the pore).

It has been shown that conical nanopores have higher fluxes and permeation rates.[43,61,62] Many biological nanopores, including aquaporin[43,63,64] have an hourglass shape which facilitates rapid water permeation.[65] Solid-state nanopores have also been designed for conical/hourglass shape to enhance solute and DNA transport.[66,67] Here, in Mo-only pores, due to the fish-bone structure of MoS_2,[27] the pore can be tailored[31,45] to an hourglass shape at sub-nanometer length scale (see cartoon representation of comparison between Mo-only, S-only and graphene pores in Figure 2.4c). Mo-only pore has a contraction center with hydrophobic S sites at the entrance and S-only pore has an expanding center (Figure 2.4c). Graphene has a flat entrance and exit geometry with a single–atom type exposure at the pore surface.[68] Water molecules slip on the hydrophobic edges of S and are attracted by the hydrophilic sites of Mo at the pore center in Mo-only case. This arrangement of hydrophobic and hydrophilic atoms along with the conical shape of the pore enhances the flux of water. Also, the water flux highly correlates with the energy barrier of each pore type. The computed potential of mean force (PMF) for water molecules in each pore type is the reflection of pore chemistry and geometry. In Mo-only pore, the PMF is the lowest because of the conical/hourglass and the hydrophobic-hydrophilic arrangement of the pore atoms (see Appendix A). The fundamental advantage of Mo-only pore architecture over other pores is the interplay of geometry and chemistry to produce a higher flux of water.

2.3 Discussion

Ion rejection and water flux are two important factors defining the effectiveness and performance of a water desalination membrane. In Figure 2.4d, ion rejection and water permeation rate are plotted for various nano-membrane materials[69] (MFI-type zeolite,[70] commercial polymeric seawater RO,[71] brackish RO,[71] Nanofiltration[71] and High-flux RO[71]) including MoS_2 and graphene investigated in this work. As shown in Figure 2.4d, water permeation rate is theoretically enhanced by 5 orders of magnitude using MoS_2 compared to conventional MFI-type zeolite. Also, there is a 70% improvement in the permeation rate of MoS_2 compared to graphene. In the study by Cohen-Tanugi *et al.*,[37] the permeation rate for graphene is shown to be higher than the rate we observed for graphene. This is because, in our simulations, the porosity (the ratio of the pore area to the membrane area) is smaller which decreases the permeation rate per unit area of the membrane. In this work, the comparison of MoS_2 and graphene is performed by keeping all conditions identical in the simulations. Thus, MoS_2 is potentially an efficient membrane for water desalination.

We have also investigated the potential performance of other transition metal dichalcogenide ($MoSe_2$, $MoTe_2$, WS_2, WSe_2, etc.) membranes. It was found that the transition metal atom plays a more important role than the chalcogen atom in desalination. More specifically, varying the Lennard-Jones (LJ) parameters of the chalcogen atom does not lead to a significant change in the ion rejection and water permeation (see Appendix A).

In conclusion, we have shown that MoS_2 membranes are promising for water purification and salt rejection. Mo-only pores perform the best among all possible MoS_2 pore architectures. MoS_2 nanopores with water accessible pore areas ranging from 20 to 60 $Å^2$ strongly reject ions allowing less than 12% of the ions (depending on pore areas) to pass through the porous membranes even at theoretically high pressures of 350 MPa. The water permeation rates associated with these MoS_2 porous membranes are found to be 2 to 5 orders of magnitude greater than that of currently used membrane materials (MFI-type zeolite, commercial polymeric seawater RO, brackish RO, Nanofiltration and High-flux RO) and 70% better than the graphene nanopore. The fish-bone, hourglass architecture of Mo-only pore with special arrangement of hydrophobic edges and hydrophilic center within 1 nm length, enhances water permeation to a large extent compared to its other counterparts.

2.4 Methods

Molecular Dynamics simulations (MD) were performed using the LAMMPS package[72]. The graphene sheet, which acts as a rigid piston to exert external pressure on saline water, along with the MoS_2 sheet, water molecules and ions were created by the Visual Molecular Dynamics (VMD).[73] The saline water box was placed between the graphene and MoS_2 sheet, and pure water was added on the other side of the MoS_2 sheet as shown in Figure 2.1. A nanopore was drilled in MoS_2 by removing the desired atoms. The accessible pore areas considered range from 20 to 60 $Å^2$ (see Appendix A for details on pore area calculations). The system dimensions are 4nm × 4nm × 13nm in x, y and z, respectively. The box contains about 16,000 atoms and the ions (sodium and chloride) have a molarity of ~1.0 which is higher than the usual salinity of seawater (0.599 M) because of the computational cost associated with low salinity solutions.

The SPC/E water model was used and the SHAKE algorithm was employed to maintain the rigidity of the water molecule. For non-bonded interactions, the mixing rule was used to obtain the Lennard-Jones parameters except for carbon-water interactions which were modeled by the force-field parameters given in Ref.[68] The LJ parameters are tabulated in Appendix A. The LJ cutoff distance was 12 Å. The long range electrostatic interactions were calculated by the Particle Particle Particle Mesh (PPPM).[74] Periodic boundary conditions were applied in all the three directions.

For each simulation, first the energy of the system was minimized for 10000 steps. Next, the system was equilibrated in NPT ensemble for 1 ns at a pressure of 1 atm and a temperature of 300 K. Graphene and MoS_2 atoms were held fixed in space during equilibration and the NPT simulations allow water to reach its equilibrium density (1 g cm^{-3}). Then, an additional NVT simulation was performed for 2 ns to further equilibrate the system. Temperature was maintained at 300 K by using the Nosè-Hoover thermostat with a time constant of 0.1 ps.[75,76] Finally, the production non-equilibrium simulations were carried out in NVT ensemble for 10 ns where different external pressures were applied on the rigid graphene sheet (no longer frozen in space) to characterize the water filtration through the MoS_2 nanopores. In the production runs, the MoS_2 atoms were again held fixed in space to study solely the water transport and ion rejection properties of MoS_2. To accelerate the MD simulations and gather enough statistics in the 10-ns simulations, high external pressures ranging from 50 to 350 MPa were considered in this work. Trajectories of atoms were collected every picosecond to obtain the results. For accurate velocity calculations, however, the trajectories were dumped every femtosecond and the data was averaged over 25 sets of simulations with different initial thermal velocity distributions.

2.5 Figures

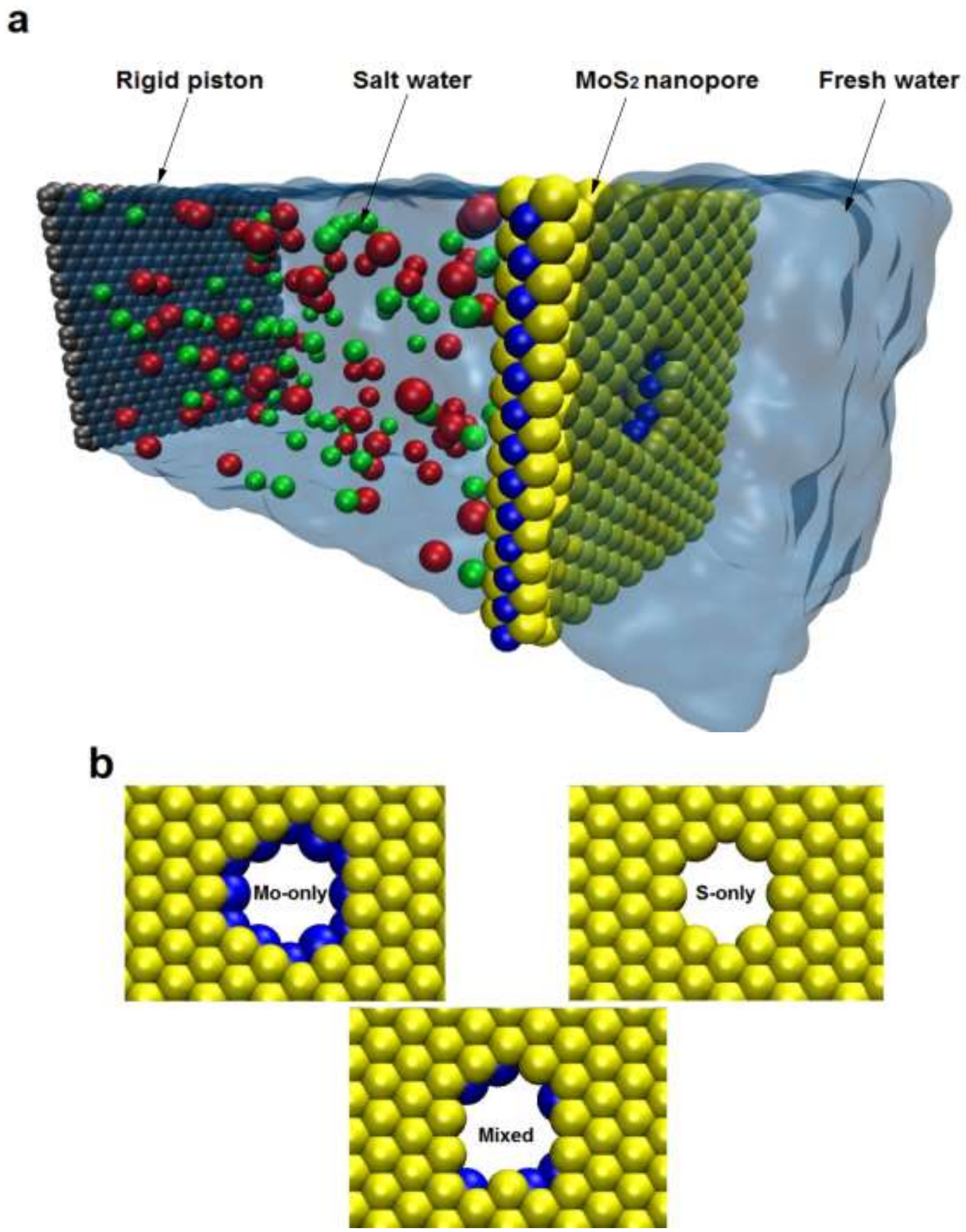

Figure 2.1 Simulation box and different pore architectures. (**a**) Schematic of the simulation box consisting of an MoS_2 sheet (molybdenum in blue and sulfur in yellow), water (transparent blue), ions (in red and green) and a graphene sheet (in grey). (**b**) Left: Mo-only pore type. Right: S-only pore type. Bottom: Mixed pore type.

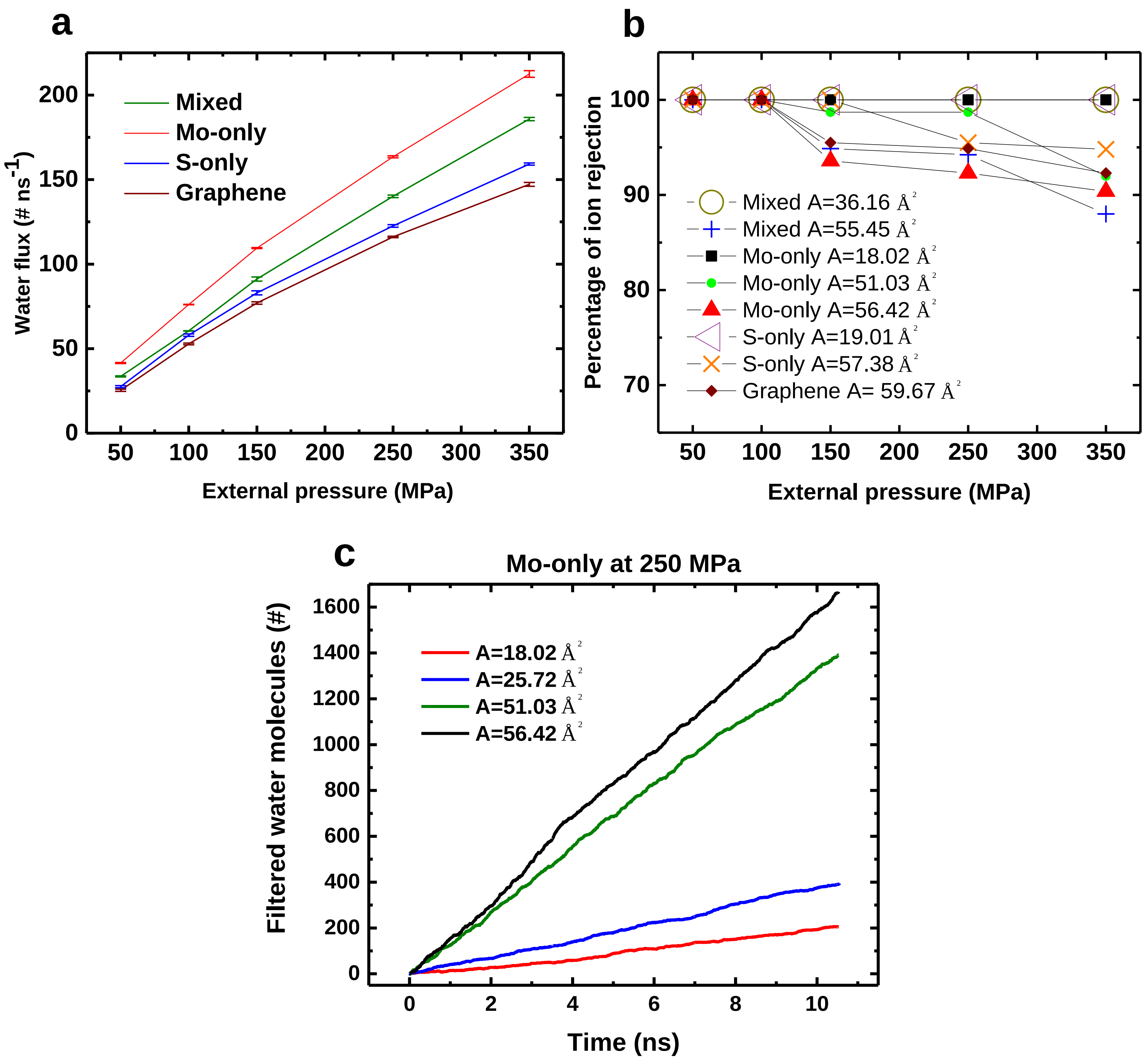

Figure 2.2 Water permeation and salt rejection. (**a**) Water flux as a function of the applied pressure for Mixed, Mo-only, S-only and graphene nanopores with equivalent pore areas. (**b**) Percentage of ion rejection by various pores as a function of the applied pressure. Pores with different edge chemistries as well as various pore areas (denoted by *A*) are considered. (**c**) Number of water molecules filtered through Mo-only pores as a function of simulation time for different pore areas at a fixed pressure of 250 MPa.

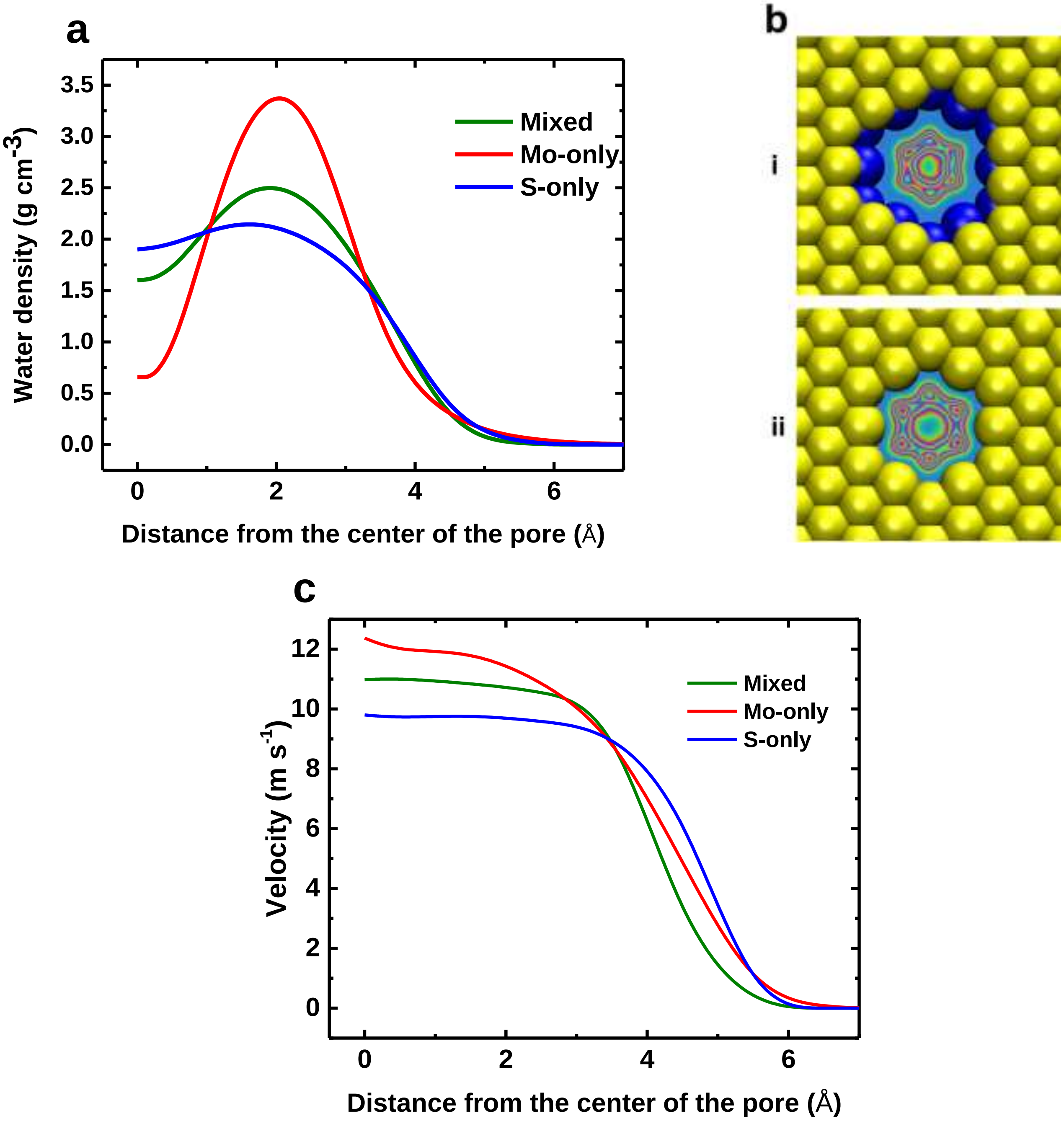

Figure 2.3 Water density and velocity profiles. (**a**) Water density distribution in the radial direction in the Mixed, Mo-only and S-only pores with equivalent pore sizes (Mixed, A=55.45 Å^2, Mo-only, A=56.42 Å^2, S-only, A=57.38 Å^2) at a fixed pressure of 250 MPa. (**b**) Density map of water distribution in Mo-only (i) and S-only (ii) pores. Blue denotes a zero probability of finding a water molecule and red indicates the highest probability of observing a water molecule. (**c**) Axial velocity of water molecules in the radial direction for Mixed, Mo-only and S-only nanopores.

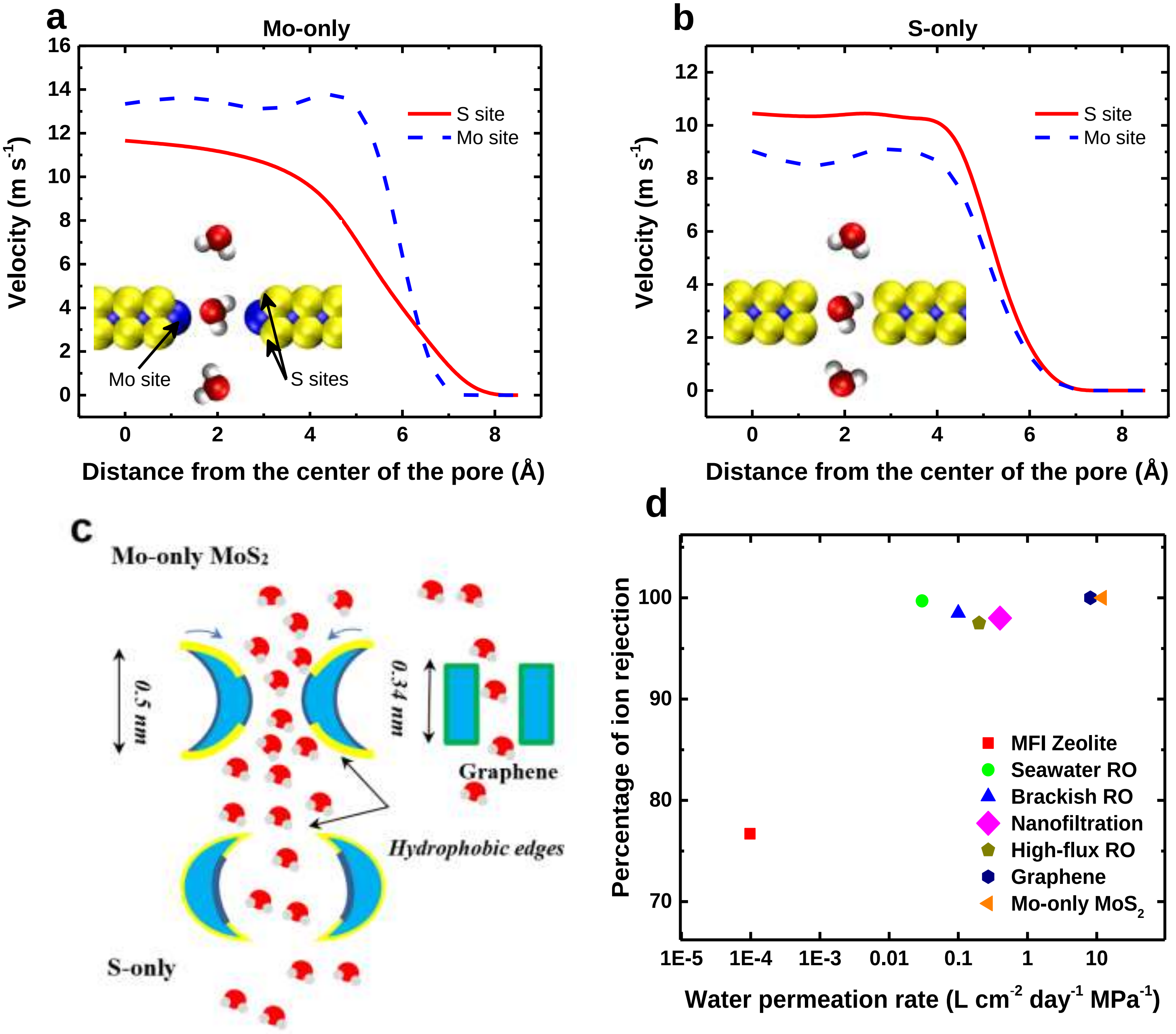

Figure 2.4 Effect of pore type on water permeation and salt rejection. (**a**) Axial velocity of water molecules in the radial direction at the location of S and Mo atom layers in the Mo-only nanopore of A=56.42 Å^2 at 250 MPa. (**b**) Axial velocity of water molecules in the radial direction at the location of S and Mo atom layers in the S-only nanopore of A=57.38 Å^2 at 250 MPa. (**c**) Cartoon representation of the pore architecture for Mo-only, S-only and graphene nanopore. (**d**) Performance of various membranes in terms of their ion rejection and water permeation rate. Water permeation rate is expressed per unit area of the membrane and per unit pressure as L cm^{-2} day^{-1} MPa^{-1}.

CHAPTER 3: Nanofludic Transport Theory with Enhacement Factors Approaching One

3.1 Introduction

Recent advances in nanotechnology and nanofabrication[27,28] combined with unique properties[35,77-82] of water transport in nanopores and nanotubes have led to significant advances in, for example, membrane technology. Due to the high flux and enhanced selectivity properties, nanoporous membranes have been found to be excellent candidates for water desalination,[1,37] electric power generation[2] and biological sensing applications.[4,27,40,83] Water transport rates in carbon-based nanopores have been shown to be several orders of magnitudes larger than the rates predicted by the classical no-slip Hagen-Poiseuille (HP) equation.[35,79,80,84] In carbon nanotubes (CNTs), enhanced flow rates are attributed to the highly frictionless and smooth surfaces.[35,81,85] Ultrathin nanoporous membranes (*e.g.*, single-layer graphene) exhibit high transport rates[1,30,34,86-88] as, classically, water flux scales inversely with the membrane thickness.[29] The exceptionally high fluxes obtained with carbon-based membranes have led to the definition of enhancement factors (EFs),[80,89,90] where the experimentally measured or computationally determined (using, for example, molecular dynamics (MD) simulations) flow rates are normalized by the flow rates computed using the classical theory (typically the Hagen-Poiseuille (HP) theory), expressed as $\mathrm{EF} = \frac{Q_{\mathrm{EXP/NEMD}}}{Q_{\mathrm{HP}}}$. While the enhancement factors are exciting and indicate the significance of carbon-based and other materials for nanofluidic transport, an important question arises as to whether the classical theory, which does not account for molecular physics that plays an important role at interfaces and under confinement, can be used to define EFs. Indeed, if a theory that accounts for all the microscopic physics is used to compute the flow rates, one would expect EFs to approach unity. However, such a theory is currently missing and in this work we report on important molecular physics that can be incorporated into the classical HP theory which can lead to EFs approaching unity (EF → 1), *i.e.*, $\mathrm{EF} = \frac{Q_{\mathrm{EXP/NEMD}}}{Q_{\mathrm{CHP}}} \to 1$.

To develop the corrected HP (CHP) theory, we characterize the thickness and diameter dependent flow by considering ultrathin graphene and finite-length CNTs. The variation of hydrodynamic properties such as interfacial friction, slip, and viscosity are studied for various thickness and diameter pores. By accounting for the variation of the key hydrodynamical properties, we develop a corrected HP equation with size dependent relations. Flow rates for pressure driven flows obtained from non-equilibrium molecular dynamics (NEMD) and published experimental data indicate that the corrected HP equation can provide EFs approaching unity. In a few cases, EFs deviating from unity are observed and possible reasons for this are discussed.

3.2 Results and Discussion

3.2.1 Scaling of Interfacial Friction, Viscosity and Slip Length

A typical simulation box consists of water molecules, two graphene sheets (the end walls) and a CNT in between the sheets. In the case of a graphene nanopore system, there is only a single graphene sheet and water molecules. A nanopore (close to the diameter of a CNT) is drilled in each graphene sheet. (6,6), (8,8), (10,10), (14,14), (18,18) and (26,26) CNTs (corresponding center-to-center diameters are 0.81 nm, 1.08 nm, 1.36 nm, 1.90 nm, 2.44 nm and 3.53 nm, respectively) with center-to-center thicknesses (the distance between the centers of the carbon atoms at the two ends of the tubes) of 5 nm, 10 nm and 20 nm are considered in this study. The system dimensions vary from 3.75 nm to 11.25 nm in x and y and 6 nm to 26 nm in z (which is along the axis of the pores) depending on the diameter and thickness of the pores. The dimensions in x and y change with the diameter to account for the porosity of the nanopores. The simulations contain about 16,000-110,000 atoms. A typical schematic of the simulation box for a graphene nanopore and CNT is shown in Figure 3.1. In equilibrium MD (EMD) simulations, friction coefficient (λ) and viscosity (μ) are obtained using the Green-Kubo formalisms[91,92] $\lambda = \frac{1}{K_B T\, A} \int_0^\infty \langle F(0) \cdot F(t) \rangle \, dt$ and

$\mu_{ab} = \frac{V}{K_B T}\int_0^\infty \langle P_{ab}\ (0) \cdot P_{ab}(t)\rangle\, dt$, respectively. K_B, T, A, V, $F(t)$ and $P_{ab}(t)$ are the Boltzmann constant, temperature, nanopore surface area, nanopore volume, total wall-fluid axial force and stress tensor, respectively. Note that A and V are calculated based on the water accessible diameter of pores (carbon-carbon Lennard-Jones (LJ) parameter, σ_{c-c} subtracted from carbon center-to-center diameter). ab are the xz and yz components of the stress tensor, $P_{ab} = \frac{1}{V}\left(\sum_i^N \frac{p_{ia}p_{ib}}{m_i} + \frac{1}{2}\sum_i^N \sum_{j\neq i}^N r_{ija}F_{ijb}\right)$ where i and j are atom indices, N is the number of atoms, p_i is the momentum of atom i, m_i is the mass of atom i, r_{ij} and F_{ij} are the distance and force between the pair of atoms i and j, respectively. Since the flow is in the z-direction (axis of the tube), we are only interested in xz and yz components of the stress tensor for the viscosity calculation. Therefore, we took the mean of the xz and yz components of viscosity in the CNT as the shear viscosity along the flow direction. λ and μ are calculated within the physical thickness of each pore/tube (h) including the size of carbon atoms at the ends. In this work, “end region” refers to the region inside the pore/tube as shown in Figure 3.1c. In graphene nanopores, the carbon-carbon LJ parameter, σ_{c-c}=0.34 nm, is taken as the physical thickness (h) of the membrane. As shown in Figure 3.1c, in CNTs, h is the addition of the center-to-center thickness and σ_{c-c} (*e.g.*, for the CNT with the center-to-center thickness of 5 nm, the physical thickness is given by h=5 nm+σ_{c-c}=5.34 nm). As shown in Figure 3.1d, for the variation of viscosity with diameter, a two-viscosity model (as discussed later) is considered with a core viscosity modelled as the bulk viscosity and an interfacial viscosity denoted by μ_i with a layer thickness of d_i. The cumulative integrals of the Green-Kubo auto correlation functions as a function of time are provided for one nanopore size in Appendix B.

λ and μ decrease with the increase in the thickness of the pore (h) as shown in Figure 3.2a-b. Significant variation of λ and μ is observed as we approach smaller thicknesses, especially for the monolayer graphene case. For long CNTs, λ is dominated by the low friction approaching the limiting friction value of infinitely long CNTs (where a periodic boundary condition is applied along the CNTs in MD simulations).[81] As the membrane becomes thinner (short CNTs and graphene nanopores), λ increases due to the significantly high friction at the ends of the pores (see Appendix B for the variation of friction coefficient along the length of the nanotube). μ is higher in graphene nanopores (higher than the bulk value, μ_{bulk}=0.85 mPa.s) owing to the highly layered structure of water in the direction of the flow in the nanopore. The axial density variation in a graphene nanopore is shown to be correlated with viscosity.[87] For CNTs, large density variations only exist at the ends of the tube (see Appendix B for the variation of water density along the length of the CNT). As the thickness increases, the overall μ inside the tubes is influenced to a lesser degree by the density fluctuations at the ends (see Appendix B shows the variation of viscosity along the length of the nanotube) and is dominated by the lower viscosity observed[90,93] inside the nanotube for an infinitely long CNT. Slip length, δ, which is the ratio of viscosity to friction $\left(\delta = \frac{\mu}{\lambda}\right)$, is directly obtained from NEMD simulations using $\delta = \frac{\mu \, U_{\text{slip}}}{\tau_{\text{interface}}}$, where U_{slip} is the slip velocity and $\tau_{\text{interface}}$ is the friction force per unit area of the pore. We obtained the slip lengths directly from NEMD to reduce the large error bar associated with the calculation of viscosity and friction coefficients obtained from EMD (both NEMD and EMD result in comparable slip lengths within the error bars). δ increases with the thickness of the pore for most cases (anomalous behavior in small diameter pores is discussed later in this paper) as shown in Figure 3.2c. Since the variation of λ with the physical thickness of the pore ($\sim h^{-0.7}$) is more significant compared to that of μ ($\sim h^{-0.5}$), slip length (which is the ratio of μ to λ) increases with thickness (scaling is based on the range of thicknesses considered here). For longer CNTs (*e.g.*, h=20.34nm), the values of viscosity and friction start to converge to those of infinitely long CNTs. The increasing slip length with thickness is consistent with the velocity profiles observed for graphene nanopores and infinitely long CNTs. In graphene, the radial velocity profile is more parabolic[29] (with a lower δ) compared to the plug-like velocity profiles in CNTs (with a higher δ).[35] The calculated slip lengths in the finite-length CNTs are one order of magnitude lower than the values reported in previous simulations[81,90,94] where the slip lengths are calculated for infinitely long CNTs without considering the end effects. We note that the slip lengths (of the order of 70 nm to 80 nm for very large diameters)[81,94] in simulations for infinitely long CNTs are lower than the slip lengths (~300 nm) observed for long CNTs (with a thickness of ~1,000 nm) in experiments.[85] Secchi *et al.*[85] suggested that the large slip length could be due to the lack of understanding of the electronic structure of interfaces. In addition to forcefields, accurate calculation of slip lengths from experimentally measured permeation rates depends on the theory used to describe the flow inside the CNTs as well as the resistance at the ends.

The scaling of λ, μ and δ with the diameter of the pore is shown in Figure 3.3. For finite-length CNTs, λ reduces (except for the single-file (6,6) CNT) with increasing diameter. This is in contrast to the trend for infinitely long CNTs where the friction coefficient increases with diameter, reaching a maximum value equal to that of the zero-curvature nanochannel[81] (λ_{flat}=1.1 × 10^4 N s m^{-3}). In infinitely long CNTs, where the effect of ends is ignored, the friction is mainly governed by the degree of curvature[81] of the CNTs. However, for finite-length CNTs, friction at the ends of the tube's wall dominates and it increases as the diameter decreases. As the thickness of CNT increases (*e.g.*, 20.34 nm), the end effects become less dominant and the scaling behavior approaches that of an infinitely-long CNT. The (6,6) CNT exhibits a very low friction coefficient. Falk *et al.*[81] showed that for single-file water in CNTs, the force amplitude or the force in the z direction between the water and CNT wall almost vanishes (friction coefficient can be obtained from $\lambda = \frac{\tau}{K_B T} \rho f^2 S(q)$, where τ is the relaxation time of the force autocorrelation function, ρ is the surface density of water, f is the force amplitude (the force per particle from the wall), $S(q)$ is the structure factor of water and q is the wavenumber). To further investigate the low friction coefficient in (6,6) CNTs, we plotted the force autocorrelation function (FACF) for different CNT diameters in Appendix B. The magnitude of FACF at t=0 ($\langle \mathrm{F}(0)^2 \rangle$), is shown to be the smallest for the (6,6) CNT consistent with the explanation of low force amplitude by Falk *et al*..[81] In addition, the relaxation time of FACF for the (6,6) CNT is small, which leads to a smaller friction coefficient, compared to other CNTs (for more details, see Appendix B). For the graphene nanopore case (see Figure 3.3a), λ exhibits a small increase with the increase in diameter until it reaches the value equal to that of the zero-curvature single-layer graphene slit. In Figure 3.3b, μ is plotted for the graphene nanopores as a function of the pore diameter and a value higher than that of the bulk viscosity is observed for the pore diameters considered. μ decreases with diameter as the structural layering of water along the axis of the pore (z direction) starts to vanish for a larger pore diameter. For very small diameter nanopores (subnanometers), inside the pore, the bulk-like region vanishes and viscosity is dominated by the low interfacial viscosity. In CNTs (Figure 3.3c), μ is lower than the bulk viscosity and increases with the diameter until it reaches the bulk value for large enough tubes (as large diameter CNTs have larger bulk-like region, compared to small diameter CNTs). In small diameter CNTs, the overall effective viscosity is affected by the low viscosity near the surface. Low viscosity near the surface is explained by higher than bulk diffusion coefficient near the surface[90] (viscosity and diffusion are inversely related by the Einstein relation). Diffusion coefficient increases as the hydrogen bonding is weakened near the surface.[95] Slip length, in finite-length CNTs, increases with diameter as the ratio of viscosity-to-friction coefficient increases with diameter as shown in Figure 3.3d (viscosity increases with diameter and friction decreases with diameter). Slip length in graphene, however, decreases with diameter as viscosity decreases and friction increases with diameter.

Water viscosity and friction coefficient exhibit length-scale dependence, *e.g.*, variation with thickness of the CNT. The effective viscosity and friction coefficient for a given radius can be obtained from the weighted average of the values in the end regions (μ^e and λ^e) and in the middle section of CNT (μ^∞ and λ^∞ (modeled by infinitely long CNTs)). These effective parameters are subsequently used in a simplified single-form HP equation (discussed in the next section) without separately calculating the contribution from the end region and the middle section of CNT. For a given radius (*r*), viscosity and friction coefficient variation with thickness for finite-length CNTs can be expressed as,

$$\mu(h,r) = \frac{l \cdot \mu^e(r) + (h-l) \cdot \mu^\infty(r)}{h}$$

and

$$\lambda(h,r) = \frac{l \cdot \lambda^e(r) + (h-l) \cdot \lambda^\infty(r)}{h}$$

where *l* denotes the total length of the end regions at both ends of the tube (see Figure 3.1c). We define *l* as a function of h and x_e ($\mathrm{x_e}$ is the length of the region at one end, see Figure 3.1) using $l = 2x_\mathrm{e}\left(1 - e^{-\frac{h}{2x_\mathrm{e}}}\right)$ where *l* approaches $2x_\mathrm{e}$ for large h ($h > 2x_\mathrm{e}$) and *l* approaches h for small h ($h < 2x_\mathrm{e}$). As shown in

Appendix B, most of the variation of viscosity and friction coefficient takes place within 0.7 nm of the edge of the nanotube (the end region length at one end of the nanotube is set to be x_{e}=0.7nm). The expressions given above are found to describe the thickness variation of viscosity and friction coefficient (see Appendix B). As shown in Appendix B, viscosity and friction vary along the length of the CNT; therefore, viscosity and friction in the end regions (μ^{e} and λ^{e}) and in the middle section of the nanopore (μ^{∞} and λ^{∞}) are different for different radii of the CNT. Variation of viscosity with radius is obtained as a weighted average of viscosities in the interface (denoted by μ_i with a layer thickness of d_i (see Figure 3.1d)) and in the bulk region of the CNT using $\mu(r) = \mu_{\mathrm{i}} \frac{A_{\mathrm{i}}(r)}{A_{\mathrm{T}}(r)} + \mu_{\mathrm{bulk}} \left(1 - \frac{A_{\mathrm{i}}(r)}{A_{\mathrm{T}}(r)}\right)$, where A_{i} and A_{T} are the interfacial and total cross-sectional areas of CNTs, respectively.[90] Expressing A_{i} and A_{T} in terms of r and d_i, the variation of μ^e and μ^{∞} with radius is reduced to,

$$\mu^e(r) = \frac{(d_{\mathrm{i}})^2(\mu_{\mathrm{bulk}} - \mu_{\mathrm{i}}^e)}{r^2} - \frac{2d_{\mathrm{i}}(\mu_{\mathrm{bulk}} - \mu_{\mathrm{i}}^e)}{r} + \mu_{\mathrm{bulk}} \quad \text{(Pa s)}$$

and

$$\mu^{\infty}(r) = \frac{(d_{\mathrm{i}})^2(\mu_{\mathrm{bulk}} - \mu_{\mathrm{i}}^{\infty})}{r^2} - \frac{2d_{\mathrm{i}}(\mu_{\mathrm{bulk}} - \mu_{\mathrm{i}}^{\infty})}{r} + \mu_{\mathrm{bulk}} \quad \text{(Pa s)}$$

where μ_{i}^e, $\mu_{\mathrm{i}}^{\infty}$ and d_i are 9.5×10^{-4} Pa s, 3.2×10^{-4} Pa s and 0.38 nm, respectively. See the Appendix B for details on the variation of viscosity with radius. The variation of λ^e and λ^{∞} with radius are expressed using the power law form as,

$$\lambda^e(r) = C_5 r^{\alpha_1} + \lambda_{\mathrm{slit}} \quad (\mathrm{N\ s\ m^{-3}})$$

and

$$\lambda^{\infty}(r) = C_6 r^{\alpha_2} + \lambda_{\mathrm{flat}} \quad (\mathrm{N\ s\ m^{-3}})$$

where the coefficients C_5 and C_6, and exponents α_1 and α_2 are 5.9×10^4 N s m^{-3} nm$^{3.5}$, -6.3×10^3 N s m^{-3} nm$^{0.6}$, -3.5 and -0.6, respectively. $\lambda_{\mathrm{slit}}=4.2 \times 10^5$ N s m^{-3} and $\lambda_{\mathrm{flat}}=1.1 \times 10^4$ N s m^{-3} are the friction coefficient in a slit with a thickness of x_{e} and a nanochannel with two flat parallel graphene sheets, respectively ($r \to \infty$). r (accessible radius of CNTs) and h are in nm. See Appendix B for more details on the variation of friction coefficient with radius.

3.2.2 Pressure Driven Flows

Permeation coefficient $\left(P_Q = \frac{Q}{\Delta P}\right)$, defined as the volumetric flow rate (Q) normalized by the applied pressure difference across the pore (ΔP), is obtained from the HP equation. The permeation coefficient determined from the HP equation with a slip condition, $P_Q^{\mathrm{CHP}} = \frac{\pi\left(r^4+4r^3\frac{\mu(h,r)}{\lambda(h,r)}\right)}{8\mu(h,r)}\frac{1}{h_l^{\mathrm{Dagan}}}$, is corrected by taking into account the variation of λ, μ and δ with thickness and diameter of the nanopore. In addition, the thickness in the corrected-HP (CHP) is the distance over which the pressure drops. Dagan *et al.*[96] developed a theory for pressure driven Stokes flow through an orifice in which the effective hydrodynamic pressure drop length is estimated to be a function of radius and thickness of the orifice as $h_l^{\mathrm{Dagan}} = h + \frac{3}{8}\pi r$. The permeation coefficient predicted by the CHP is shown in Figure 3.4 as a function of the reciprocal thickness of the pore for three different diameters corresponding to CNTs of (10, 10), (14,14) and (18, 18). We note that the CHP theory is able to reasonably match the water permeation coefficient from NEMD simulations (used as the reference method) for all the thickness and diameter variations considered in this study. In NEMD, different pressure drops, ranging from 10MPa to 50MPa, are applied to obtain the reference permeation coefficients presented as blue circles in Figure 3.4. For subnanometer pores (*e.g.* single-file water flow in (6,6)) where the water flow is anomalous and is governed by a hopping mechanism,[29] the CHP fails to predict the permeation coefficients from NEMD simulations. We also plotted the permeation coefficients obtained from other models in Figure 3.4. HP equation with a slip condition, where viscosity and friction coefficient are taken from an infinitely long CNT $\left(P_Q^{\mathrm{HP-sc}} = \frac{\pi\left(r^4+4r^3\frac{\mu_\infty}{\lambda_\infty}\right)}{8\mu_\infty}\frac{1}{h}\right)$, fails to predict P_Q for the graphene nanopores and short CNTs as it overestimates the slip length $\left(\frac{\mu_\infty}{\lambda_\infty}\right)$ for thin membranes. As shown in Figure 3.2, slip length decreases as the thickness of the membrane decreases. HP equation with no slip condition and bulk viscosity $\left(P_Q^{\mathrm{HP}} = \frac{\pi r^4}{8\mu_{\mathrm{bulk}}}\frac{1}{h}\right)$ fails for the thicknesses considered and the deviation grows for longer tubes where the slippage becomes more dominant. The permeation coefficient estimated by the Dagan's equation, $P_Q^{\mathrm{Dagan}} = \frac{\pi r^4}{8\mu_{\mathrm{bulk}}} \frac{1}{\left(h+\frac{3}{8}\pi r\right)}$, fails to match the NEMD results (see Figure 3.4) mainly due to the lack of slippage in the model. For infinitesimally thin membranes ($h \rightarrow 0$), the Dagan's solution reduces to the Sampson's equation which serves as the upper limit for the no slip Stokes flow permeation coefficient through an orifice. We should note that Dagan's equation is simply the HP with no slip condition with a correction to the hydrodynamic pressure drop length. Using MD simulations, Suk *et al.*[87] introduced an empirical relationship for the hydrodynamic pressure drop length, $h_l^{\mathrm{GRA}} = 0.27r + 0.95\,\mathrm{nm}$ in a monolayer graphene pore. Dagan's and HP with no slip condition result in identical permeation coefficients when the Suk's empirical relationship is used for the thickness in HP with no slip condition. We also introduced the slip term in the Dagan's equation $\left(P_Q^{\mathrm{Dagan-sc}} = \frac{\pi\left(r^4+4r^3\frac{\mu_\infty}{\lambda_\infty}\right)}{8\mu_\infty\left(h+\frac{3}{8}\pi r+\frac{3}{2}\pi\frac{\mu_\infty}{\lambda_\infty}\right)}\right)$ using the viscosity and friction coefficient from that of an infinitely long CNT. Dagan's equation with a constant slip condition also fails for thin membranes as it overestimates the resistance modeled by Sampson (this is evident as the permeations by Sampson are lower than the permeations in a monolayer graphene nanopore from NEMD). In general, accurate variations of viscosity, friction, and slip length with thickness and diameter as well as a proper hydrodynamic pressure drop length are required for a complete model. The individual contribution for the corrections of viscosity, friction, and hydrodynamic pressure drop length is discussed in Appendix B.

3.2.3 Enhancement Factors

In experiments, water transport rates in CNTs have been shown to be enhanced by several orders of magnitude over the rates predicted by the no-slip HP theory. Holt *et al*.[80] attributed this enhancement to the large slippage at the frictionless CNT surface and enhancement factors of 100-1000 over no-slip HP flow rates were reported. The validity of the HP equation for small diameter CNTs was questioned[90,97] because of the giant slip lengths[79,80,85] and the lack of understanding of the scaling of hydrodynamic properties with CNT sizes. With the HP equation corrected to account for the variation of viscosity and slip length with the diameter of CNTs, the enhancement factor was reassessed[21,24] as $\frac{Q_{\mathrm{slip}}}{Q_{\mathrm{no-slip}}} = \left(1 + \frac{4\delta(r)}{r}\right)\frac{\mu_{\mathrm{bulk}}}{\mu(r)}$. Suk *et al.*[94]

included the effect of finite-length CNTs by modeling the entrance friction using Sampson's equation and reassessed the enhancement factor based on the thickness and diameter of CNTs; here, a direct investigation of the variation of hydrodynamic properties with both diameter and thickness of the pores, including single-layer graphene nanopores, was performed. Figure 3.5 shows the enhancement factors reported in the literature for various nanopores and CNTs. The data includes both experiments and computations as well as some NEMD calculations performed in this study. When the enhancement factors (from experiments and NEMD simulations) were reassessed using the corrected HP theory, they approach unity. As shown in Figure 3.5 for most thickness-to-radius ratios $\left(\frac{h}{r}\right)$, the permeations obtained from the CHP theory approach unity and are in reasonable agreement with experiments, especially for larger values of $\frac{h}{r}$. For graphene, the permeation coefficients are overestimated by the CHP theory and the enhancement factors are below one. Possible explanations for this discrepancy are i) lack of accurate force-fields for graphene nanopores where quantum and other effects could be important and affect the scaling of hydrodynamic parameters, ii) challenging flow rate measurements and existence of defects and contaminants in experiments,[30,85] iii) inaccurate prediction (by NEMD) of the actual hydrodynamic pressure drop distance, *etc*. For some of the long CNTs, the permeation coefficients are underestimated by the CHP (leading to enhancement factors higher than 1) which one might find counterintuitive due to the presence of defects and contaminants in experiments. However, the presence of defects and contaminants in experiments can also result in flow enhancement in some cases. It was shown that pure graphene (in vacuum conditions) is more hydrophilic (the forcefields used in this work) than the graphene contaminated in air.[98] Enhanced hydrophobicity (especially in the case of long CNTs) results in faster water flow rates in experiments. In addition, it was shown that hydroxyl groups at the edge of nanopores can enhance the flow rates by attracting water molecules towards the nanopore.[37] Therefore, enhancement factors of both higher and lower than 1 should be expected. There is also some discrepancy between the permeations predicted by CHP and other NEMD studies. This is mainly due to the use of different force-fields. In our study, we used the force-field developed by Wu *et. al*.[68] which reasonably matches the experimental water contact angle on graphene.

3.3 Conclusion

Flow rates in carbon-based nanopores far exceed the predicted HP flow rates; therefore, in the absence of a theory that accounts for the microscopic physics of transport in nanopores, large enhancement factors were reported. When the microscopic physics is incorporated into the HP theory, the previously reported enhancement factors (of the order of 1000) approach unity. To develop the corrected HP model, the variation of hydrodynamical properties (friction coefficient, viscosity and slip length) with the thickness and diameter are calculated using Green-Kubo relations and molecular dynamics simulations. Significant variations are observed as the thickness approaches the infinitesimal thickness of the single-layer graphene nanopore. Flow in long CNTs is enhanced by the smooth and frictionless nature of the tube surface where a high slippage occurs. As the thickness reduces, flow rates are dominated by high interfacial friction and viscosity at the pore end regions. For friction coefficient and viscosity, size dependent relations are introduced. Permeation coefficients from the corrected Hagen-Poiseuille model, based on the friction and viscosity relations, successfully predict the values from experiments and molecular dynamics simulations.

3.4 Methods

MD simulations were performed using the LAMMPS package.[72] The SPC/E water model was used and the SHAKE algorithm was employed to maintain the rigidity of the water molecule. The carbon-water interactions were modeled by the force-field parameters given in Wu *et al*.[68] Since the carbon atoms are fixed in space, the interactions between carbon atoms were turned off. We should note that fixing the carbon atoms can lead to flow rate errors of 10%-20% due to lower friction.[35,99] Since flexible membranes add complexity to the calculation of different properties in the radial direction, the effect of flexibility is neglected in this study. The LJ cutoff distance was 12 Å. The long range electrostatic interactions were calculated by the Particle-Particle-Particle-Mesh (PPPM) method.[100] Periodic boundary conditions were applied in all the three directions. For each simulation, first the energy of the system was minimized for 10000 steps. Next, the system was equilibrated using NPT ensemble for 1 ns at a pressure of 1 atm and a temperature of 300 K with a time-step of 1fs. With the graphene atoms held fixed in space, the NPT simulations allow the water to reach its equilibrium density (1 g/cm^3). Then, an additional NVT simulation was performed for 2 ns to further equilibrate the system. Temperature was maintained at 300 K by using the Nosè-Hoover thermostat with a time constant of 0.1 ps.[75,76] Finally, the production equilibrium and non-equilibrium simulations were carried out in NVT ensemble for 20 ns.

3.5 Figures

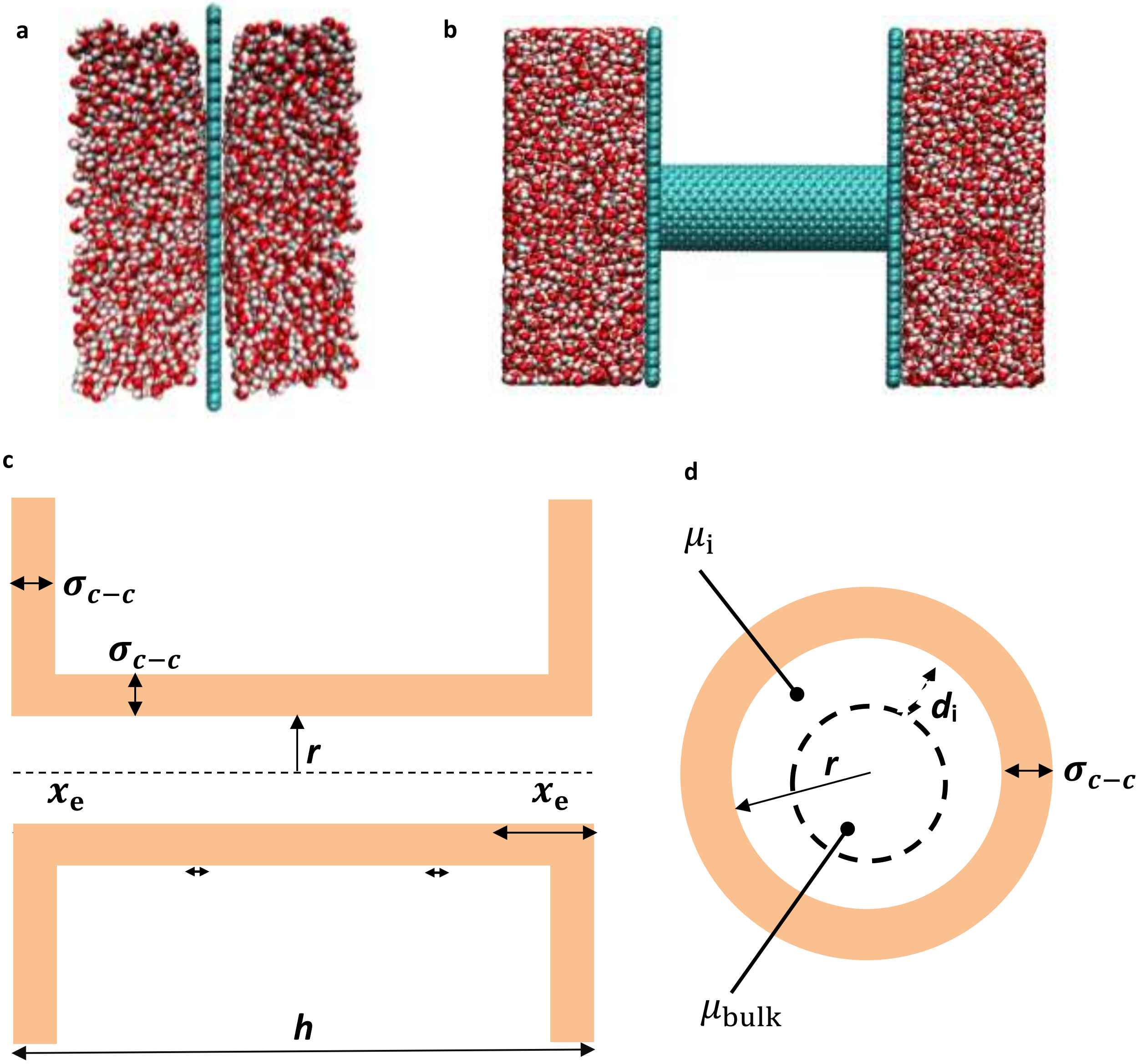

Figure 3.1 a) Simulation box for water across a monolayer graphene nanopore. **b)** Simulation box for water across a 5nm-long (14,14) CNT with a graphene sheet at both ends of the tube. **c)** h, x_e, σ_{c-c} and r are shown for a CNT. The CNT and graphene walls are shown in green. The dashed line represents the centerline of the pore. h is the physical thickness of each pore including the size of carbon atom (σ_{c-c}). r is the water accessible radius of the pore. l denotes the combined length of both end regions which is given by $l = 2x_e\left(1 - e^{-\frac{h}{2x_e}}\right)$ where l approaches $2x_e$ for large h ($h > 2x_e$) and l approaches h for small h ($h < 2x_e$). **d)** Cross-sectional view of a CNT where the interfacial annular region, bulk-like region, r, d_i and σ_{c-c} are shown. d_i is the thickness of the interfacial annular region.

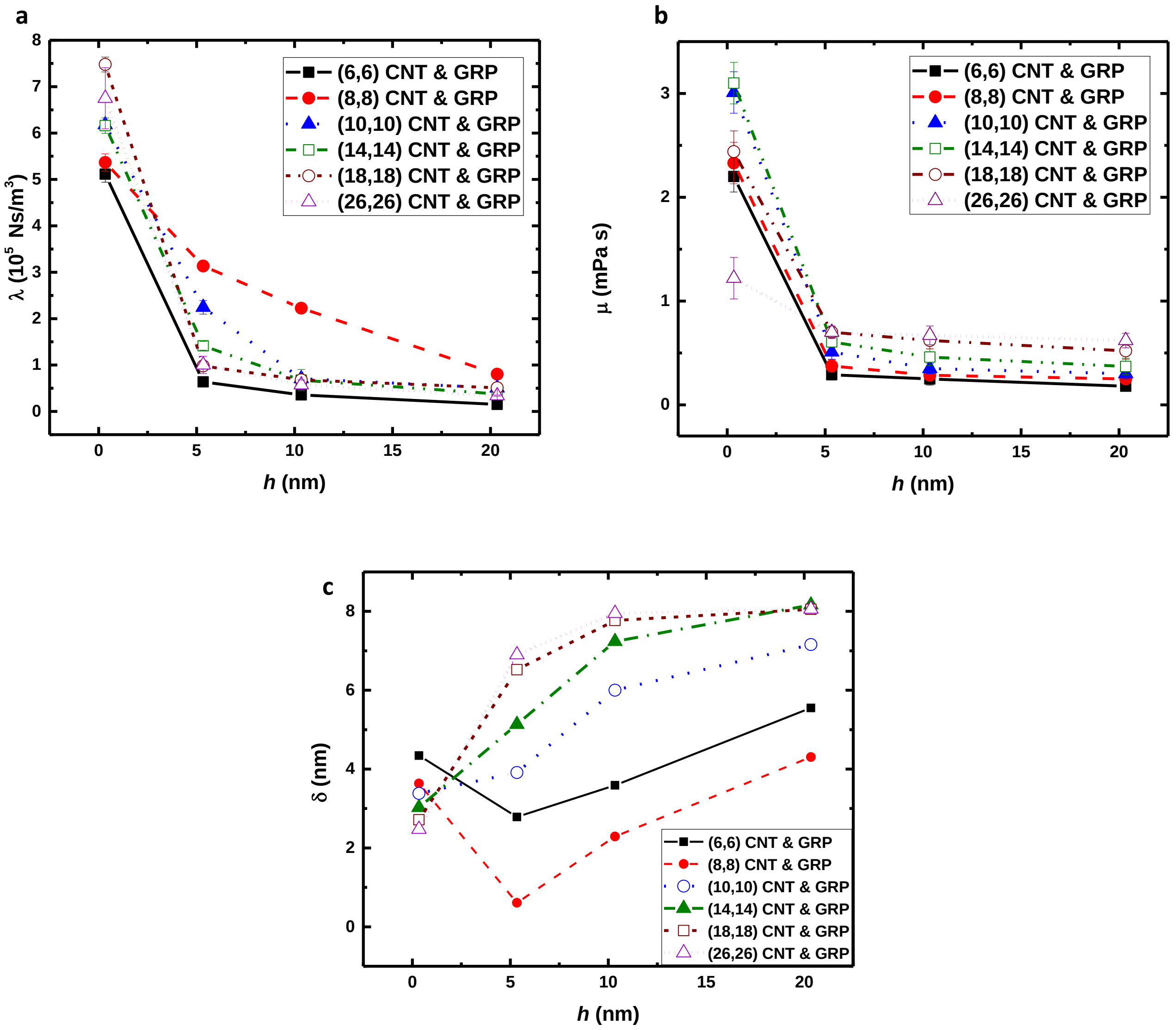

Figure 3.2 Interfacial friction coefficient (**a**), viscosity (**b**) and slip length (**c**) inside the nanopores are plotted as a function of physical thickness of the nanopores (*h*) for different diameters. The graphene nanopores (denoted as GRP with *h*=0.34nm) and CNTs have similar diameters. λ and μ decrease with increase in thickness. Friction is high at the ends increasing the overall friction in short nanopores. Viscosity is higher in short nanopores due to density layering at the ends. Slip length changes with thickness following the scaling of $\frac{\mu}{\lambda}$. As thickness increases, the values of friction, viscosity and slip length approach that of infinitely-long CNTs.

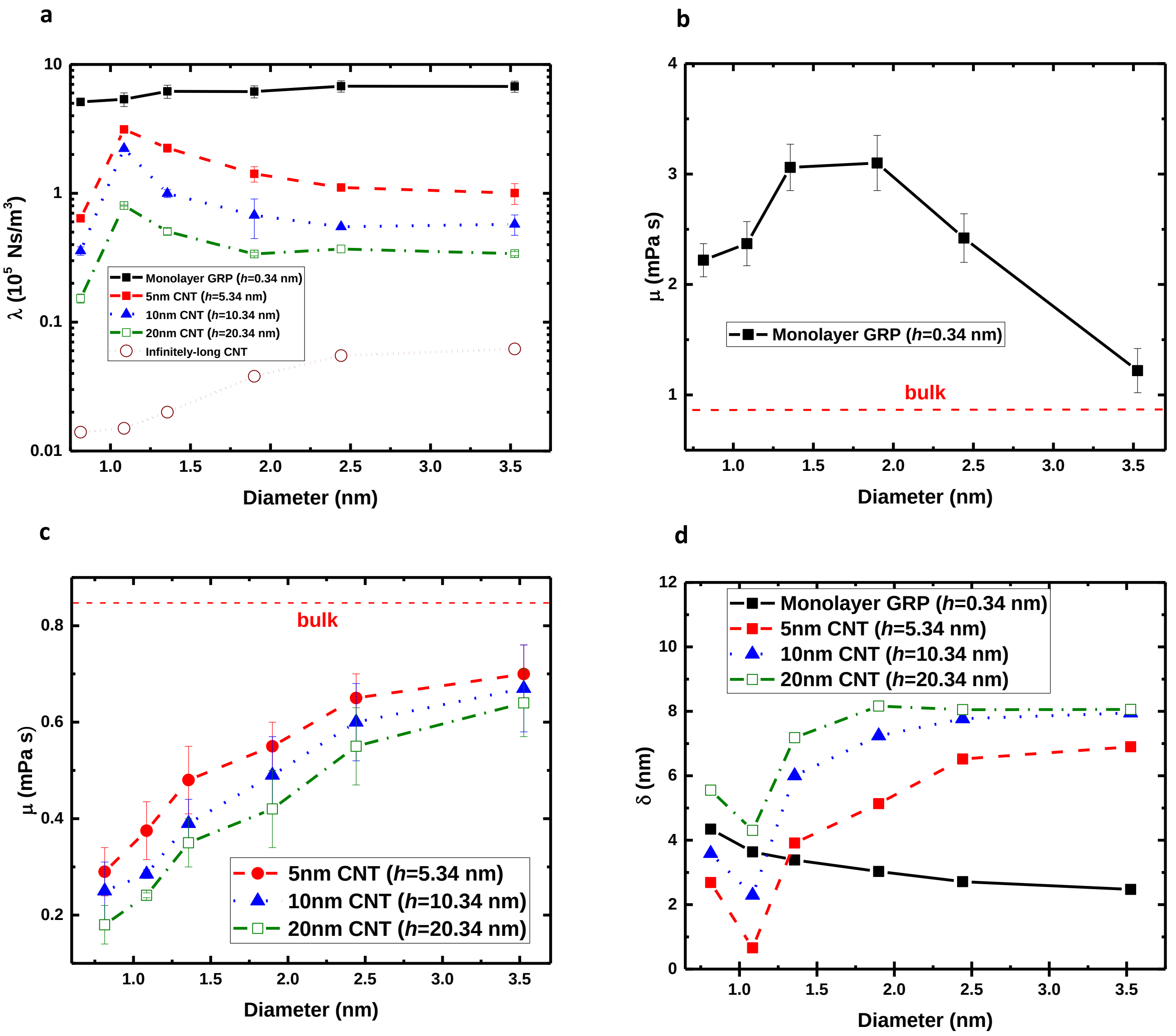

Figure 3.3 Interfacial friction coefficient (**a**), viscosity in monolayer graphene (**b**), viscosity in finite-length CNTs (**c**), and slip length (**d**) are plotted as a function of diameter of the nanopore (the graphene nanopores (denoted as GRP) and CNTs have similar diameter). For CNTs, friction decreases with increase in diameter (except the single-file (6,6) CNT) as small diameters exhibit larger friction at the ends. This is in contrast with the behavior in infinitely long CNTs where a periodic boundary condition is applied with no ends. Viscosity in monolayer graphene is higher for smaller diameters because of stronger density layering along the flow direction. As diameter increases, viscosity approaches its bulk value in both graphene nanopores and CNTs. Slip length increases for CNTs (except for the single-file (6,6) CNT) and decreases for graphene with increase in diameter following the scaling of viscosity-to-friction coefficient ratio. Unlike infinitely long CNTs, slip length increases with diameter for finite-length CNTs especially for shorter CNTs (*e.g.*, 5.34nm) where the end effects are dominant.

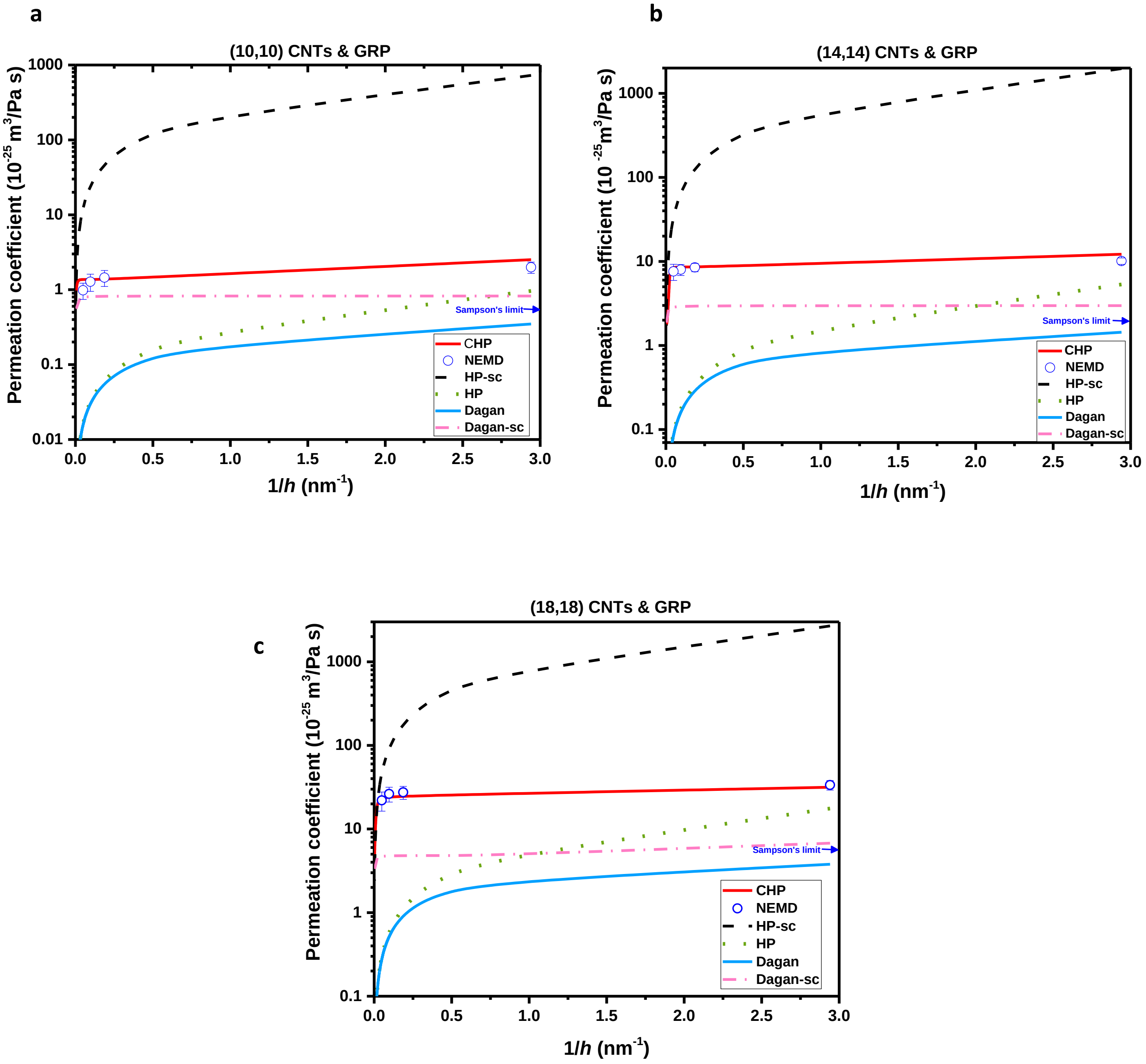

Figure 3.4 Permeation coefficients of monolayer graphene and finite-length CNTs from pressure driven NEMD simulations (blue circles) are compared with the corrected-HP model (P_Q^{CHP}, red solid line) and other theoretical models (HP with viscosity and friction from infinitely long CNTs ($P_Q^{\mathrm{HP-sc}}$, black dashed line), no-slip HP with bulk viscosity (P_Q^{HP}, green dotted line), Dagan's model (P_Q^{Dagan}, blue solid line) and Dagan's model with viscosity and friction from infinitely long CNTs ($P_Q^{\mathrm{Dagan-sc}}$, pink dashed and dotted line) for **a.** (10,10), **b**. (14,14) and **c**. (18,18) CNTs and similar graphene nanopore sizes. The limit of Sampson's model (Dagan's model with $h \to 0$) is also shown by a blue arrow. The corrected HP theory predicts the permeation from NEMD simulations reasonably well. For long CNTs, no-slip HP and Dagan theories fail as they do not account for the slippage in long CNTs. Slip-HP fails as it overestimates the slippage for short nanopores. Slip-Dagan fails for short nanopores since it overestimates the resistance modeled by the Sampson theory.

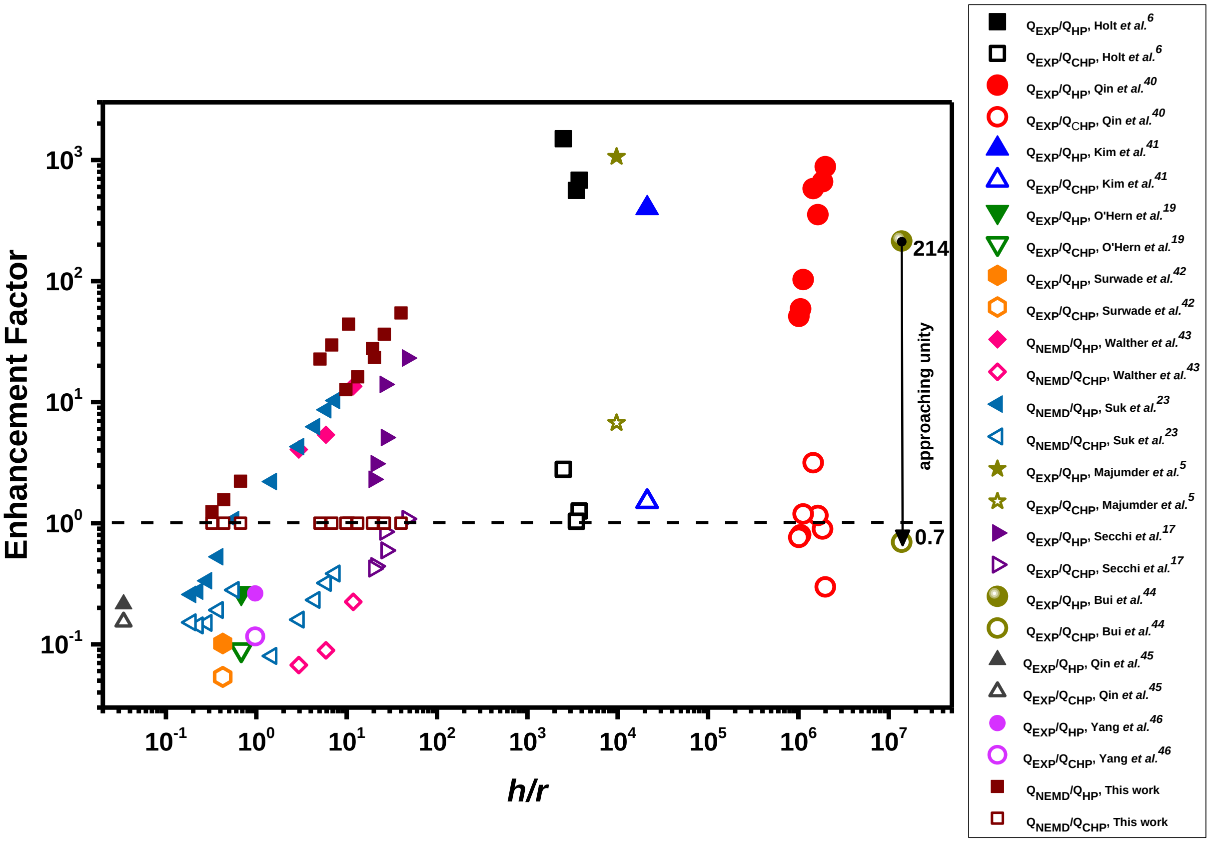

Figure 3.5 Enhancement factors using the classical no-slip HP theory (filled symbols) and the corrected-HP theory (hollow symbols) are shown for different pore sizes as a function of the physical thickness-to-radius ratio for various experimental and computational permeation coefficients.[29,30,79,80,85,101-107] The previously reported enhancement factors based on classical HP theory (of the order of 1000 for long CNTs) approach unity when the permeations are normalized by that of the corrected-HP theory. We show this for one of the experimental measurements (Bui *et al.*[105]) by an arrow $\left(\frac{Q_{\text{EXP}}}{Q_{\text{HP}}} = 214 \rightarrow \frac{Q_{\text{EXP}}}{Q_{\text{CHP}}} = 0.7\right)$.

CHAPTER 4: Revisiting Sampson's Theory for Hydrodynamic Transport in Ultrathin Nanopores

4.1 Introduction

Recent experimentation[27,28,80,108,109] and computational studies[35,79,84] have revealed unique properties of fluids in nanoconfinement. Water in carbon-based nanopores has been shown to have giant transport rates[29,35,80,82,85], fast rotational motion[110,111] and rotation-translation coupling[112]. Nanopores in transition metal dichalcogenides (TMDs) have also been explored and found to possess high water permeability and selectivity making them attractive candidates for water desalination[1,113] and nanopower generation[2]. Water in biological nanopores, such as aquaporins, exhibits a unique single-file dynamical behavior[43,114] with a high flux of 10^9 molecules per second. 2D materials (*e.g.*, graphene, MoS_2) have been shown to possess high transport rates[1,29,88] as flux is expected (classically) to scale inversely with the thickness of the pore. For atomically thin pores, the flow rates are dictated by the entrance/exit hydrodynamic resistance governed by the viscous energy dissipation. The entrance/exit effects are also important in thicker pores where the resistance inside the pore is negligible[61,94] (*e.g.*, frictionless flows in carbon nanotubes (CNTs)). In CNTs, accurate calculation of slip lengths, from experimentally measured permeation rates[85], depends on the accuracy of the theory used to obtain the entrance/exit resistance. As the entrance/exit resistance dominates the total resistance in a CNT, a slight error in the estimation of the entrance/exit resistance could lead to a large error in the calculation of slip length. Therefore, the need for an accurate theory describing the entrance/exit resistance (defined as the ratio of the pressure drop to the volumetric flow rate, $R = \frac{\Delta P}{Q}$) in both ultrathin and thick pores has been recognized in the past few decades[43,88,115].

Couette[116] in 1890 first introduced the entrance/exit resistance by crudely adding an additional length to the actual length of the tube in the Hagen-Poiseuille (HP) equation[117,118] ($R^{\mathrm{HP}} = \frac{8\mu h}{\pi a^4}$, where μ is the viscosity, h is the tube length/thickness and a is the tube radius), which describes the flow in circular tubes independent of the end effects. A year later, Sampson[119] obtained the exact solution for the entrance/exit resistance of a zero-length orifice $\left(R^{\mathrm{Sampson}} = \frac{3\mu}{a^3}\right)$. Sampson formula was later confirmed experimentally[120] for $\frac{h}{a} < 26$. Weissberg[120] further found an upper bound for the entrance/exit resistance to be 1.154 times that of the Sampson formula. Combining Sampson and HP equations, Dagan[96] obtained the total flow resistance across a finite-length orifice $\left(R^{\mathrm{Dagan}} = \frac{(8h + 3\pi a)\mu}{\pi a^4}\right)$ using a no-slip boundary condition at the pore walls. More recently, hydrodynamic entrance/exit resistance was obtained for hourglass pores by modifying the pre-factor in the Sampson formula based on finite-element calculations[43,61]. The Sampson formula, however, is found to overestimate the hydrodynamic resistance in graphene nanopores[61,115]. Gravelle *et al.*[61] attributed this overestimation to the finite thickness of a single-layer graphene nanopore. In this work, we show that the lower hydrodynamic resistance in graphene compared to that of the Sampson formula is due to the finite slippage at the edge of the pore. The resistance obtained from molecular dynamics (MD) simulations for a fictitious hydrophilic pore (with no slip) matches the resistance predicted by the Sampson formula. Motivated by this observation in MD simulations, we revisit the Sampson theory and introduce a finite slip length (δ) into the original theory. Introducing a finite slip length at a zero length orifice of the Sampson's theory may be counter-intuitive at first; however, a slip length can be introduced if the velocity at any cross-section is known, *e.g.*, velocity profile right at the orifice. To further account for the interfacial molecular physics, we corrected the Sampson theory for the variation of viscosity at the interface of graphene membrane. The slip and viscosity corrected Sampson theory is able to predict the hydrodynamic resistance from MD simulations. In addition to MD simulations, steady-state Navier-Stokes (NS) continuum simulations are carried out (see the Appendix for more details about NS simulations).

4.2 Role of Slippage

Water transport in graphene nanopores is associated with slippage at the pore due to the significance of molecular physics between water molecules and carbon atoms. Slip length in graphene decreases with radius as shown in Figure 4.1a (see the Appendix for slip calculation details). In the original Sampson theory, a no-slip condition is assumed at the wall. Slippage in graphene results in higher permeability (or lower resistance) compared to the permeability predicted by the original Sampson theory. In this work, the interaction parameter between the oxygen atom of water and carbon atom of graphene are changed such that a no-slip interface (hydrophilic wall) is achieved in MD simulations (see the Appendix). In Figure 4.1b, the axial velocity profile of the fictitious hydrophilic pore is compared to that of the non-fictitious graphene (Wu *et al.*[68] force-field) for a radius of 3.54 nm. The hydrodynamic resistance is directly computed from MD simulations to be $5.78\pm0.03 \times 10^{22}$ Pa s/m^3 and $4.21\pm0.4 \times 10^{22}$ Pa s/m^3, for the hydrophilic pore and graphene pore, respectively (see the Appendix). The resistance obtained for the hydrophilic pore matches the resistance predicted by the Sampson theory ($R^{\mathrm{Sampson}} = \frac{3\mu}{a^3} = 5.75 \times 10^{22}$ Pa s/m^3, where μ is taken to be the bulk water viscosity (0.85 mPa.s) and a is calculated based on the water accessible radius (see Figure 4.1b)). Sampson theory, however, fails to predict the resistance for the graphene nanopore (where a slip length exists) as it does not include interfacial physics in the form of slip length and viscosity variation. Motivated by the results in Figure 4.1, the effect of slip length is introduced into Sampson's theory in the next section.

4.3 Slip Corrected Sampson's Theory

The pressure drop, ΔP, can be obtained from the rate of energy dissipation using[121]

$$\Delta P = \frac{2\mu}{Q}\int \omega^2 dV + \frac{4\mu}{Q}\int \left(\mathbf{u}\cdot\nabla\right)\mathbf{u}\cdot\mathbf{n}dS \tag{4.1}$$

where μ is the fluid viscosity, Q is the volumetric flow rate, ω is the vorticity, V is the volume and S is the surface of the boundaries of the system. The second term in equation (4.1) can be neglected assuming the velocity on the boundaries of S to be zero. Oblate spheroidal coordinates are used outside the orifice and cylindrical coordinates inside the orifice as shown in Figure 4.2a. x and t in the oblate spheroidal coordinates are related to the cylindrical coordinates z and r using

$$r^2 = \left(t^2 + (a+d)^2\right)\left(1-x^2\right) \tag{4.2}$$

$$z^2 = t^2 x^2 \tag{4.3}$$

where d is a virtual length, characterizing the slip length as discussed later in more detail, in the radial direction of the cylindrical coordinates. The vorticity in equation (4.1) can be expressed in terms of the stream function ψ using[122]

$$r\omega = -D^2\psi \tag{4.4}$$

where D^2 is a differential operator (see the Appendix for the definition of D^2). Using equations (4.1), (4.2), (4.3) and (4.4), the pressure drop can be rewritten as

$$\Delta P = \frac{4\pi\mu}{Q}\int_0^1\int_0^\infty \frac{1}{t^2+(a+d)^2 x^2}\left[\left(\frac{t^2+(a+d)^2}{1-x^2}\right)^{\frac{1}{2}}\frac{\partial^2\psi}{\partial t^2}+\left(\frac{1-x^2}{t^2+(a+d)^2}\right)^{\frac{1}{2}}\frac{\partial^2\psi}{\partial x^2}\right]^2 dtdx\,. \tag{4.5}$$

The exact stream function, $\psi^o = \frac{1}{2\pi}Qx^3$, which Sampson[119] obtained for flow through a zero-length orifice, when used in equation (4.5) results in the famous Sampson formula $\Delta P = \frac{3\mu Q}{a^3}$. To introduce the slip length, we use the Sampson stream function for $b < x \le 1$, and for $0 < x \le b$ (next to the wall) the stream function is set to zero as follows:

$$\psi = \begin{cases} \frac{1}{2\pi} Q x^3 & \text{for } b < x \le 1 \\ 0 & \text{for } 0 < x \le b \end{cases} \qquad (4.6)$$

where b in the oblate spheroidal coordinates corresponds to d (the virtual length within which the velocity is set to zero as shown in Figure 4.2b) in the cylindrical coordinates when $r = a$ at the edge of the pore ($t = 0$). The stream function in (4.6) satisfies the boundary conditions used in the original Sampson theory ($U_t = 0$ & $U_x = 0$ as $t \longrightarrow \infty$, $U_t = 0$ & $U_x = 0$ at $x = 0$ (outside the orifice tube) and $U_r = 0$ & $U_\phi = 0$ at $r = a + d$ (inside the orifice tube where $t = 0$)). ϕ is the angular coordinate inside the orifice tube. Using equation (4.2), b can be expressed in terms of the virtual length d as follows

$$b = \left(\frac{d}{a+d} \right) \left(1 + \frac{2a}{d} \right)^{\frac{1}{2}} . \qquad (4.7)$$

Slip length is related to the slip velocity, which is the t-component of velocity at $r = a$, using the relation $U_{\text{slip}} = \delta \frac{\partial U_t}{\partial r}$ at the pore $\left(U_t\left(t = 0 \,\&\, r = a\right) = U_{\text{slip}}\right)$. U_t can be obtained from the stream function ψ using

$$U_t = \frac{1}{r h_x} \frac{\partial \psi}{\partial x} = \frac{3Q}{2\pi} \frac{x^2}{\left(t^2 + (a+d)^2\right)^{\frac{1}{2}} \left(t^2 + \left(a+d\right)^2 x^2\right)^{\frac{1}{2}}}$$

(4.8)

where h_x is the scale factor in the oblate spheroidal coordinates (see the Appendix for the definition of the scale factors h_x, h_t and h_ϕ). The slip length δ (the ratio of U_t to $\frac{\partial U_t}{\partial r}$ at $t = 0$ and $r = a$) can then be expressed in terms of the virtual length d as

$$\delta = \frac{d^2 + 2ad}{a}. \tag{4.9}$$

Now using equation (4.6), (4.7) and (4.9), the pressure drop in equation (4.5) can be expressed in terms of the ratio of slip length to radius ($\alpha = \frac{\delta}{a}$). The Sampson formula corrected for slippage is, therefore, given by

$$R^{\text{Sampson}}_{\text{Slip-corrected}} = \frac{\Delta P}{Q} = \frac{3\mu}{a^3}\left[\frac{1+2\left(\frac{\alpha}{1+\alpha}\right)^{\frac{3}{2}} - 3\left(\frac{\alpha}{1+\alpha}\right)}{\left(1+\alpha\right)^{\frac{3}{2}}}\right]. \tag{4.10}$$

As $\alpha \to 0$ ($\delta \to 0$ or $a \to \infty$), when there is no slippage or the radius is very large compared to the slip length, the hydrodynamic resistance in equation (4.10) reduces to the original Sampson resistance ($R^{\text{Sampson}}_{\text{Slip-corrected}} \to R^{\text{Sampson}} = \frac{\Delta P}{Q} = \frac{3\mu}{a^3}$). The hydrodynamic resistance predicted by the slip-corrected Sampson formula normalized by that of the original Sampson formula $\left(\frac{R^{\text{Sampson}}_{\text{Slip-corrected}}}{R^{\text{Sampson}}} = \left[\frac{1+2\left(\frac{\alpha}{1+\alpha}\right)^{\frac{3}{2}} - 3\left(\frac{\alpha}{1+\alpha}\right)}{\left(1+\alpha\right)^{\frac{3}{2}}}\right]\right)$ as a function of the ratio of radius to slip length $\left(\frac{1}{\alpha} = \frac{a}{\delta}\right)$ is plotted in Figure 4.3. The slip-corrected Sampson's theory is able to match the hydrodynamic resistance from MD and NS simulations (used as the reference methods) for all the graphene pore radii and water-carbon interaction parameters except for small values of $\frac{a}{\delta}$ <1. Table C1 and Table C2 summarize all the MD and NS simulations in this study. The original Sampson's theory, however, fails to predict the hydrodynamic resistance from MD simulations for $\frac{a}{\delta}$ <300.

4.4 Viscosity Corrected Sampson's Theory

The slip-corrected Sampson formula underestimates the hydrodynamic resistance for small values of $\frac{a}{\delta} < 1$ as it does not account for the variation of the interfacial viscosity at the membrane in the MD simulations. The average effective interfacial shear viscosity (within the interface layer with a thickness of L_{int} =0.8nm) is calculated in MD simulations using the Green-Kubo formulation (see the Appendix for more information) to be μ_{int} =0.98 mPa.s. L_{int} is the distance from the graphene wall within which the viscosity variation takes place. To obtain the pressure drop from equation (4.5), the integration must be carried out such that the viscosity is μ_{int} =0.98 mPa.s for $0 < z \le L_{\text{int}}$ and μ_{bulk} =0.85 mPa.s elsewhere. The interval $0 < z \le L_{\text{int}}$ corresponds to $0 < t \le \frac{L_{\text{int}}}{x}$ in the oblate spheroidal coordinates using equation (4.3). Therefore, equation (4.5) can be rewritten as

$$\Delta P = \frac{4\pi}{Q}\int_0^1\int_0^\infty \mu(x,t)\, f(x,t)\,dt\,dx = \frac{4\pi}{Q}\int_0^1\left[\int_0^{\frac{L_{\text{int}}}{x}} \mu_{\text{int}}\, f(x,t)\,dt + \int_{\frac{L_{\text{int}}}{x}}^{\infty} \mu_{\text{bulk}}\, f(x,t)\,dt\right]dx \tag{4.11}$$

where $f(x,t)$ is the integrand in equation (4.5). The interfacial viscosity can be expressed in terms of the bulk viscosity and an excess viscosity ($\mu_{\text{int}} = \mu_{\text{excess}} + \mu_{\text{bulk}}$ where μ_{excess} =0.13 mPa.s for graphene). The pressure drop in equation (4.11) can be rewritten in terms of the excess and bulk viscosities as

$$\Delta P = \frac{4\pi\mu_{\text{excess}}}{Q}\int_0^1\int_0^{\frac{L_{\text{int}}}{x}} f(x,t)\,dt\,dx + \frac{4\pi\mu_{\text{bulk}}}{Q}\int_0^1\int_0^\infty f(x,t)\,dt\,dx \tag{4.12}$$

where the second term is simply the pressure drop in equation (4.5). Therefore, the total hydrodynamic resistance can be given by

$$R^{\text{Sampson}}_{\text{Slip-viscosity-corrected}} = R^{\text{Sampson}}_{\text{Slip-corrected}} + R^{\text{Sampson}}_{\text{excess-viscosity}} \tag{4.13}$$

where $R_{\text{Slip-corrected}}^{\text{Sampson}}$ is the slip-corrected Sampson formula in equation (4.10) and the hydrodynamic resistance due to the excess viscosity can be obtained from integrating the first term in equation (4.12) (the effect of slippage for viscosity corrected is neglected for simplicity) as follows

$$R_{\text{excess-viscosity}}^{\text{Sampson}} = \frac{6\mu_{\text{excess}}}{\pi a^3}\left[\tan^{-1}(\beta) + \ln\left(\frac{1}{\beta^2}+1\right)\left(\frac{3\beta}{2}+\beta^3\right) - \beta\right] \tag{4.14}$$

where β is the ratio of the interfacial layer thickness to radius ($\beta = \frac{L_{\text{int}}}{a}$). In Figure 4.3, the hydrodynamic resistance predicted by the slip and viscosity-corrected Sampson formula normalized by that of the original Sampson formula as a function of the ratio of radius of the pore to the slip length are compared with the MD simulations. The slip and viscosity-corrected Sampson's theory gives rise to a good match with the hydrodynamic resistance from the MD simulations even for small values of $\frac{a}{\delta}$ where the slip-corrected Sampson's theory fails. The additional resistance due to the excess interfacial viscosity is dictated by $\beta = \frac{L_{\text{int}}}{a}$. In Figure 4.4, the normalized additional resistance is plotted as a function of β. As $\beta \to 0$ ($L_{\text{int}} \to 0$ or $a \to \infty$), when the interfacial viscosity variation length is negligible or the radius is very large compared to the interfacial layer thickness, the excess viscosity hydrodynamic resistance approaches zero $\left(R_{\text{excess-viscosity}}^{\text{Sampson}} \to 0\right)$. The normalized $R_{\text{excess-viscosity}}^{\text{Sampson}}$ reaches a plateau beyond a critical β for which most of the hydrodynamic pressure drop takes place within L_{int} and L_{int} becomes comparable to the hydrodynamic pressure drop length. In Dagan's theory[96], the effective length over which the pressure drop takes place is given by $h^{\text{Dagan}} = h + \frac{3}{8}\pi a$. For $h = 0$, $\frac{h^{\text{Dagan}}}{a} = \frac{3}{8}\pi = 1.178$ which corresponds to the critical value of β at which the excess viscosity hydrodynamic resistance reaches a plateau.

4.5 Final Remarks

Sampson's theory has been used to describe the flow in ultrathin pores and to understand the entrance/exit hydrodynamic resistance in nanotubes. Here, we show that the pore slippage and the variation of viscosity at the membrane interface, which are not accounted for in the original Sampson's theory, play an important role in small-diameter ultrathin nanopores. We introduced a new set of formulas for the slip and viscosity-corrected Sampson's theory which results in good agreement with data from MD and NS simulations as well as experiments (see the Appendix). The ratio of slip length to radius of the pore is the key parameter in explaining the flow in ultrathin nanopores. The model presented here ideally works for circular pores in 2D materials. Aside from porous 2D materials, accurate estimation of entrance/exit hydrodynamic resistance is required in frictionless nanotubes (e.g., CNTs) to quantitatively describe the flow both inside and outside of the nanotubes. For example, estimation of slip lengths inside CNTs from experimentally measured permeation coefficients relies on the theories used to obtain the resistance at the ends and inside the CNTs, $R_{\text{total}} = R_{\text{Entrance-exit}} + R_{\text{CNT}}^{\text{HP}}$. R_{total}, which is typically obtained from experimental measurements[85], is dominated by $R_{\text{Entrance-exit}}$ and an error in estimation of $R_{\text{Entrance-exit}}$ can result in a significant error in calculation of $R_{\text{CNT}}^{\text{HP}}$ using which the slip length inside the CNT is extracted (see the Appendix for more information). The corrected Sampson theory, therefore, could help explain the reported discrepancies in CNT slip lengths between experiments and MD simulations[85]. In other words, the CNT slip lengths from MD simulations are consistent with those of experiments when the corrected Sampson theory is used (see the Appendix for more details).

4.6 Figures

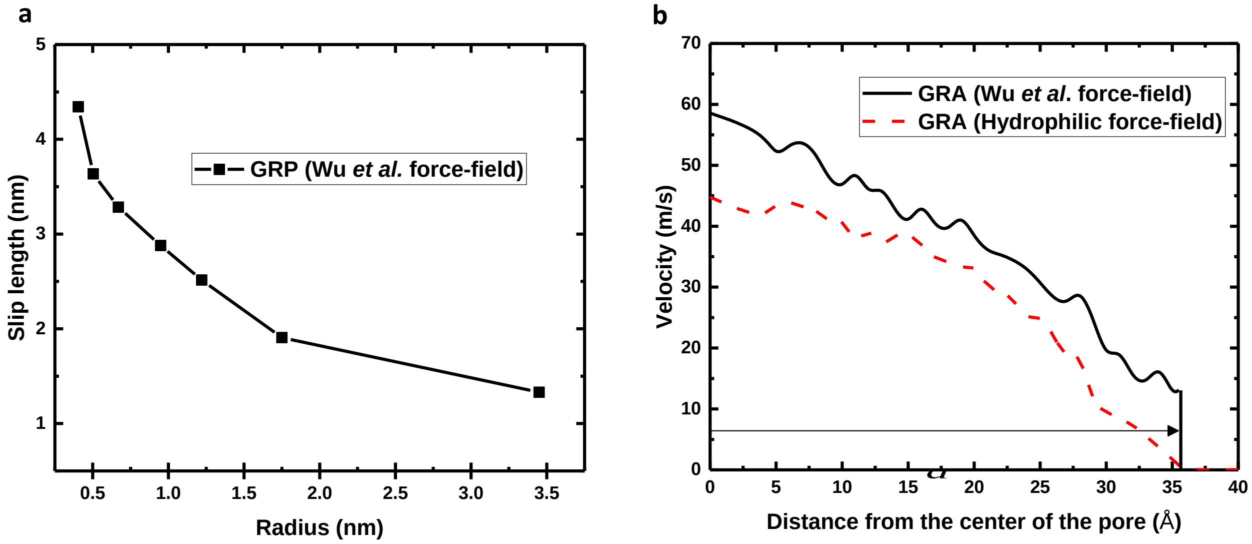

Figure 4.1 a. The slip lengths in the graphene nanopore are plotted for different radii (a). Finite slip lengths are obtained when using Wu *et al.*[68] force-field. **b.** Axial velocity profile in the single-layer graphene nanopore (a=3.54 nm) as a function of the radial distance from the center of the pore is plotted using Wu *et al.*[68] force-field (black solid curve) and a fictitious hydrophilic force-field ($\varepsilon_{\text{C-O}}$=0.9 kcal/mol, red dashed curve, (see Appendix)). The water accessible radius a is illustrated by an arrow. The water accessible radius is the length within which the water density is nonzero. In the Appendix, a systematic method of calculating the accessible radius is discussed.

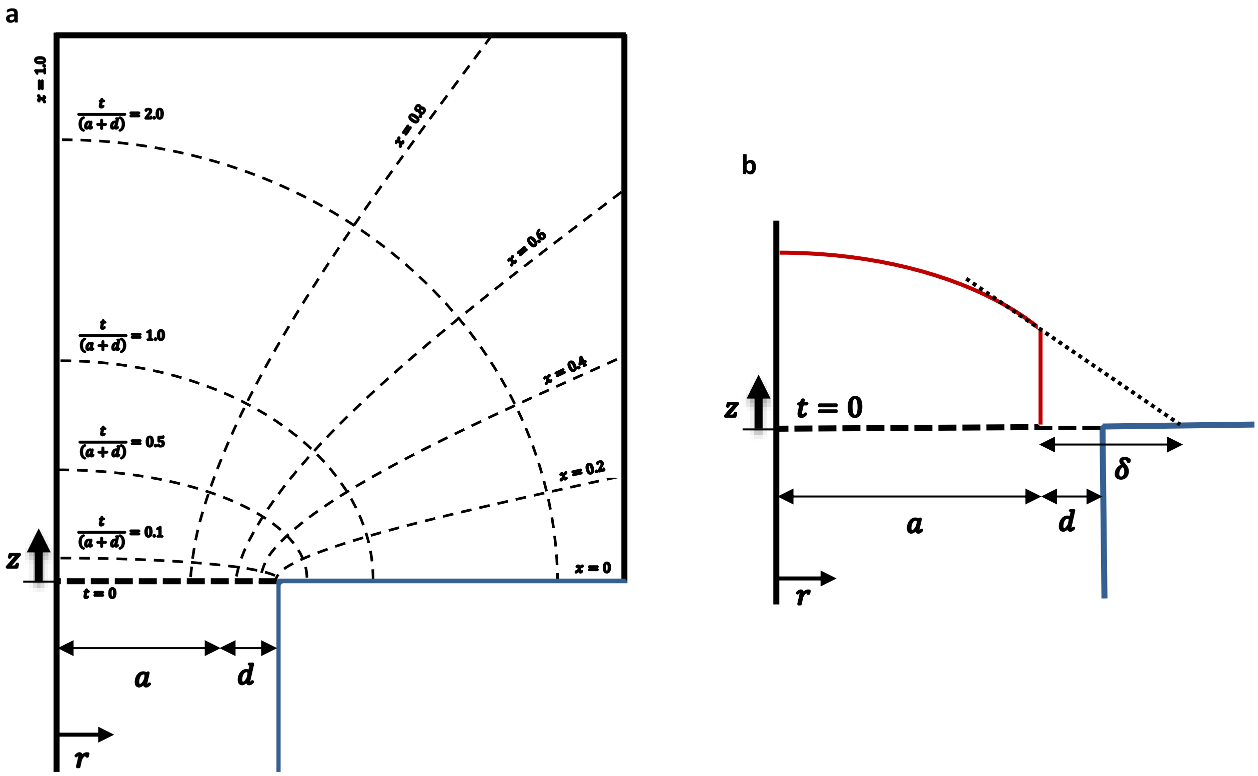

Figure 4.2 a. The confocal hyperbolas and ellipses (denoted by χ and t, respectively) in the oblate spheroidal coordinates are shown for an orifice of radius, a. The orifice boundaries are presented in blue. Inside the orifice, the radial distance from the center of the orifice (denoted by r) is shown by a solid arrow. The oblate spherical coordinates (outside the orifice) and the cylindrical coordinates (inside the orifice) are related by equations (4.2) and (4.3). **b.** The schematic of the velocity profile (red curve) and the lengths considered are shown. The dotted line is the tangent line to the velocity profile at $r = a$ whose intersection with $z = 0$ defines the slip length δ . d is a virtual length within which the velocity is zero. Note that the cylindrical sections of the two schematics have finite thicknesses (the actual pore thickness is zero in the theory) merely for the sake of clear presentation.

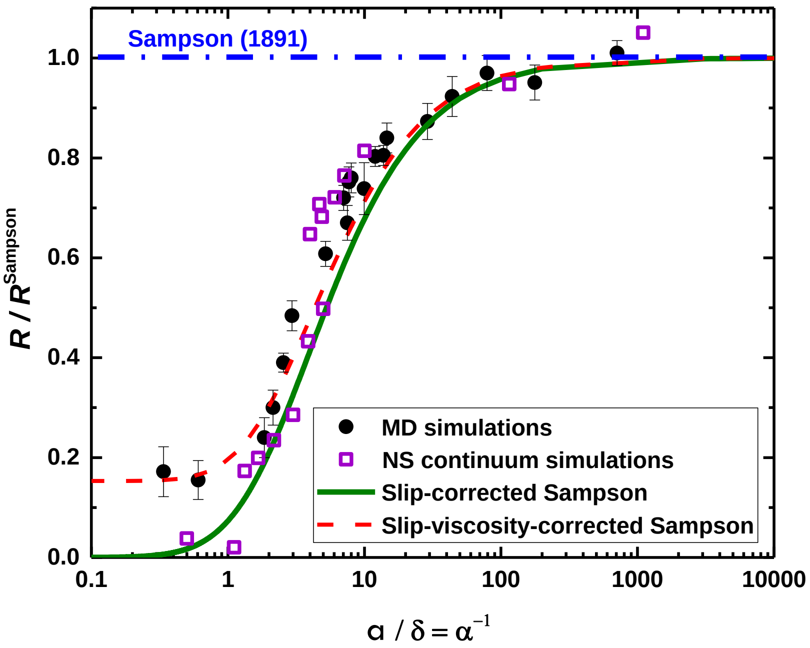

Figure 4.3 Comparison of the hydrodynamic resistance (*R*) obtained from MD simulations, NS continuum simulations and the corrected Sampson's theory to that of the original Sampson's theory (blue dash-dotted line) for different radius-to-slip length ratios $\left(\frac{1}{\alpha}=\frac{a}{\delta}\right)$. For smaller ratios (small radii or large slip lengths), the original Sampson formula overestimates the resistance from MD simulations (black solid symbols). The slip-corrected Sampson formula (green solid curve, equation (4.10)) describes the flow well from NS simulations (purple hollow symbols) as well as MD simulations. The inclusion of viscosity correction, in addition to the slippage, (red dashed curve, equation (4.14)) near the graphene interface leads to a good match with MD simulations (as viscosity variation take places in MD simulations (in NS simulations, the viscosity is assumed to be uniform)). For the viscosity-corrected curve, μ_{excess} =0.13 mPa.s, L_{int} =0.8 nm and a constant slip length of $\delta = 1.2$ nm are assumed.

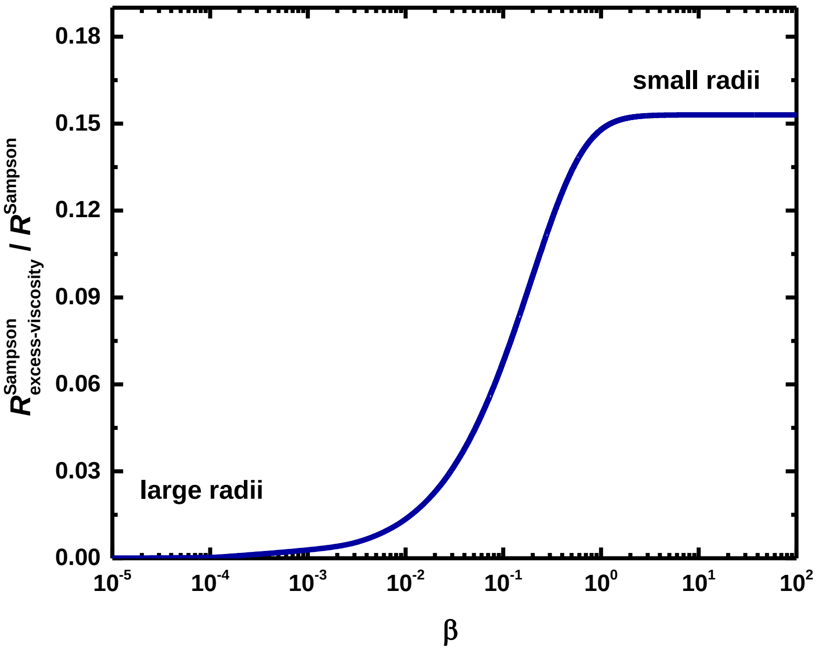

Figure 4.4 Hydrodynamic resistance due to the excess interfacial viscosity (equation (4.14)) normalized by the hydrodynamic resistance of the original Sampson's theory is plotted as a function of the ratio of the interface layer thickness to radius, $\beta = \frac{L_{\mathrm{int}}}{a}$. In equation (4.14), μ_{excess} =0.13 mPa.s, L_{int} =0.8 nm obtained from MD simulations. For small β (negligible interfacial viscosity variation or large radii), the excess hydrodynamic resistance is insignificant. For large β (when it is comparable to the ratio of the effective hydrodynamic pressure drop length to radius), the contribution of the excess resistance to the total resistance becomes important (as shown for small $\frac{a}{\delta}$ in Figure 4.3).

CHAPTER 5: Dynamic and Weak Electric Double Layers in Ultrathin Nanopores

5.1 Introduction

Recent advances[27,28] in nanotechnology have led to fabrication of nanopores in ultrathin membranes (*e.g.*, single-layer graphene, single-layer MoS_2) opening up new opportunities to explore novel applications ranging from water desalination[1,37,103,123], power generation[2,124] and disease diagnosis[4,5]. Of particular interest is the unique structural and dynamical properties of aqueous electrolytes in nanopores. Due to the unique chemistry and geometry of ultrathin nanopores, they have been shown to effectively reject salt ions allowing water molecules to pass through the pores at high rates[1,37] up to 10 L cm^{-2} per day per MPa. In addition, high ionic mobility, combined with strong charge selectivities, inside ultrathin nanopores has been demonstrated[2] to produce remarkable nanopower up to 10^6 W m^{-2} when a salinity gradient exists across the membrane. The high ionic mobility in ultrathin nanopores is justified by weakened ionic adsorption to the thin surface of the pores[2]. Ionic current blockade, which is used as a molecule identification signal in DNA sequencing and single biomolecule detection[3,6,18], is also shown to possess a high resolution in ultrathin nanopores as the thickness of ionic blockade region in the pore is comparable to the size of DNA nucleotides and amino acids of proteins. The experimentally and computationally unique observations in ultrathin nanopores is mainly because of the distinctive structure and dynamics of molecules inside these thin confinements as compared to thicker nanopores (*e.g.*, carbon nanotubes (CNTs), nanochannel slits). In thick nanopore, where the size of solid surface is much larger than the size of ions, an electric double layer (EDL) is formed at the solid-liquid interface[125]. Under the application of an electric field along the axis of the pore, EDLs in thick nanopores drag water molecules (solvent) resulting in a hydrodynamic flow known as electroomosis which has found numerous applications in micro- and nano-fluidic systems[126], fuel cells[127], *etc*. In field effect transistors (FET), the presence of EDL above the channel is shown to screen the charge of target molecules (*e.g.*, DNA molecules), which are outside the EDL away from the solid surface, hindering the sensitivity of the detection of target molecules[128]. The sensitivity increases with increasing the thickness of EDL characterized by the Debye length. EDLs have also drawn a great deal attention in the field of batteries and supercapacitors[129,130]. EDL capacitors are based on the adsorption of ions to the solid surface where a nanometer charge separation exists at the interface[131]. Given the fact that ultrathin nanopous membranes are emerging as one of the most versatile new materials, understanding the EDL or the ionic structure at their thin nanometer interface is of crucial importance.

Helmholtz[132] was the first one to discover that counter-ions in a solution are attracted to a charged surface (electrode) to neutralize the surface charge. In his simplistic model, the surface charge is counterbalanced by only counter-ions where the electric potential linearly changes from the surface to the counter-ions leading to a constant capacitance. This Helmholtz's description of EDLs fails to account for the ions adsorbed onto the surface as well as the diffusing ions in the solution. Later, Gouy and Chapman[133] independently discovered that the capacitance changes with applying an external potential invalidating the Helmholtz's model. In the Gouy-Chapman model, the surface charge is neutralized by diffusing counter-ions in the solution, known as the diffuse layer, in which the variation of ion concentrations next to the surface obeys the Maxwell-Boltzmann distribution. The Gouy-Chapman model, however, fails in highly charged surfaces as it does not account for the finite size of ions. Stern[134] introduced to the Gouy-Chapman model another layer, known as the Stern layer, where ions are ideally immobile and adsorbed onto a highly charged surface.

The interfacial properties in nanopores does not follow that of predicted by the classical models. As the ratio of surface area to solution volume is small inside ultrathin nanopores, the ionic structure is expected to differ from the classical EDLs. Here, using extensive molecular dynamics (MD) simulations, we study how the structure and dynamics of aqueous ions in single-layer graphene nanopores differ from that of thick

CNTs. In graphene nanopores, the variation of ion concentration and diffusion coefficient show that the ionic structure resembles mostly that of the bulk structure with no apparent Stern layer even for highly charged nanopore surfaces. In addition, ions and the surface are shown to be weakly correlated resulting in very short residence times as compared to thick CNTs. The weak wall-counter-ion correlation in ultrathin nanopores explains the observed rapid residence times as well as the fast dynamics of ions.

5.2 Results and Discussion

5.2.1 Structure and Dynamics of Ions

Each simulation involves water molecules, ions (potassium and chloride ions), two graphene sheets (the entrance and exit walls) and a CNT in between the sheets (see Appendix D for more details). For the ultrathin graphene nanopore, there is only one graphene sheet with water molecules and ions. (14,14), (26,26) and (37,37) CNTs with thicknesses (*h*) of 3.34 nm, 5.34 nm and 10.34 nm are considered (the dimension in *z* which is along the axis of the pores varies from 6 nm to 16 nm depending on the thickness). In the case of graphene nanopores, a similar pore size to that of CNTs is drilled in the middle of graphene sheets (*h*=0.34 nm). To maintain the degree of porosity of the nanopores, the dimensions in *x* and *y* (which lie in the plane of graphene sheets) vary from 6.25 nm to 12 nm depending on the diameter (see the Methods section for more details). In the equilibrated MD simulations, the number of potassium ions (K^+, which are the counter-ions as the pore surface carbon atoms are assigned negative charges with charge densities ranging from -0.0006 to -0.6 C m^{-2}) is calculated within 1.9nm-diameter nanopores for the ultrathin nanopore as well as the thickest CNT (*h*= 10.34 nm). The number of K^+ ions, which is an indication of the presence of an ionic layer or EDL inside the nanopores, is shown as a function of the simulation time in Figure 5.1. In the ultrathin nanopore, the presence of K^+ ions has a dynamic nature where an ionic layer exists at intervals with time scales of few picoseconds. As the thickness increases only by 3 nm (*h*=0.34 nm to *h*=3.34 nm), inside the nanopore, the ionic structure begins to assume a continuous and rigid EDL which is stable over the entire simulation time (>nanoseconds).

As observed, the dynamic nature of the ionic structure inside nanopores abruptly changes as we approach the ultrathin limit of a single-layer graphene. To shed more light into the structure and dynamics of K^+ counter-ions inside nanopores, the ion concentration and ion diffusion coefficient in the z direction are plotted as a function of the radial distance from the center of the pores in Figure 5.2. In the case of large-thickness CNTs (h=10.34 nm), an EDL is formed for both low and high surface charge densities. The structure of the EDL in the low surface charge density CNT, is consistent with the structures obtained in previous studies[125,135], where a counter-ion concentration peak is formed next to the wall and the co-ion concentration reduces featurelessly along the radial distance towards the wall. The counter-ion diffusion coefficient along the axis of the pore, is almost uniform with no features of ionic immobility. However, for the high surface charge density, we observe a giant counter-ion concentration peak and an almost vanishing ion diffusion near the charged wall. In addition, a strong packed layering of both co- and counter-ions is formed within just 0.2 nm of the wall surface. Comparing the ionic structure and dynamics in thick CNTs in the MD simulations to the ones predicted by the classical EDL models, the EDL in the low surface charge density CNTs, resembles the Gouy-Chapman EDL where a diffuse layer with a higher concentration of counter-ions is present (Figure 5.3a). The ion concentration variation, however, does not follow the exact Maxwell-Boltzmann in the Gouy-Chapman model. The properties of the EDL in highly charge thick CNTs are similar to those of the Gouy-Chapman-Stern model (Figure 5.3b) where an additional immobile Stern layer is formed next to the surface. For the single-layer graphene with a low surface charge density (Figure 5.2c), the ion concentrations are nearly homogeneous throughout the pore and are less than the bulk concentration (~1M) near the surface. The region next to the surface is highly concentrated with water molecules (see Appendix D). The counter-ion diffusion coefficient along the pore axis is uniform. Compared to the CNT with the same surface charge density, the diffusion coefficient is slightly higher inside the graphene nanopore. The structure and dynamics of ions inside the low surface charge density graphene pore does not resemble that of any of the EDL models as no diffuse layer nor Stern layer are present (see Figure 5.3c for the schematic of ions inside low surface charge density nanopores). Rather, in spite of the nanopore having a net charge, the nanopore acts like a point of zero charge[136]. In the high surface charge density graphene nanopore (Figure 5.2d), near the wall (which is highly concentrated with water molecules (see Appendix D)), a weak diffuse layer (Figure 5.3d) is formed where the concentration of counter-ions are less than or comparable to the bulk ion concentration. This diffuse layer differs from that of the Gouy-Chapman model as the counter-ion concentration in the model is expected to increase (high than the bulk value) near the wall. As the diffusion coefficient is nonzero near the wall, no indication of a Stern layer is available even for such a high surface charge density in the ultrathin nanopore.

5.2.2 Wall-Ion Correlation

To further investigate the dynamics of ions inside charged nanopores, the time correlation[125] between the counter-ions and the wall atoms is calculated using $C_{ij}(t) = \langle \theta_{ij}(0)\theta_{ij}(t) \rangle$, where i and j are a pair of particles (here, K^+ ion and carbon atom, respectively). θ_{ij} is 1 if i and j are nearest neighbors based on their first peak in the concentration plots and 0 otherwise. C_{ij} is the probability of a pair of particles being nearest neighbor from time 0 to t, therefore, the residence times of K^+ ion near the wall can be obtained from $\tau = \int_0^\infty C_{ij}(t)\,dt$. In Figure 5.4, the K^+-wall time correlation is plotted as a function of the simulation time in the ultrathin graphene nanopore and 10.34nm-long CNT for different surface charge densities. In graphene nanopore, the correlations die out rapidly regardless of the magnitude of surface charge densities. The calculated K^+ ion residence times are about 4.8 ps for all the surface charge densities. The rapid residence times suggest that forming a Stern layer is impossible in the ultrathin graphene nanopores within the practical range of surface charge densities. For the thick CNTs, the correlations die out quickly for low surface charge densities with K^+ ion residence times of about 15 ps. However, for large charge densities, K^+ ions and wall carbon atoms are highly correlated with residence time scales that are beyond the scope of the MD simulations. The tail of $C_{ij}(t)$ is extrapolated by fitting a curve into the available data from MD simulations. The residence times based on the extrapolated $C_{ij}(t)$ are found to be in order of seconds. The strong K^+ -wall correlation is a signature of ion immobility or the presence of a Stern layer near the wall. In the ultrathin limit of graphene nanopore, no Stern layer is observed regardless of the strength of the surface charge density which justifies the exceptionally fast dynamics of ions inside these nanopores both computationally and experimentally[2].

5.3 Conclusion

The structural and dynamical properties of aqueous ions in nanopores (especially ultrathin nanopores) have shown to differ the predicted properties by the classical theories. In our MD simulations, the formation of EDLs or the ionic structures at the nanopore interfaces begin to have an unstable and dynamic behavior as the thickness of nanopore reduces to that of a single-layer graphene nanopore. Unlike the EDL in thick CNTs where diffuse and Stern layers similar to that of the Gouy-Chapman-Stern model are observed, in the ultrathin nanopores, no Stern layer is present and a weak (lower than the bulk ion concentration) diffuse layer is only present for highly charged nanopores. The lack of Stern layer formation is shown to be due to the highly weak correlation between the counter-ions and the atoms of the wall with time. The weak correlation results in fast dynamics of ions with short residence times in ultrathin graphene nanopores. The critical ratio of surface area to solution volume is reached only for single-layer graphene nanopores (and other ultrathin 2D materials like MoS_2) for which ultra-fast residence times of counter-ions is observed.

5.4 Methods

MD simulations were performed using the LAMMPS package.[72] The simulation boxes contain 20,000-100,000 atoms depending on the thickness and diameter of pores with ions (potassium and chloride) having a molarity of ~1 (see Appendix D for more details). The SPC/E water model was used and the SHAKE algorithm was employed to maintain the rigidity of the water molecule. For nonbonded interactions of ions with water and carbon atoms, the mixing rule was employed to obtain the LJ parameters[137]. The carbon-water interactions were modeled by the force-field parameters given in Wu *et al*.[68] Since the carbon atoms are fixed in space, the interactions between carbon atoms were turned off. Flexible membranes add complexity to the calculation of different properties in the radial direction, therefore, the effect of flexibility is neglected. The LJ cutoff distance was 12 Å. The long range electrostatic interactions were calculated by the Particle-Particle-Particle-Mesh (PPPM) method.[100] Periodic boundary conditions were applied in all the three directions. For each simulation, first the energy of the system was minimized for 10000 steps. Next, the system was equilibrated using NPT ensemble for 1 ns at a pressure of 1 atm and a temperature of 300 K with a time-step of 1fs. With the graphene atoms held fixed in space, the NPT simulations allow the water to reach its equilibrium density (1 g/cm^3). Then, an additional NVT simulation was performed for 2 ns to further equilibrate the system. Temperature was maintained at 300 K by using the Nosè-Hoover thermostat with a time constant of 0.1 ps.[75,76] Finally, the production equilibrium simulations were carried out in NVT ensemble for ~20 ns.

5.5 Figures

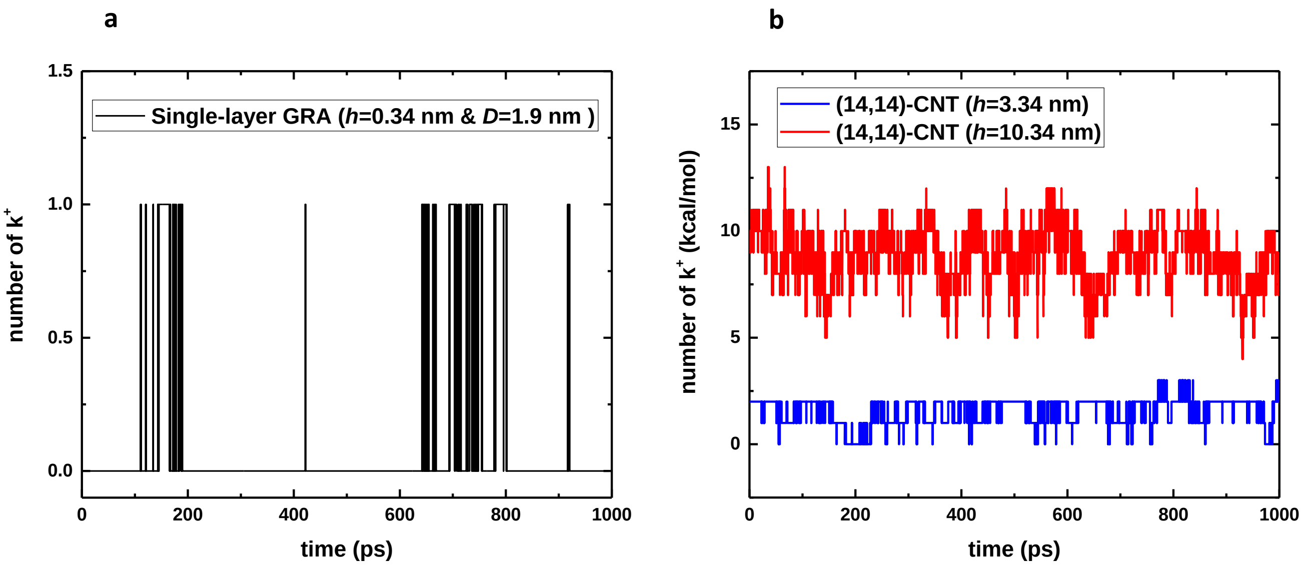

Figure 5.1 Number of potassium ions inside the nanopores as a function of simulation time are plotted for **a)** a single-layer graphene nanopore with a diameter of 1.9 nm and **b)** finite-length (14,14) CNTs with thicknesses of 3.34 nm and 10.34 nm. The graphene nanopores (denoted as GRP with *h*=0.34nm) and CNTs have similar diameters. The ionic layer inside the graphene nanopore has a dynamic nature with residence time scales of few picoseconds. Increasing the thickness of the pore by only 3 nm (departing from a single-layer graphene (ultrathin limit) to a CNT with *h*=3.34 nm) results in a giant increase in the residence times ($\gg$1 ns) where a continuous, rigid EDL exists in the CNTs.

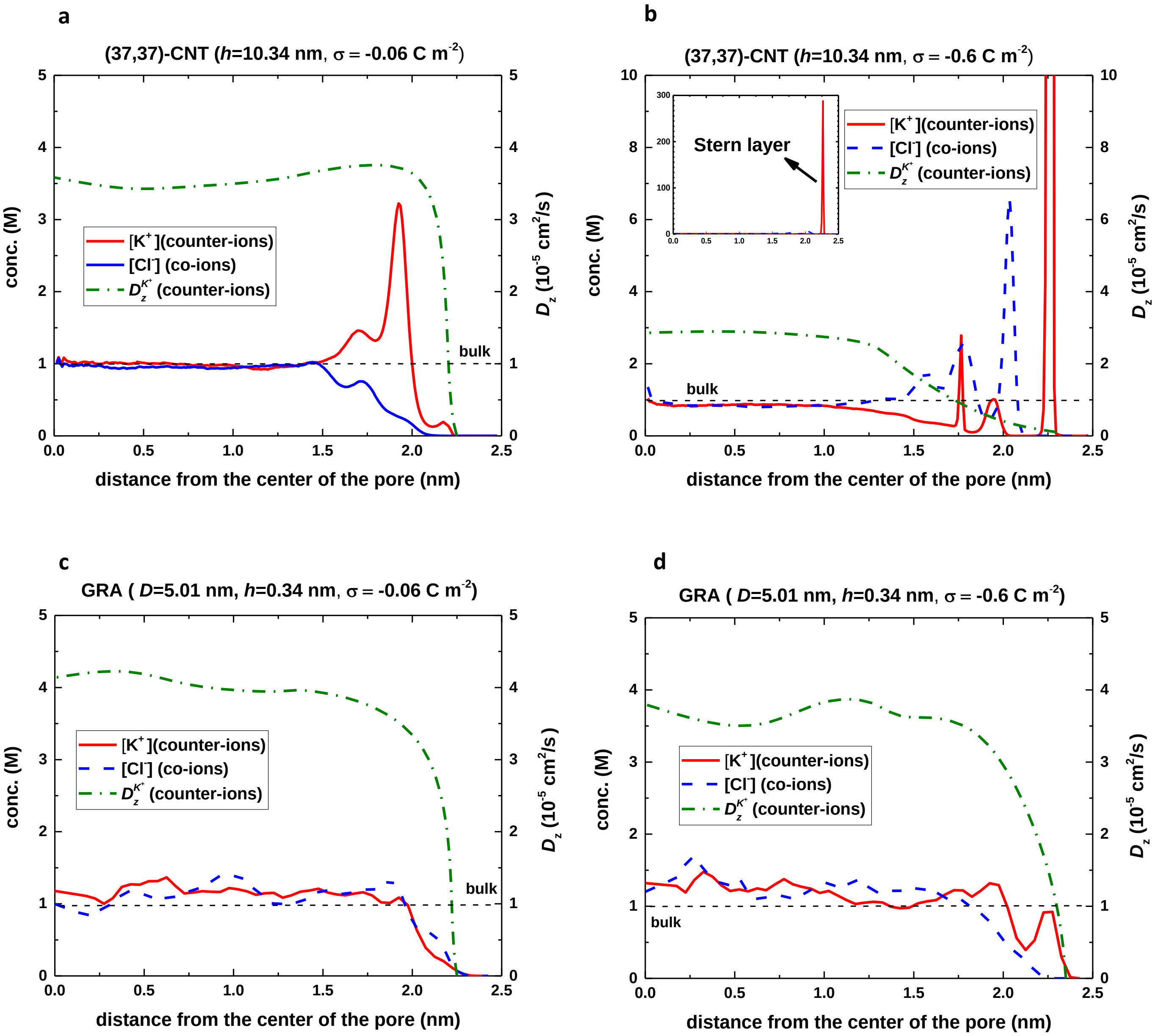

Figure 5.2 Ion concentration (left axis) and ion axial diffusion (right axis) are shown as a function the distance from the center of a 10.34nm-(37,37) CNT for **a)** low surface charge density of -0.06 C m^{-2} and **b)** high surface charge density of -0.6 C m^{-2}. Ion concentration and ion axial diffusion in a single-layer graphene with a similar diameter (5.01nm) are plotted for **c)** low surface charge density of -0.06 C m^{-2} and **d)** high surface charge density of -0.6 C m^{-2}. For low σ, a typical EDL is formed in the CNT with almost uniform counter-ion diffusion coefficient. In graphene nanopore with low σ, no EDL is formed and the diffusion coefficient is uniform. As σ increases, the counter-ion concentration in the CNT spikes near the surface where the diffusion coefficient starts to vanish indicating the presence of an immobile layer. In graphene nanopore with high σ, a weak EDL is formed where the counter-ions diffuse almost uniformly inside the nanopore.

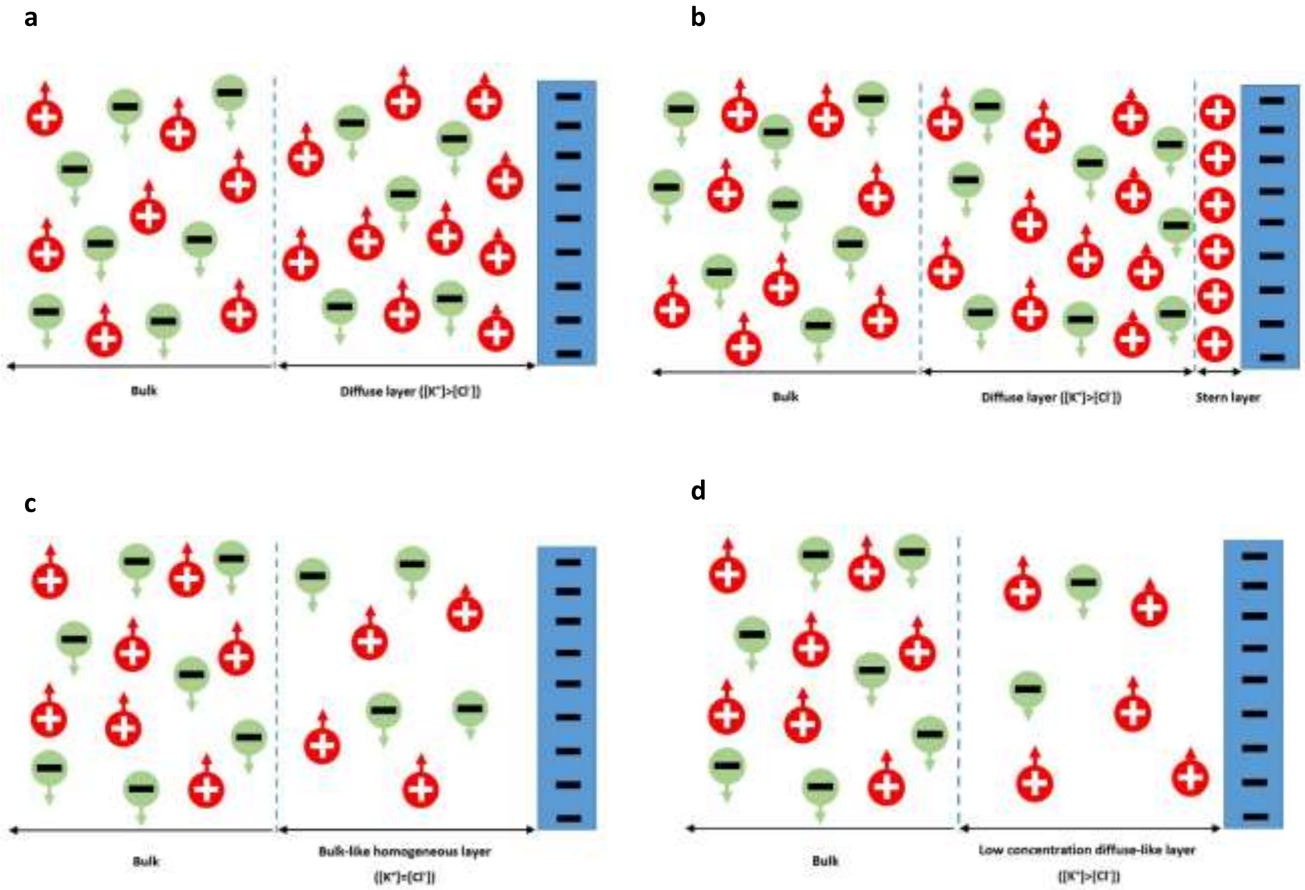

Figure 5.3 Schematics of observed ionic structure near a negatively charged graphitic surface (shown in blue) for **a)** a finite-length CNT with low surface charge densities, **b)** a finite-length CNT with high surface charge densities, **c)** a single-layer graphene nanopore for low surface charge densities and **d)** a single-layer graphene nanopore for high surface charge densities. Based on the results in Figure 5.2, for low surface charge density CNTs, a diffuse layer is observed similar to that of described by the Gouy-Chapman model. As the surface charge density increases, a Stern layer is formed near the surface wall similar to the description proposed by Gouy-Chapman-Stern model. In the ultrathin limit of the graphene nanopore, no apparent Stern layer are observed. Rather a homogeneous bulk-like layer or a diffuse layer (with smaller than bulk concentrations) is observed for low and high surface charge densities, respectively.

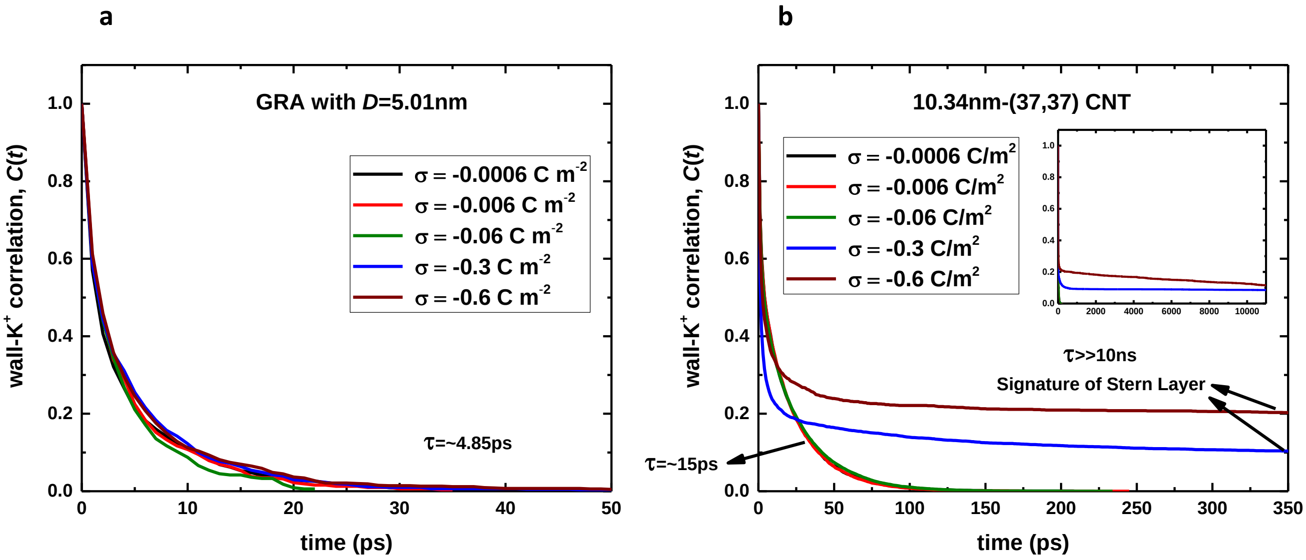

Figure 5.4 The correlation between potassium ions (counter-ions) with negatively charged carbon atoms the surface wall are shown as a function of simulation time in **a)** a single-layer graphene nanopore and **b)** a similar dimeter (37,37) CNT with a thickness of 10.34 nm for different surface charge densities. In graphene, regardless the surface charges, the correlation dies out quickly with residence times of about 4.85 ps. In the CNT, however, wall and potassium ions are highly correlated for large surface charge densities.

CHAPTER 6: Electro-Mechanical Signatures for DNA Sequencing through a Mechano-Sensitive Nanopore

6.1 Introduction

Nanopore-based DNA sequencing is attractive as it is a label-free, single-molecule approach that can be utilized for high precision DNA analysis.[15,18,138] Biological nanopores have been investigated for DNA base detection since they offer several advantages for single-molecule DNA analysis.[15,138-143] First, mutagenesis can be used to tailor the physical and chemical properties of biological nanopores;[18,143] Second, biological nanopores are synthesized by cells with an atomic level precision that may not be possible with solid-state fabrication approaches;[11] Third, crystallography data of protein channels is available at Angstrom length scales.[11,15,18,139] The first biological nanopore investigated for sequencing DNA was staphylococcal Alpha-Haemolysin (αHL) protein pore[144]; an applied potential translocated a ssDNA molecule through the pore giving rise to modulation of the ionic current.[140] αHL cylindrical beta barrel (with a diameter of 2 nm and length of 5 nm) is not tight enough to yield a distinguishable ionic current specific to individual nucleotides and therefore, exhibits small current differences between the nucleotides. Another well-researched biological nanopore for DNA sequencing is Mycobacterium Smegmatis Porin A (MspA).[145,146] MspA has been shown to provide better ionic current signals for differentiating nucleotides as its pore structure includes a tighter 1.2 nm constriction region.[146] In contrast to synthetic nanopores, such as graphene[147-149] and MoS_2 nanopores[27,40] where DNA base could be electronically read through transverse tunneling current,[150-152] ionic current is the only signature that has been acquired in biological nanopores, e.g. in MspA or αHL. The noise in the system and the presence of multiple bases in these nanopores make detection of a single DNA base difficult.[18] Acquiring another signal, in addition to ionic currents, for DNA detection using biological pores can significantly increase the accuracy of DNA sequencing.

The sensing of mechanical tension and force within a cell's environment is mostly mediated by a highly specialized class of membrane proteins known as Mechanosensitive (MS) ion channels.[146] MS channels were shown to be able to transduce mechanical tension into an electrochemical response[153]. When a cell membrane is under tension due to osmotic down shock, MS channels relieve the pressure of the cell by gating and forming a pore as big as 3 nm in diameter.[154,155] Among several types of MS channels, the mechano-sensitive channel of large conductance (MscL) of prokaryotes has been most extensively characterized.[154,156-161]

Here, we demonstrate for the first time that a MscL nanopore can be used for detection of DNA bases by modulating tension and strain in MscL. Tension in the MscL membrane, along with the ionic currents, can be used for more precise sequencing of DNA (see the cartoon representation of the system in Figure 6.1a). Unlike αHL or MspA, that are structurally wide open pores, initially closed MscL pore opens as a ssDNA translocates through the pore due to an applied electric field. MscL adjusts its pore size to the size of DNA bases during the translocation. The distinct tension in the protein associated with each nucleotide can be sensed through the strain and tension induced in the lipid bilayer. Recently,[162] MscL has been successfully embedded and characterized inside a droplet interface bilayer (DIB). It has been shown that the induced tension inside MscL is translated into a change in the triple point angle of DIB. By monitoring the angle change in DIB during DNA translocation, induced tension can be measured and quantified.

Two well-known challenges of DNA detection through nanopores are the fast translocation speed of DNA and noise.[11,15,18] Experiments have shown that DNA passes through αHL with a speed of 1base/μs, requiring MHz signal measurements to differentiate between nucleotide types.[15,18] The presence of multiple bases in the pore and thermal fluctuations in the system generate noise in the ionic current, making detection difficult. A MscL nanopore is flexible[163] and it adjusts to DNA size, causing a reduction in the speed of translocation. We demonstrate the slower translocation of DNA in MscL by comparing the results in MspA nanopore. Furthermore, we demonstrate the effect of pore flexibility by comparing the results in MscL and MspA pores.

6.2 Methods

We performed molecular dynamics (MD) simulations with NAMD 2.6 using the Petascale Blue Waters machine. [164] A typical simulation set up consisting of ssDNA, MscL protein, lipid bilayer, water and ions (~600,000 atoms) is shown in Figure 6.1b. We used the closed MscL model provided by Sukharev et al. and the crystal structure was obtained from Chang *et al*.[146,153]The C alpha segments were eliminated to obtain a reduced version of MscL.[146,153] A lipid bilayer (POPC) patch was created (10 nm×10 nm) to accommodate the protein and solvated by a 25-Å thick slab of water on each side of the membrane. MscL with the center of the pore aligned along the membrane normal axis (z-axis) was placed in the lipid bilayer using Visual Molecular Dynamics (VMD).[73] We ran the simulation for 40 ns to equilibrate the system of lipid bilayer and protein. This long equilibration makes sure that the protein is firmly placed in the membrane without any membrane leakage. Using the equilibrated lipid-protein system, ssDNA was placed at the mouth of the MscL nanopore with the ssDNA axis (z-direction) aligned along the protein axis (Figure 6.1b). Then, ssDNA (one at a time), MscL and lipid bilayer are submersed in water and salt ionic solution. The ionic concentration of NaCl is 0.5 M. We used polydA(60), polydC(60), polydT(60) and polydG(60) to create 4 simulation boxes (Figure 6.1b) differing only in ssDNA type. We used the CHARMM27 force field[165] parameters for the protein, nucleic acid (DNA), TIP3P water molecules and ions. SHAKE algorithm was used to maintain the rigidity of the water molecules. Periodic boundary condition was applied in all the three directions. The cut off distance for the LJ interactions was 15 Å. The long-range electrostatic interactions were computed by using the Particle-Mesh-Ewald (PME) method. The time step is selected to be 1 fs. For each simulation, energy minimization was performed for 100,000 steps. System was then equilibrated for 5 ns with NPT ensemble at 1 atm pressure and 300 K temperature. NPT simulation ensures that the water concentration is equal to the bulk value of 1 g/cm^3. The simulation was then performed in NVT ensemble. Temperature was maintained at 300 K by applying the Nosè-Hoover thermostat with a time constant of 0.1 ps. Before applying the electric field, equilibration for 2 ns was performed in NVT. Production simulations were performed by applying an external electric field in the z-direction. The external electric fields are reported in terms of a transmembrane voltage difference $V = EL_z$, where E is the electric field strength and L_z is the length of the simulation system in the z-direction.[148] For computational efficiency, we used steered molecular dynamics (SMD) to pull DNA with a very slow velocity of 0.00001 Å/fs. The steering forces were applied to all the atoms (both charged and uncharged) of the first base entering the pore. We monitored the time-dependent ionic current, *I(t),* in the pore. We computed the ionic current through the nanopore by using the definition of current, $I=dq/dt$, as $I(t)=\frac{1}{L_z}\sum_{i=1}^{n} q_i\left[\frac{z_i(t+\delta t)-z_i(t)}{\delta t}\right]$, where the sum is for all the ions, δt is chosen to be 5 ps, and z_i and q_i are the z-coordinate, charge of ion *i*, and *n* is the total number of ions, respectively. The ionic current data is averaged for each base, and the average current per base was reported.

To characterize the tension in the protein due to nucleotide translocation, the interaction forces between MscL helices and DNA bases were calculated. Subunits of MscL containing M1, M2 and S1 helices are shown in different colors in Figure 6.1c. Since MscL has five identical subunits, pair interaction calculations were carried out separately for each subunit. Both Coulombic and VdW (Van der Waals) forces by DNA bases on the inner transmembrane helix (M1) and the S1 helix (Figure 6.1c) were computed every pico second and then averaged over the entire DNA translocation time for each subunit of MscL. Only the inner M1 and S1 helices which create the constriction regions (Figure 6.1c) inside MscL were considered and the outer helices (M2) were ignored. The radial components of the calculated forces directed away from the center of the protein channel were then spatially averaged over all the five identical subunits of MscL to obtain an average force per subunit corresponding to each DNA base type. The nature of these forces is tensile and, therefore, the induced tension in MscL is transferred to the membrane since its segments are radially pushed outward by ssDNA. We refer to these interaction forces between ssDNA and protein lining residues as tension. It's notable that the origin of this tension is different from the tension defined as the membrane tension which causes MscL to gate.

6.3 Results and Discussion

We found 4 different tension signals for bases A, C, G and T which can be used for detecting and discriminating between nucleotides (Figure 6.1d). We observed that the maximum induced force is from base T, and the order of the induced forces is T>G>C>A. The force between ssDNA and MscL is from VdW and electrostatic interactions. Prior work has shown that a 70 pN force can open the MscL protein channel, therefore, the range of 20-120 pN forces induced from translocation of different bases should be adequate for the discrimination of bases.[155,160] Also, using magnetic tweezers, it's possible to measure forces as small as 50 fN,[166] therefore, forces of 20 pN magnitude should be measurable. These forces on the wall of the protein channel have a local effect on the lipid bilayer. The effect of the forces and tension is maximum on the lipids in the vicinity of MscL, therefore, the force measurements need to be done on the lipids, close to the protein. To understand why base T induces a maximum force, we investigated the structure and interaction parameters of each base. Base T has two protruding oxygen atoms and this is the maximum number among all the bases (more information about the structure of bases and their interaction strength can be found in Appendix E). Oxygen plays a significant role in both VdW and electrostatic forces between MscL lumen lining residues and nucleotides. The Lennard-Jones (LJ) energy interaction parameter of the oxygen atom is higher ($\varepsilon_O=0.210$) compared to all the other atoms ($\varepsilon_H=0.05$, $\varepsilon_C=0.1$, $\varepsilon_N=0.17$)[167] of the base. Base A has only hydrogen terminations (no oxygen), therefore, it has the lowest interactive forces among all the bases (Figure 6.1d). Comparing the termination structure of bases G and C reveals the existence of two nitrogens and one oxygen for base G, and only one nitrogen and oxygen for base C . The extra nitrogen in base G compared to base C gives rise to the higher interaction forces between MscL and base G and this fact explains the interaction forces order (G>C).

Unlike other biological pores (MspA or αHL) and solid-state nanopores which are normally-open, MscL has a flexible pore as it opens according to the size of the base, i.e., in our simulations, initially, MscL opens with evolving pore radii during the translocation of the first 5-10 bases. In the calculation of forces, we ignored the force data from the initial entry of ssDNA (for all PolydA, PolydC, PolydG and PolydT) into

MscL because these forces are not in equilibrium and the pore exhibits transient dynamics. In Figure 6.2a, we show three states of the pore representing the pore opening and expansion. State 1, state 2 and state 3 refer to closed, transient opening (while the first bases of PolydA are about to exit the cytoplasmic segment of MscL) and fully-opened by polydA states, respectively. Interestingly, MscL pore has an elliptical shape when it is fully open (Figure 6.2a). It is notable that in normal operation of MscL, in both intermediate and open states, MscL pore is circular and symmetrical.

We computed the average ionic current for each base (averaged during the translocation of each polydna with 60 bases) and found the current to decrease in the order, C>A>G>T. The ionic currents of bases C and A are close to each other and higher compared to bases G and T. Most of the ions that passed through the pore are cations which are dragged by the negatively charged backbone of the DNA during the translocation of all the 60 bases. Very small number of ions are trapped between the bases and dragged down the pore. Water molecules are observed in the pore all around the DNA. To illustrate the effect of pore elasticity of MscL on the quality of the acquired ionic current signal, we compared the ionic current signals for both MscL and MspA nanopores (Appendix E). According to the literature, MspA has been found to be the best biological pore, reported so far, for DNA detection.[15,66,145,168] The maximum and minimum current difference, ΔI, is 113.1 pA and 189.2 pA for MspA and MscL, respectively (Appendix E). Higher ΔI for MscL compared to MspA shows a better detection signal for MscL. We also investigated the noise by computing the signal to noise ratio, SNR, for both MscL and MspA pores. SNR is 6.13 (with $I_{noise,RMS}$=30.99 pA) and 4.21 (with $I_{noise,RMS}$=26.84 pA) for MscL and MspA, respectively (Appendix E). To compare the noise for static and moving ssDNA, we performed simulation of moving ssDNA by applying bias (500 mv) and static ssDNA when ssDNA is inside MscL and the applied bias is zero. We used the same method of noise calculation that we used in SNR computation (Appendix E). The ratio of noise generated in static ssDNA case ($I_{noise, RMS: Static}$) and noise generated in moving ssDNA case ($I_{noise, RMS:Moving}$) , is $I_{noise, RMS:Static} / I_{noise, RMS:Moving}$ =0.985 which means the noise is very similar in both cases. The signal becomes strong (or the SNR is improved) when a strong bias (no SMD) is applied leading to a high DNA passage rate.

Therefore, DNA translocation rate is indirectly related to the strength of the signal and consequently the signal to noise ratio.

The fluctuations in current are dependent on the slit diameter, slit length and the charged lining residues of the slit. In MscL, the diameter of the pore is flexible and adaptive to the ssDNA nucleotide type. We believe this flexibility, and perhaps selectivity reduces the noise level, as noted in the SNR comparison of MspA and MscL. The distinctive ionic current features in MscL can be attributed to two fundamental differences between the operation of MscL and other biological nanopores. First, in MscL, the pore is initially closed and it opens due to the electric field-mediated translocation of ssDNA, unlike in other nanopores where a fixed pore diameter is employed. Second, unlike MspA, Alpha-Hemolysin, Si_3N_4, graphene and MoS_2, MscL has two constriction regions which open during ssDNA translocation (see Figure 6.1c). Bases C and A have larger ionic currents (Figure 6.2b), revealing the fact that these bases are capable of transporting ions through the constriction regions with higher rates. To understand how the MscL pore opens during the translocation of bases, we time-averaged the pore radius during ssDNA translocation (Figure 6.3a). Base A creates the largest pore diameter and base T creates the smallest pore diameter in constriction 1, constriction 2 and open regions of the MscL channel. (Figure 6.3a). The minimum ionic current is for base T (Figure 6.2b) and this is consistent with the minimum opening of the pore induced by base T in all the segments of MscL (Figure 6.3a). The order of pore radii opened by ssDNA in constriction regions 1, 2 and open region is A>G>C>T. Bases A and G (purines) have an additional ring compared to bases C and T (pyrimidines) which gives rise to larger base area of purines and the consequent larger pore radii in MscL compared to pyrimidines (Appendix E).

The normal activation of MscL by tension in the lipid bilayer has two open states – intermediate and fully-open. In the closed state, the S1 segments form a bundle, and the crosslinking of S1 segments prevents the opening of the channel (Figure 6.1c). When a tension is applied to the membrane, the transmembrane barrel-like structure expands and stretches apart the S1-M1 region allowing the channel to open (Figure 6.1c). The transition from the closed to the intermediate state includes small movements of the M1 helix. Further transitions to the open states are characterized by large movements in both M1 and M2. The gating pathway for ssDNA translocation through MscL is, however, different. We compared the conformational changes occurring in the pore lumen due to ssDNA translocation with the normal operation of MscL (Figure 6.3b). The average pore radius for the 3 stable structures of MscL and ssDNA-opened MscL are shown in Figure 6.3b. The minimum pore radii are 0.0 Å, 2.1 Å and 12.5 Å for the closed, intermediate and open states, respectively (Figure 6.3b). For the ssDNA translocation case, MscL radius is between closed and intermediate states (Figure 6.3b). It can be inferred from the radius of ssDNA–opened MscL that this state of MscL is not stable; tending to relax to closed state. Another striking difference between ssDNA-opened and normally-opened MscL is the mechanism of gating. In the normal operation of MscL, transmembrane helices M1 (Figure 6.1c) rotate and tilt such that they become more aligned with the plane of the membrane and M2 helices also tilt but to a much lower degree[155,160] resulting in a shortened length of MscL (Figure 6.3b). In the ssDNA-opened MscL, the initially closed-state length of MscL does not change and all M1, M2 and S1 segments expand radially (Figure 6.3b).

An important challenge of DNA sequencing through a nanopore is to decrease the high speed of translocation. If the translocation speed can be reduced to about one base per millisecond, then single-base detection can be more easily performed in experiments. It has been shown that translocation speeds can be reduced by increasing the solvent viscosity or decreasing the temperature,[15] but these methods could not reduce the translocation speed to a desired level.[15] To reduce the translocation speed, an initially-closed, and a translocation-induced elastic opening of the pore could be a potential solution. In this regard, MscL has the potential to significantly reduce the translocation speed. We compared the translocation speed of ssDNA through MscL and MspA[169] (Figure 6.4). MspA is an octameric protein with a pore suitable for DNA sequencing[169,170] (Figure 6.4a). We simulated DNA translocation keeping all conditions identical and only differing in the type of the protein. Two biases of 500 mV and 1.0 V were applied to both simulation cases to compare their speed of translocation. Translocation speed of ssDNA in MscL is 11-17 times slower than in MspA (Figure 6.4b and 6.4c). For the bias of 500 mV, the speed of translocation is 0.129 Å/ns and

2.24 Å/ns for MscL and MspA, respectively (17.36 times slower in MscL than in MspA). The reduction in speed can be attributed to two fundamental differences between these pores: 1. The comparison between MscL and MspA protein structures reveals the existence of multiple constrictions in MscL with near zero diameters where as in MspA, only one constriction region with a 1.2 nm diameter is present (Figure 6.4a). These structural differences help reducing the speed of translocation in MscL to a large extent. 2. MspA has an open pore structure and remains roughly intact during translocation, whereas MscL opens to an extent just enough to accommodate the ssDNA bases. Since ssDNA-opened MscL does not reach an intermediate stable state, it tends to close during DNA translocation, which results in exerting force on ssDNA and reducing the speed. Based on the interaction force calculations, LYS 31, GLU 9, ARG 13 and ASP 18 residues in MscL have the highest interaction forces with ssDNA, giving rise to slower translocation of ssDNA. Interestingly, all these residues are located in constriction regions 1 and 2. It is notable that the S domain plays a critical role in the creation of highly constricted regions in MscL. The highly constricted regions in MscL give rise to the selectivity of the passage of ions for each nucleotide which increases the SNR. Also, the highly constricted regions created by S1 domain have a significant effect on reducing the DNA translocation speed.

6.4 Conclusion

We have shown that a mechanical signature, namely tension in the membrane, can be effective for DNA detection through a mechano-sensitive channel of large conductance, MscL. Four distinct force signals were detected for bases with forces decreasing in the order T> G> C>A. An initially-closed MscL opens to ssDNA due to electric-field mediated translocation and the pore geometry adapts to the size of each base. Ionic current signal is also distinct for each base, making MscL pore amenable for detecting bases with two parallel signals, namely, membrane tension and ionic current. We found a completely different gating mechanism of MscL during ssDNA translocation compared to its normal operation. The translocation speed of DNA in MscL is roughly one order of magnitude slower compared to that in MspA.

6.5 Figures

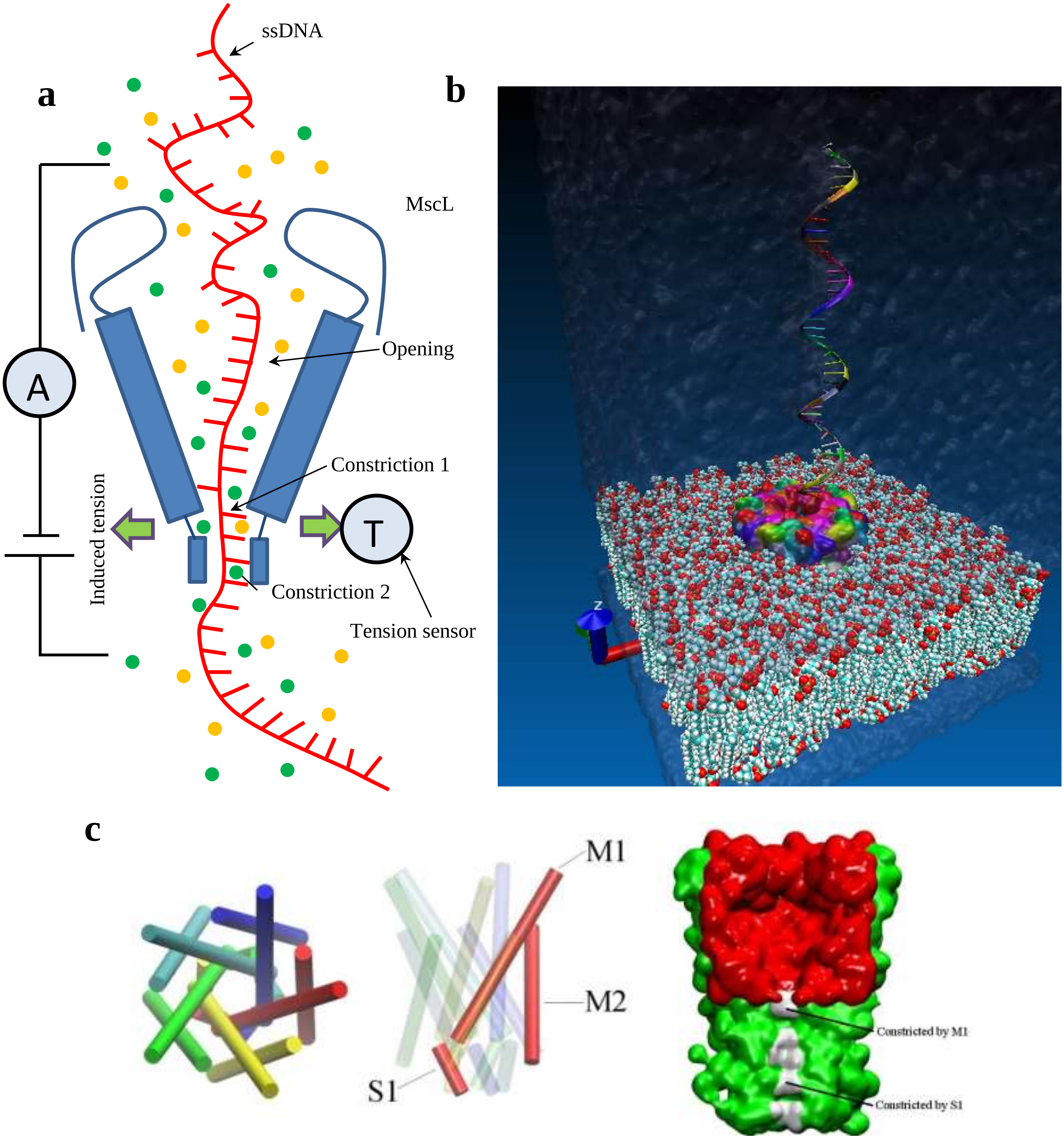

Figure 6.1 (cont.)

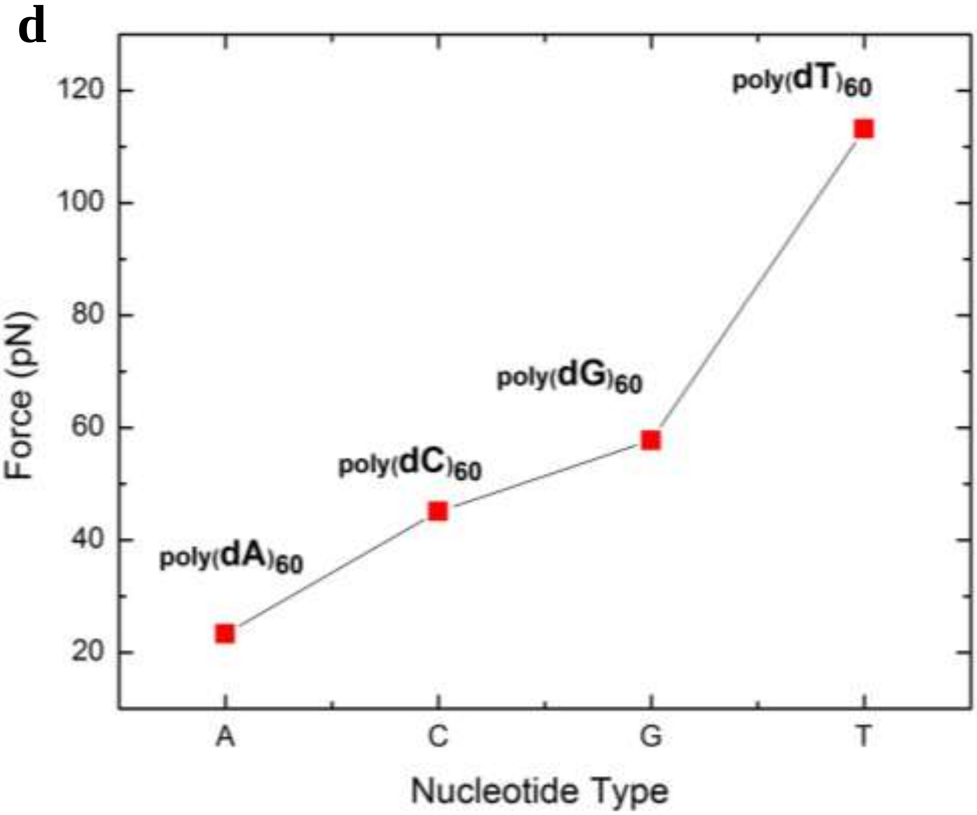

Figure 6.1 a) Cartoon representation of the system (MscL, ssDNA, ions) demonstrating two parallel signals: tension and ionic current. **b)** Visualization of the simulation setup comprising ssDNA, MscL protein, lipid bilayer and water. **c)** Left: Top view of MscL. Middle: side view of MscL with the designation of M1 and S1 helices. Right: Pore architecture of MscL, cut in the middle and the location of the two constriction regions of MscL. **d)** Force (averaged) induced in the membrane due to the presence of each base in MscL.

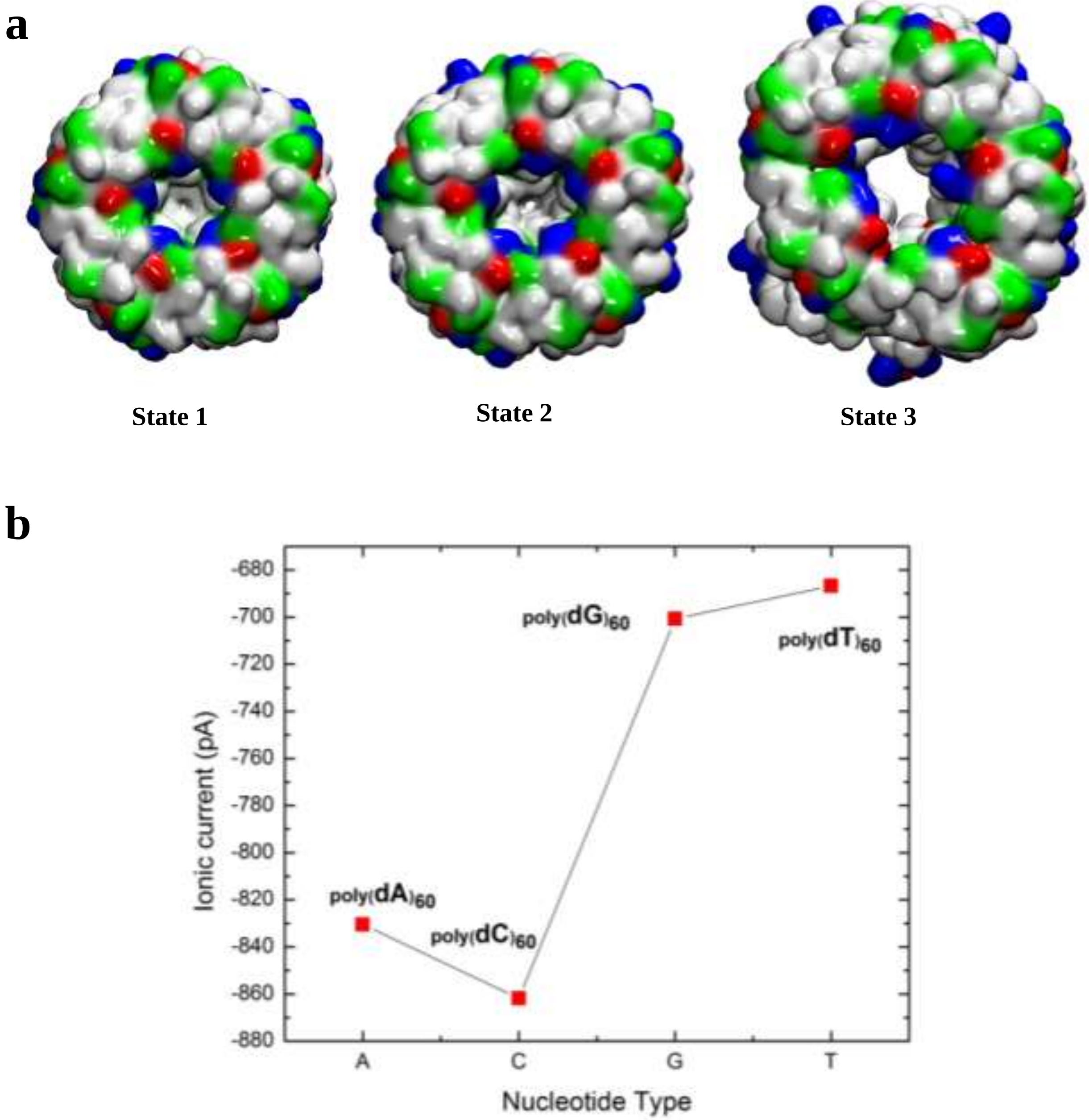

Figure 6.2 a) Three representative states of the MscL pore and the extent to which it opens, *state1*: initially-closed state prior to the ssDNA entry, *state 2*: the first base of ssDNA entered the pore and is about to exit the cytoplasmic segment of the pore (the pore opens partially), *state 3*: ssDNA with 60 bases (here, polydA) translocated and pore has an elliptical shape. **b)** Average ionic current for different nucleotide types.

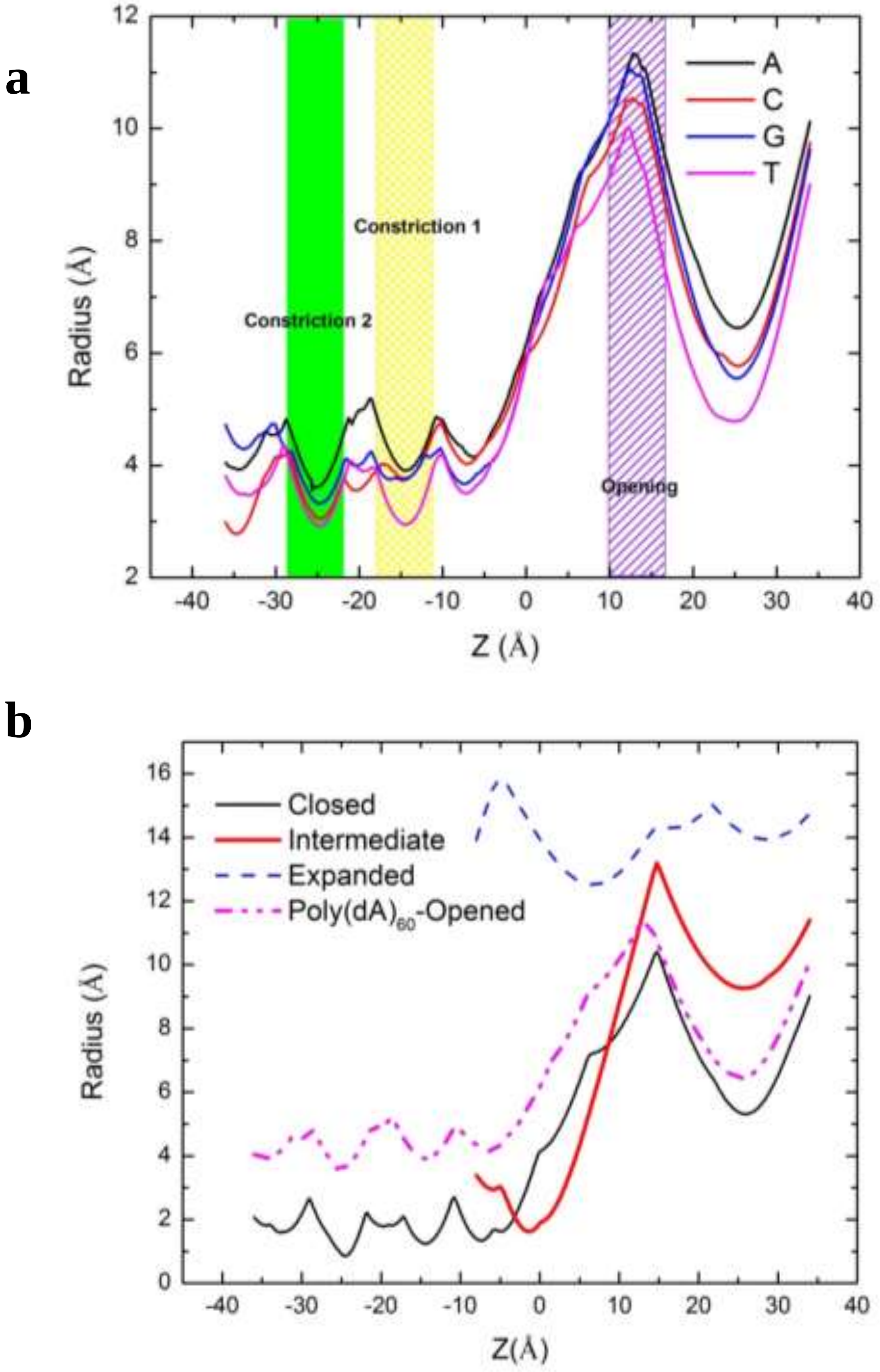

Figure 6.3 a) Average pore radius of MscL during translocation of Poly(dA)$_{60}$, Poly(dC)$_{60}$, Poly(dG)$_{60}$ and Poly(dT)$_{60}$. **b)** Pore radius for 3 stable states of MscL (closed, intermediate and expanded) and its comparison with the pore radius for translocation of Poly(dA)$_{60}$.

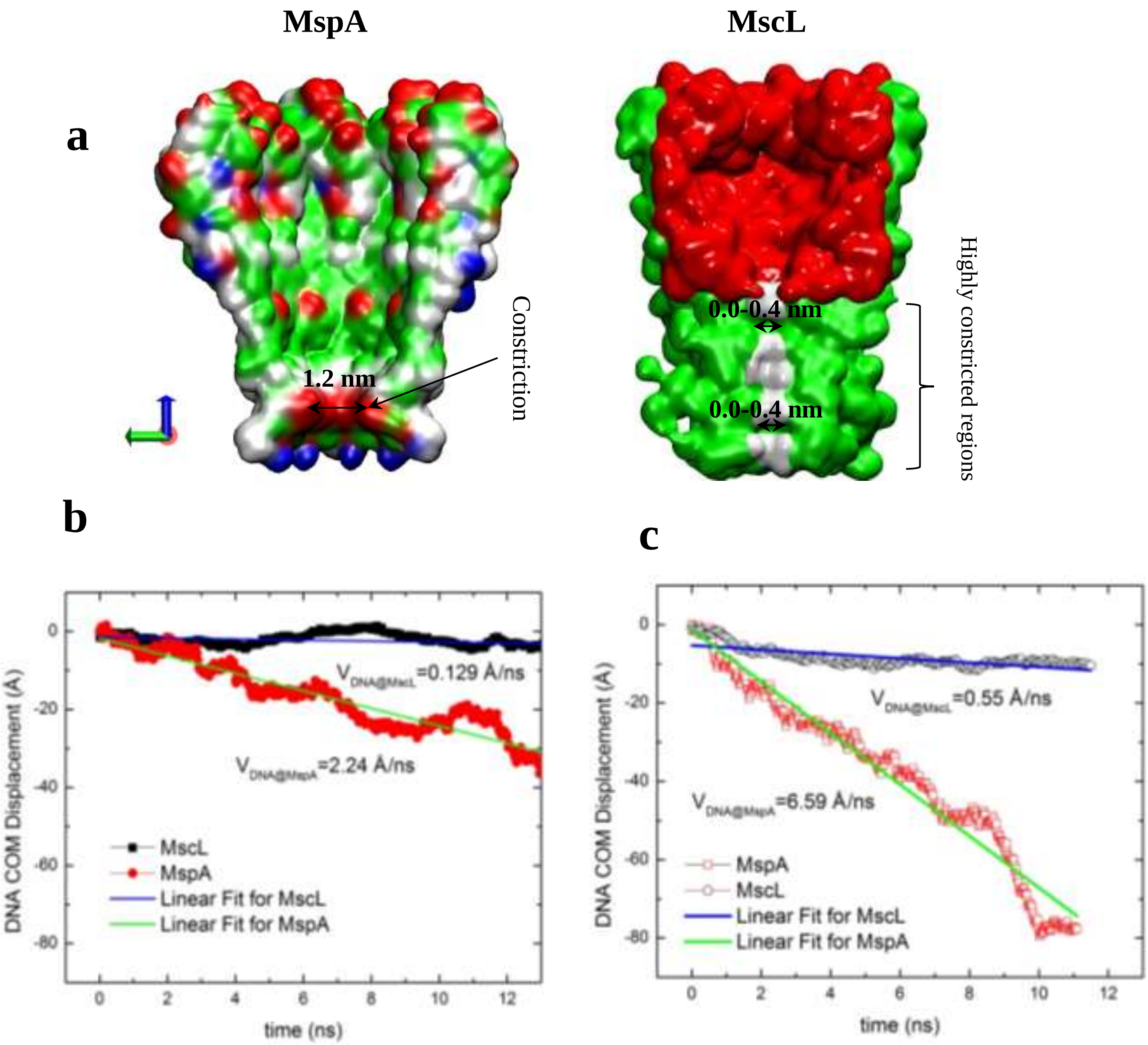

Figure 6.4 a) Cross-Sections of MspA and MscL pores and their structural differences. **b)** DNA center of mass (COM) translocation history through MspA and MscL for a bias=500 mV. **c)** DNA center of mass (COM) translocation history through MspA and MscL for a bias=1Volt.

CHAPTER 7: Conclusion

In conclusion, we studied the transport of water molecules, ions, and DNA molecules across different nanopore membranes with application to water desalination, power generation and biosensing. Using extensive atomistic simulations, we explored the possibilities of using MoS_2 and MscL as a candidates for water desalination and DNA sequencing, respectively. In addition, the classical theories for hydrodynamic flow in circular pores were corrected to account for the microscopic physics and chemistry of carbon-based nanopores at the water-pore interface. We also investigated the structural and dynamical properties of aqueous ions in ultrathin nanopores (single-layer graphene) as compared to thick nanopores (CNTs).

In the second chapter, we showed that MoS_2 membranes are promising for water purification and salt rejection. MoS_2 nanopores strongly reject ions allowing less than 12% of the ions (depending on pore areas) to pass through the porous membranes. The water permeation rates associated with these MoS_2 porous membranes are found to be 2 to 5 orders of magnitude greater than that of currently used membrane materials. The fish-bone, hourglass architecture of the pores enhances water permeation to a large extent compared to its other counterparts. In the third chapter, we corrected the HP model by studying the variation of hydrodynamical properties (friction coefficient, viscosity and slip length) with the thickness and diameter. Significant variations are observed as the thickness approaches the infinitesimal thickness of the single-layer graphene nanopore. Flow in long CNTs is enhanced by the smooth and frictionless nature of the tube surface where a high slippage occurs. As the thickness reduces, flow rates are dominated by high interfacial friction and viscosity at the pore end regions. Permeation coefficients from the corrected Hagen-Poiseuille model, based on the friction and viscosity relations, successfully predict the values from experiments and molecular dynamics simulations. In the fourth chapter, we showed that the pore slippage, which is not accounted for in the original Sampson's theory, plays an important role. The original Sampson theory is revisited and corrected for the slippage and the variation of viscosity at the membrane interface.

We introduced a new set of formulas for the slip and viscosity-corrected Sampson's theory which results in good agreement with data from MD and NS simulations as well as experiments. The ratio of slip length to radius of the pore is the key parameter in explaining the flow in ultrathin nanopores.

In the fifth chapter, the structural and dynamical properties of aqueous ions in ultrathin nanopores were shown to differ from the predicted properties by the classical theories. Formation of the ionic structures at the nanopore interfaces begins to have an unstable and dynamic behavior as the thickness of nanopore reduces to that of a single-layer graphene nanopore. Unlike the EDL in thick CNTs where diffuse and Stern layers similar to that of the Gouy-Chapman-Stern model are observed, in the ultrathin nanopores, no Stern layer is present and a weak (lower than the bulk ion concentration) diffuse layer is only present for highly charged nanopores. The critical ratio of surface area to solution volume is reached only for single-layer graphene nanopores for which ultra-fast residence times of counter-ions is observed.

In the sixth chapter, we showed that a mechanical tension can be used for DNA detection through a mechano-sensitive channel of large conductance, MscL. Four distinct force signals were detected for bases with forces decreasing in the order T> G> C>A. An initially-closed MscL opens to ssDNA due to electric-field mediated translocation and the pore geometry adapts to the size of each base. Ionic current signal is also distinct for each base, making MscL pore amenable for detecting bases with two parallel signals, namely, membrane tension and ionic current. We found a completely different gating mechanism of MscL during ssDNA translocation compared to its normal operation. The translocation speed of DNA in MscL is roughly one order of magnitude slower compared to that in MspA.

Appendix A: Supplementary Information for Chapter 2

A.1 Figures

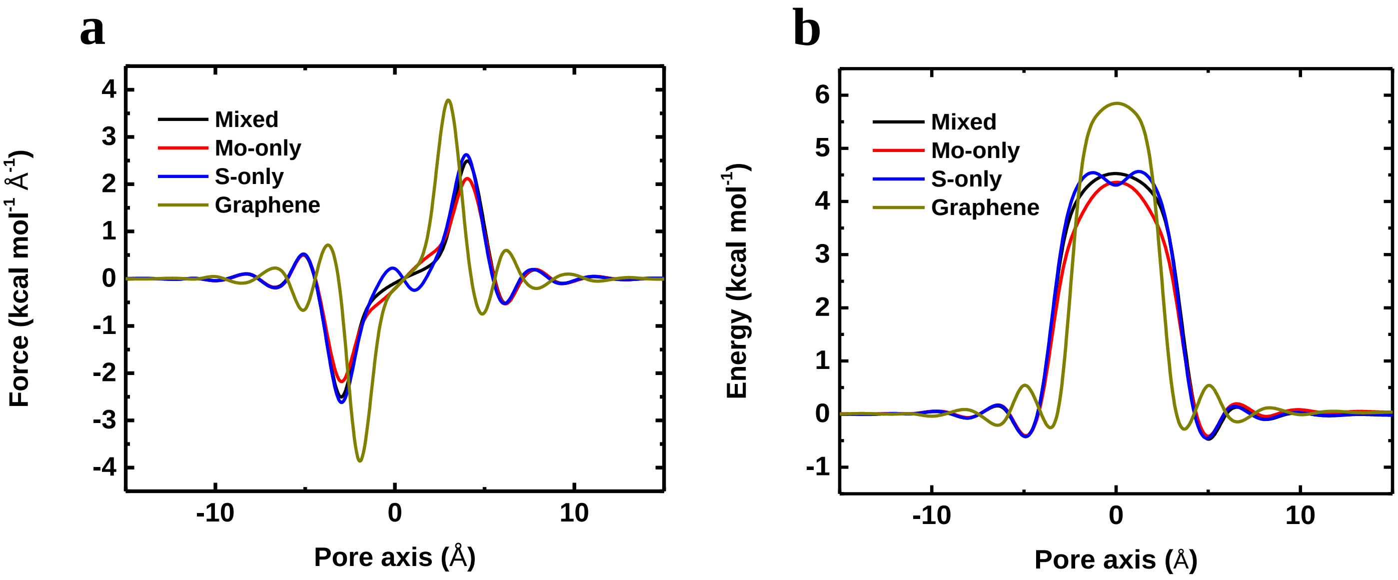

Figure A.1 Energy Barriers. (**a**) Average force on a water molecule computed along the pore axis for the Mixed, Mo-only, S-only and graphene membranes with similar pore areas. (**b**) Potential of mean force computed along the pore axis for the Mixed, Mo-only, S-only and graphene membranes with similar pore areas. To calculate the energy barrier experienced by a water molecule when moving across a pore, the simulation box is first divided into bins of equal length along the axis of the pore (z). Next, in each bin, the force on each water molecule is averaged over both the simulation time and all the water molecules of the bin when the system is in equilibrium (no external pressure). Using the resulting average force (F) along the pore axis (z) (Figure A.1a), the energy required to move a water molecule from a reference point (z_o) in the bulk water to any other point (z) can be obtained by $\int_{z_0}^{z} F(z)dz$.

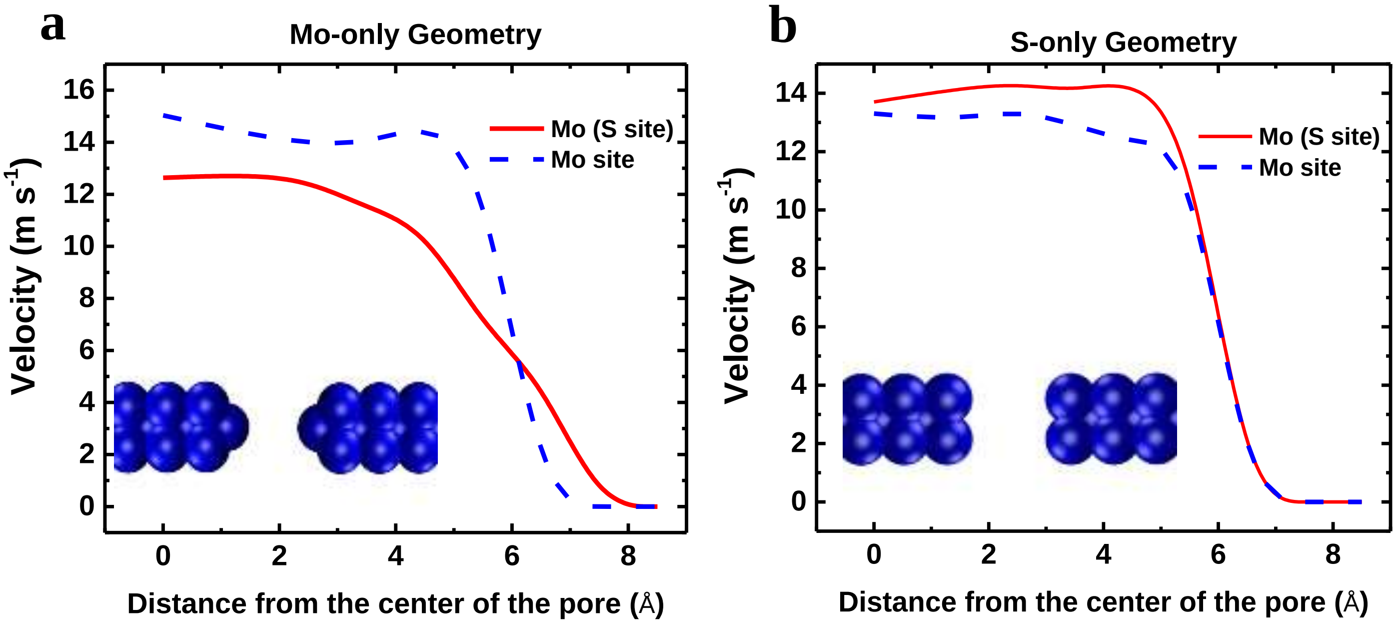

Figure A.2 Velocities. Axial velocity profile of water molecules in the radial direction at the location of S and Mo atom layers where S atoms are replaced by Mo atoms (all Mo atoms). (**a**) For the Mo-only nanopore of Figure 2.4a. (**b**) For the S-only nanopore of Figure 2.4b. As discussed, the higher flux observed in the Mo-only pores is a result of the nozzle-like structure of the pore compared to the S-only pores. To further confirm the importance of the pore geometry in achieving the higher water velocities, the role of the atom type (Mo or S) is excluded by replacing all S atoms by Mo atoms (leading to a fictitious three-layer molybdenum membrane). The axial velocities of water in the radial direction at the location of each atom layer (the middle layer of Mo, and outer layers of Mo (S layers in real MoS_2)) are plotted in Figure A.2a and Figure A.2b for both Mo-only and S-only pore structures, respectively. Comparing these velocity profiles with those of the real MoS_2, in Figure 2.4, we notice that the general shape of the velocity profiles are identical meaning that the water flux is enhanced due to the nozzle-like geometry (hourglass shape) of the Mo-only pore and remains almost independent of the atom types.

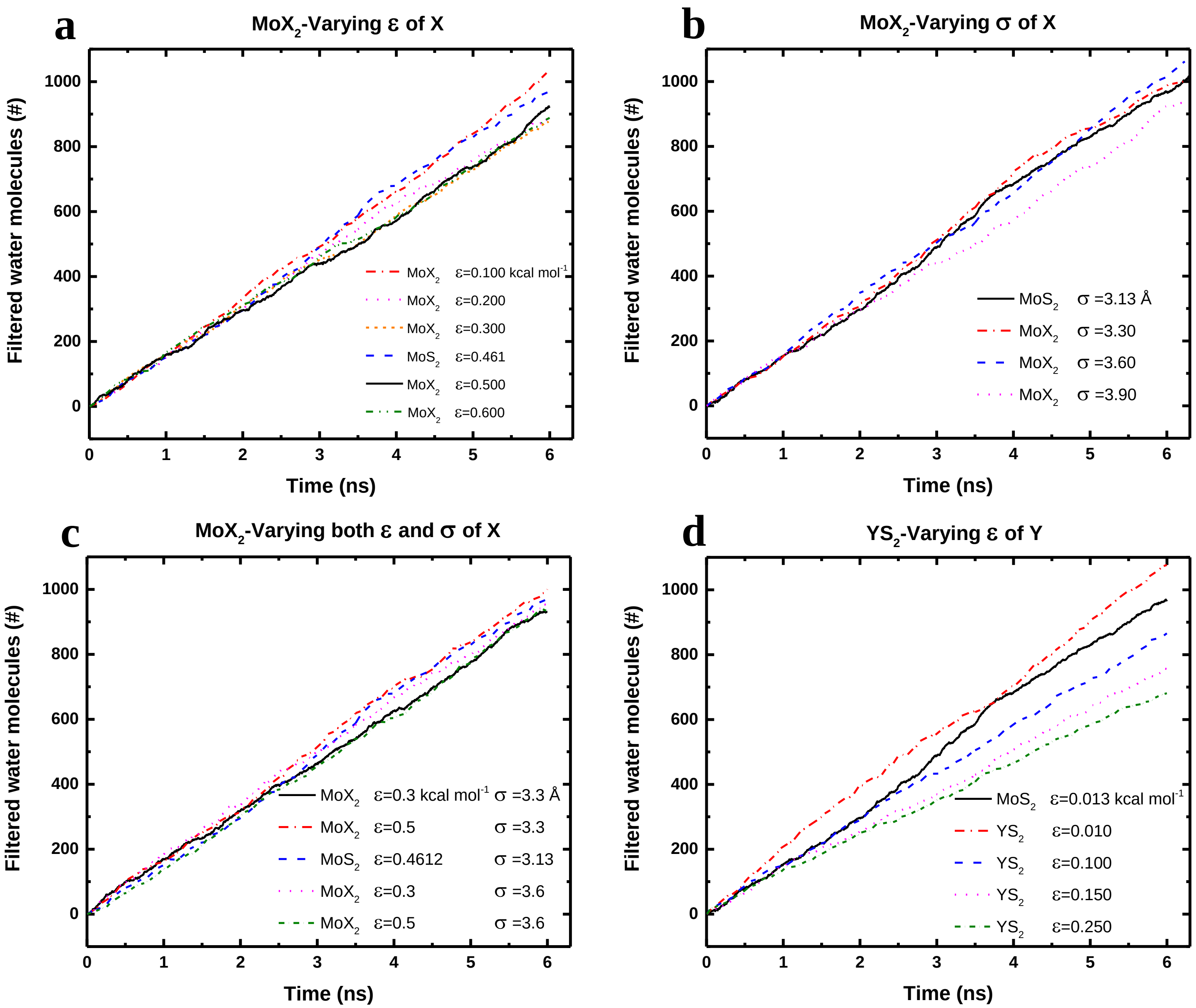

Figure A.3 Other Transition Metal Dichalcogenide Membranes. Water permeation across a Mo-only geometry pore at 250 MPa for (**a**) MoX_2 by varying ε of X (**b**) MoX_2 by varying σ of X **c|** MoX_2 by varying both ε and σ of X (**d**) YS_2 by varying ε of Y. The molecular dynamics forcefield parameters are not available for the other transition metal dichalcogenide materials (TMD). Therefore, we swept over the Lennard-Jones parameters (σ, ε) of MoS_2 to investigate the potential performance of other TMD materials. Two different types of materials (MoX_2 and YS_2) were considered. For the MoX_2, only the parameters of the chalcogen atom (X) were varied to resemble the possible properties of membranes like $MoSe_2$ and $MoTe_2$. The Mo-only pore geometry was used and a pressure of 250 MPa was applied. As shown in part a, b and c, the water permeation rate does not change significantly with varying σ and ε of X. Since atomic size of sulfur is smaller than those of the other chalcogen atoms (Se, Te, etc.), only higher values of σ were considered. For the other type, YS_2, the ε of the transition metal (Y) atom was varied to study the efficiency of YS_2 membranes. We did not change σ, since the pore area changes for Mo-only pore geometry. As shown in

Figure A.3 (cont.) Figure A.3d, changing the parameter of Y effects the permeation rate of water which decreases with increasing ε. The ion rejection percentages of MoX_2 and YS_2 do not change significantly and lie within 3% of ion rejection of MoS_2 (92%). Based on the analysis, we conclude that the transition metal atom plays a more important role than the chalcogen atom when it comes to choosing the best TMD material for desalination.

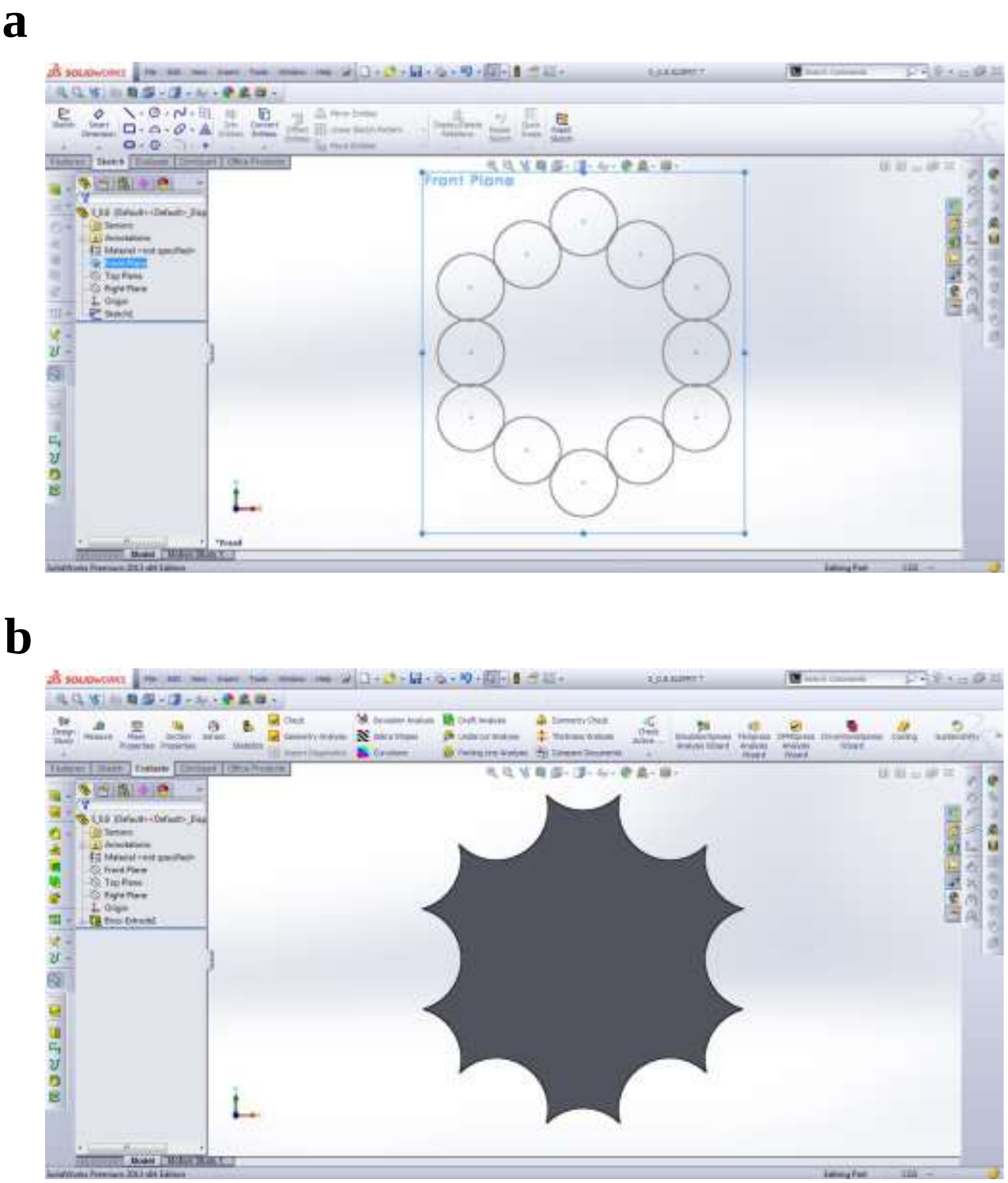

Figure A.4 Calculation of pore area. (**a**) Terminating atoms of a pore represented by their size. (**b**) Extruded area of the pore. The pore area, which is accessible to water molecules, is computed by considering the size of the atoms on the edge of each pore. First, the coordinates of all terminating atoms' centers as well as the van der Waals radii of sulfur and molybdenum are input into the SolidWorks program. Then the accessible area is extruded through the atoms and the pore area is calculated.

A.2 Table

Table A.1 The Lennard-Jones parameters employed in the simulations are tabulated below.

Interaction	σ [Å]	ϵ [kcal mol^{-1}]
C-C[95]	3.3900	0.0692
Mo-Mo[171]	4.2000	0.0135
S-S[171]	3.1300	0.4612
O-O[95]	3.1656	0.1554
H-H[95]	0.0000	0.0000
Na-Na[137]	2.1600	0.3526
Cl-Cl[137]	4.8305	0.0128
C-O[68]	3.4360	0.0850
C-H[68]	2.6900	0.0383
Rest	Obtained by Lorentz-Berthelot rules.	

Appendix B: Supplementary Information for Chapter 3

B.1 Green-Kubo Auto Correlation Functions

The cumulative integrals of the auto correlation functions for viscosity and friction coefficient for the (10,10) CNTs with different thicknesses as well as the monolayer graphene nanopore of similar diameter are shown in Figure B.1.

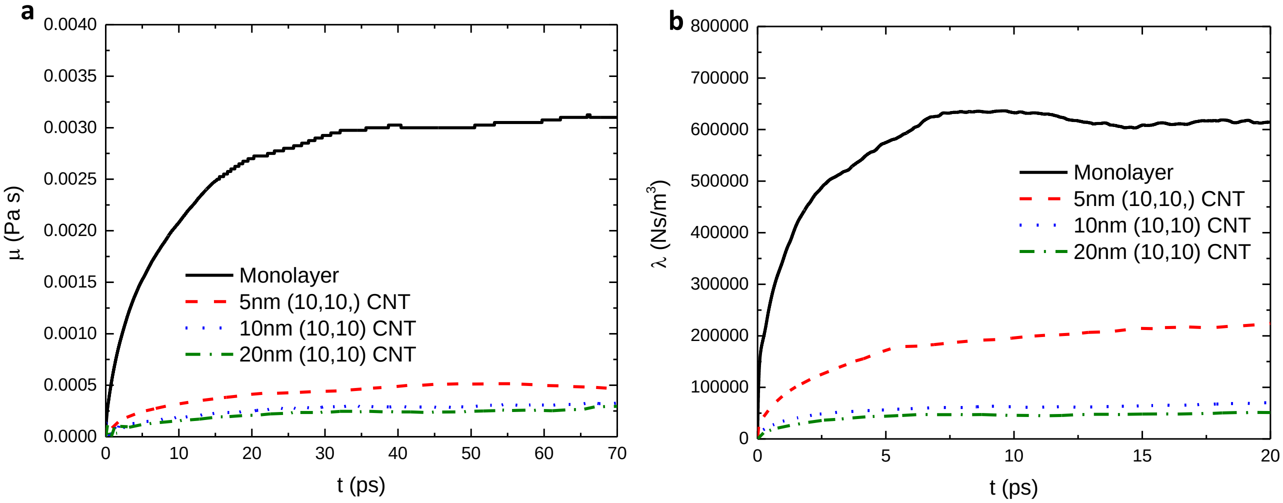

Figure B.1 Cumulative integral of the Green-Kubo (GK) auto correlation functions for **a)** viscosity $\mu_{ab} = \frac{V}{K_B T}\int_0^\infty \langle P_{ab}\,(0) \cdot P_{ab}(t)\rangle\, dt$ and **b)** friction coefficient $\lambda = \frac{1}{K_B T\,A}\int_0^\infty \langle F(0) \cdot F(t)\rangle\, dt$ as a function of time for the (10,10) CNTs and monolayer graphene with a similar pore diameter. Viscosity and friction coefficients are obtained by fitting a constant line to the plateaus between time t=40ps and t=70ps, and between t=10ps and t=20ps, respectively.

B.2 Variation of Viscosity and Friction with Thickness and Radius

The weighted average relations are used to estimate viscosity and friction for different thicknesses. As shown in Figure B.2, the variation of both viscosity and friction with thickness is well captured by the model.

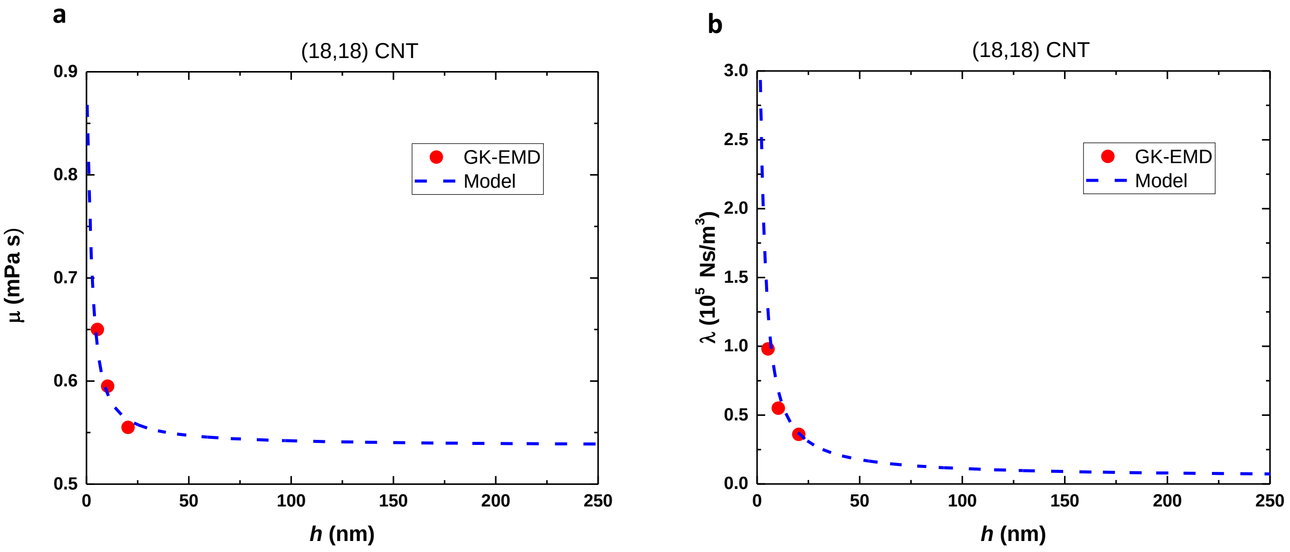

Figure B.2 Thickness variation of **a)** viscosity and **b)** friction coefficient predicted by the weighted average model (dashed blue line). The GK-EMD values (red symbols) are well described by the model. As thickness increases, the values converge to that of infinitely long CNTs.

Variation of viscosity with diameter can be obtained from weighted average of viscosity in the interface, μ_{i}, (with a layer of d_{i}) and in the bulk region of the CNT. d_i=0.38 nm was used previously by Suk *et al*.[94] to describe the thickness of the interfacial viscosity. As shown in Figure B.3, most of the variation takes place within ~0.4 nm of the surface which is consistent with d_i=0.38 nm. Using μ_i^e=9.5 × 10^{-4} Pa s and μ_i^{∞}=3.2 × 10^{-4} Pa s through fitting (it should be noted that viscosity also varies along the length of CNT which results in different μ_{i} values for the end region and the middle section of the CNT), the variation of viscosity with radius is given by

$$\mu^{\infty}(r) \ = \frac{7.5 \times 10^{-5}}{r^2} - \frac{4\times 10^{-4}}{r} + \mu_{\mathrm{bulk}} \qquad \text{(Pa s)}$$

and

$$\mu^e(r) = -\frac{1.4\times10^{-5}}{r^2} + \frac{7.6\times10^{-5}}{r} + \mu_{\text{bulk}} \quad \text{(Pa s)}$$

Variation of $\lambda^\infty(r)$ and λ^e with radius can be obtained by applying the power law to the data as follows:

$$\lambda^\infty(r) = -6.3\times10^3\, r^{-0.6} + \lambda_{\text{flat}} \quad (\text{N s m}^{-3})$$

and

$$\lambda^e(r) = 5.9\times10^4\, r^{-3.5} + \lambda_{\text{slit}} \quad (\text{N s m}^{-3})$$

Note that *r*, in the equations above, is in nm. The relations given above are used for viscosity and friction to predict the values obtained from Green-Kubo calculations. As shown in Figure B.4, the variation of both viscosity and friction with diameter is well captured by the model for all the thicknesses considered.

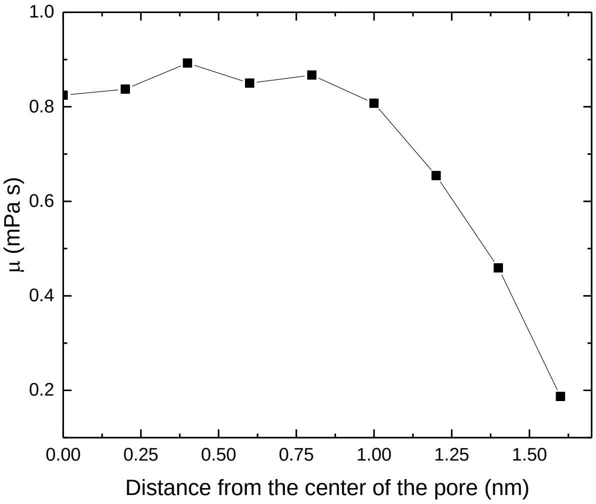

Figure B.3 Viscosity as a function of distance from the center of the pore for an infinitely long (26,26) CNT

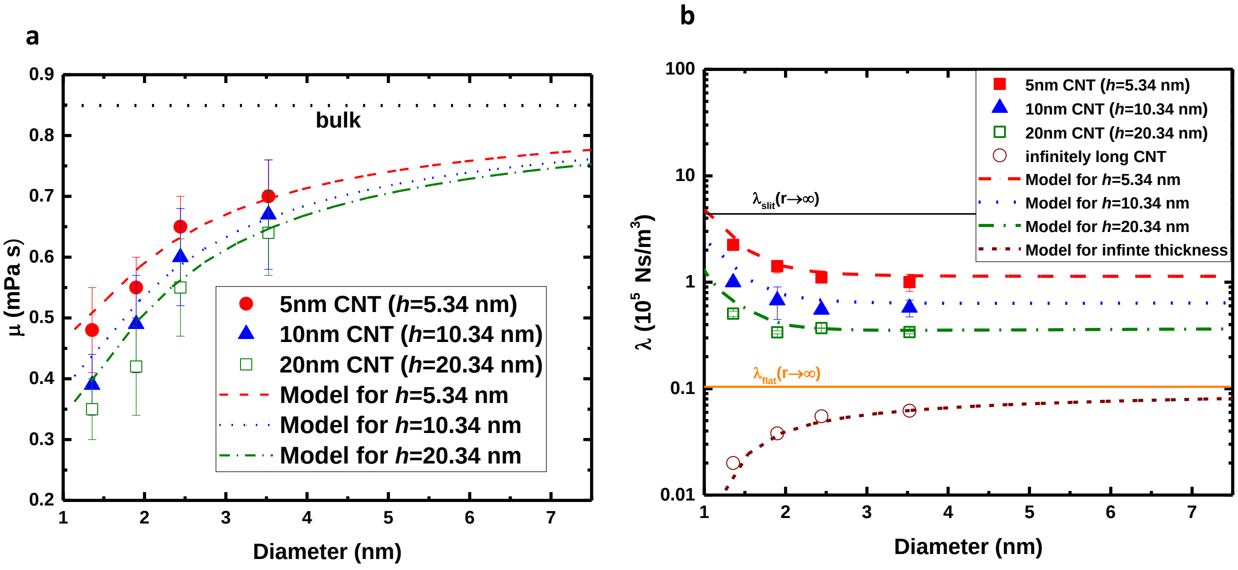

Figure B.4 a) Viscosity and **b**) friction coefficient for finite-length CNTs are plotted as a function of diameter for all the thicknesses considered. The symbols represent the data from Green-Kubo calculations and the curves are the prediction from the model which describes both viscosity and friction variation with diameter and thickness.

To provide more insight into the underlying physics, we plotted the force autocorrelation function (FACF) for different CNT diameters in Figure B.5. As shown in B.5a, the magnitude of FACF at t=0 ($\langle F(0)^2 \rangle$, which is the variance of the force between CNT and water molecules), is the smallest for the (6,6) CNT consistent with the explanation by Falk *et al*.[81] In addition, the relaxation time of FACF for the (6,6) CNT is small (featureless exponential type decay with weak memory), which leads to a smaller friction coefficient, compared to other CNTs (oscillatory type decay with strong memory). We plotted the contribution of area and integral of FACF to the friction coefficient normalized by that of (6,6) CNT in Figure B.5b. As shown, the contribution of integral of FACF is much smaller for the (6,6) CNTs due to smaller force amplitude and relaxation time.

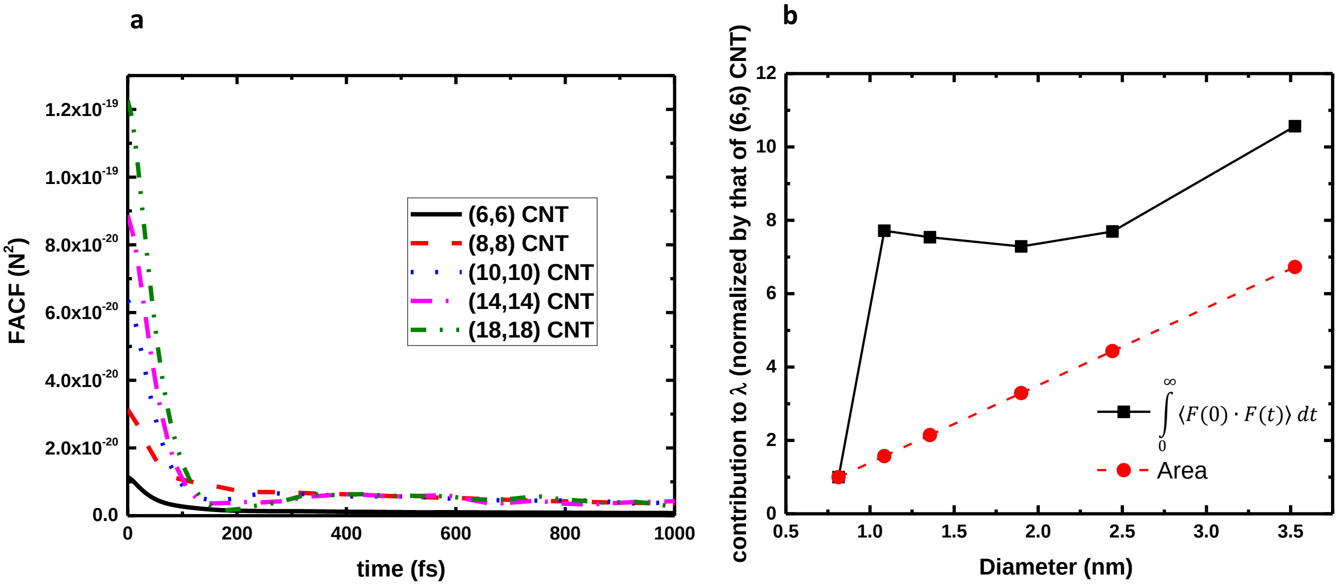

Figure B.5 a) Force autocorrelation function (FACF) of 5nm long CNTs for different diameters. **b)** The contribution of the integral of FACF and the surface area to the friction coefficient (normalized by that of (6,6) CNT) are plotted as a function of diameter for 5nm long CNTs.

The variation of viscosity and friction coefficient as a function of distance from the edge of the nanotube along the tube axis is shown in Figure B.6. Both viscosity and friction coefficient decrease with distance away from the edge. In the middle section of the nanotube, the values converge to that of an infinitely long CNT. Most of the variation takes place within 0.7 nm from the edge of the nanotube.

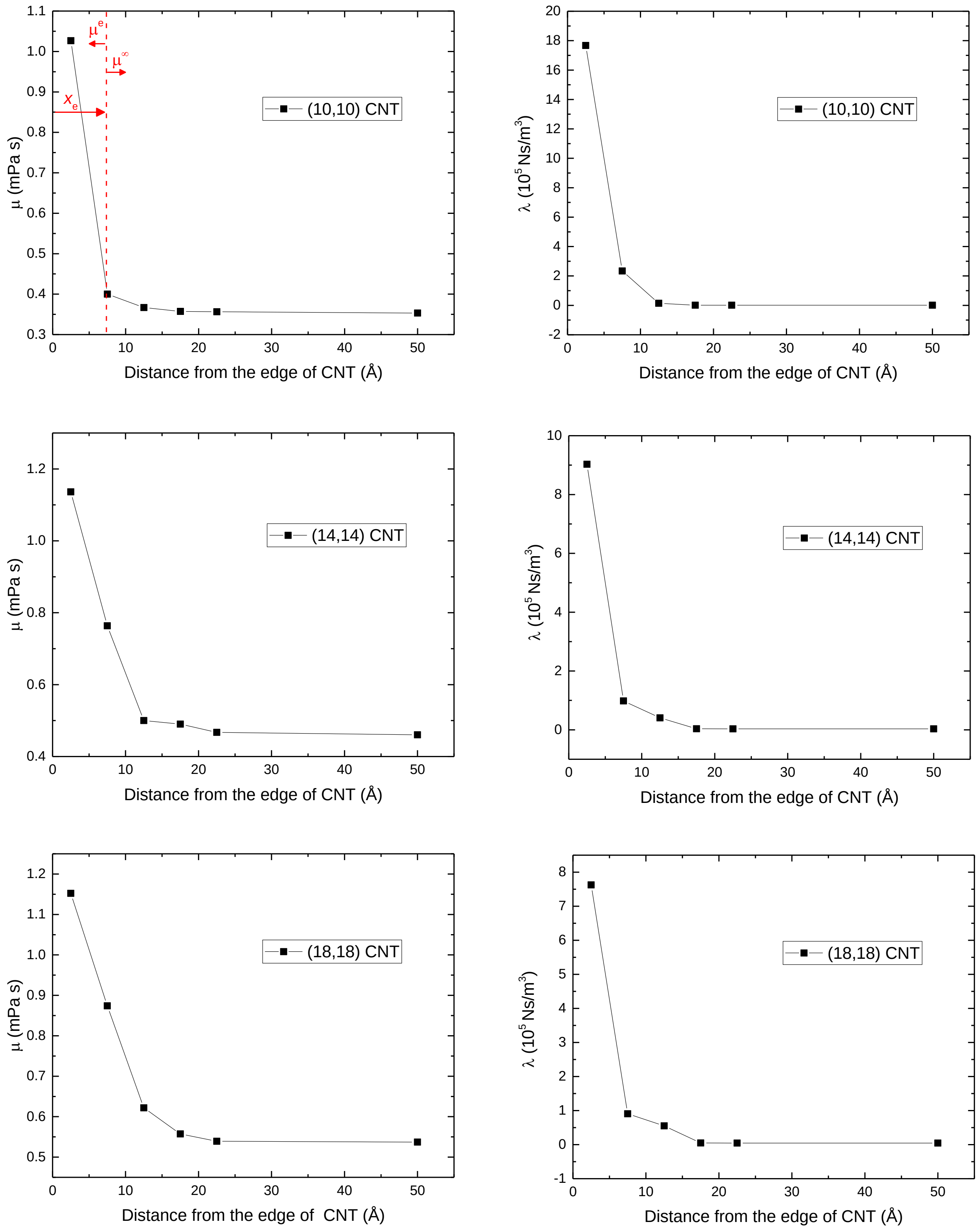

Figure B.6 Viscosity (left plots) and friction coefficient (right plots) as a function of distance from the edge of the nanotube for (10,10), (14,14) and (18,18) CNTs. All the CNTs are 10-nm long and the viscosity and

Figure B.6 (cont.) friction coefficient are shown for one half length of the CNT. Both viscosity and friction coefficient decrease with distance away from the nanopore edge. In the middle section of the nanotube, the values converge to that of an infinitely long CNT. The end region (with μ^e and a length of x_e) and middle section of the CNT (with μ^∞) are separated by the red dashed line for (10,10) CNT.

B.3 Variation of Water Density along the Length of CNTs

Water density as a function of distance from the nanotube edge inside a (10,10) CNT is shown in Figure B.7. The density variation is significant in the end region (inside the nanotube) compared to the middle section of the nanotube. The higher density variation at the ends results in a higher viscosity.

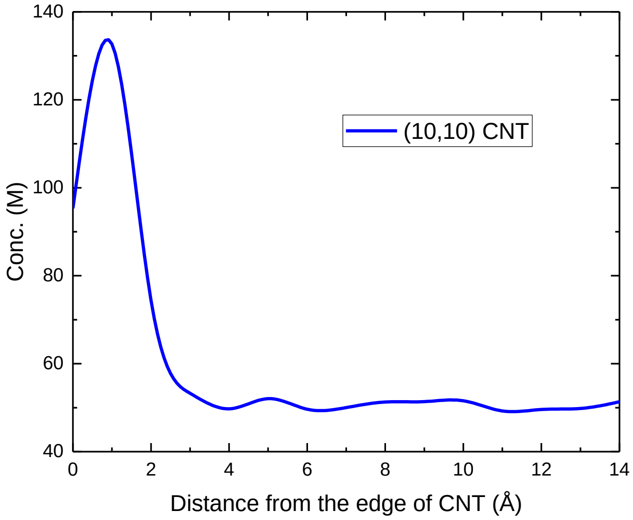

Figure B.7. Water density as a function of distance from the edge of (10,10) CNT. Higher density variation is observed inside the CNT at the end region.

B.4 Dagan and HP Theories with Empirically Corrected Pressure Drop Length

Dagan's equation is simply the HP equation with no slip condition and the hydrodynamic pressure drop length is corrected by accounting for the entrance/exit hydrodynamic resistance given by Sampson's equation. The hydrodynamic pressure drop length (h_l) in a monolayer graphene pore is shown to be a linear function of pore radius[87] and is given by the empirical relationship, $h_l^{\mathrm{GRA}} = 0.27r + 0.95$ nm using MD simulations. In finite-length CNTs, h_l can be taken to be the addition of the center-to-center thickness and the monolayer graphene hydrodynamic pressure drop length. The general relation is then given by $h_l = (0.27r + 0.95) + (h - \sigma_{c-c})$ nm. In Figure B.8, Dagan and HP theories with no slip condition result in identical permeation coefficients when the empirical relationship is used for the thickness (h_l) in HP with no slip condition.

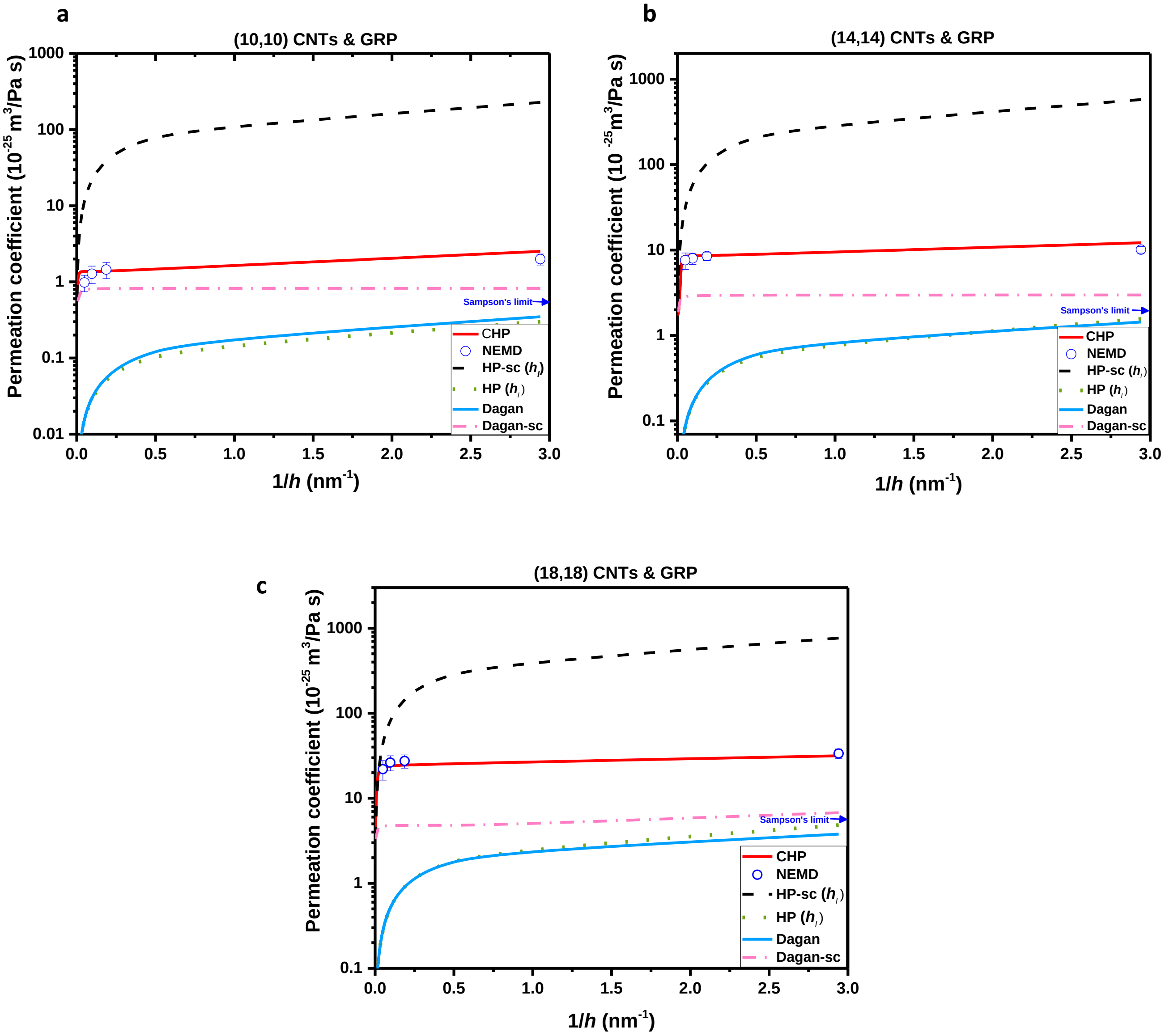

Figure B.8. Figure 3.4 is replotted where the thickness is taken to be the Suk's empirical relationship[87] ($h_l = (0.27r + 0.95) + (h - \sigma_{c-c})$ nm) for HP and HP-sc. The permeation coefficients from Dagan's theory almost collapse with those from HP theory with empirically corrected hydrodynamic pressure drop length.

B.5 Contribution of the Correction of Viscosity, Friction and Hydrodynamic Pressure Drop Length to the CHP Model

Accounting for the proper variation of viscosity, friction (or slip length) and hydrodynamic pressure drop length with length and diameter is necessary for a complete model to predict the NEMD permeation coefficients. In Figure B.9, the individual contribution of the correction of viscosity, friction and hydrodynamic pressure drop length is investigated by excluding their variation with length and diameter. Friction coefficient is the most considerable quantity affecting the permeation coefficient followed by the hydrodynamic pressure drop length. Viscosity, however, is only important for small diameter pores as it approaches bulk value for larger-diameter pores.

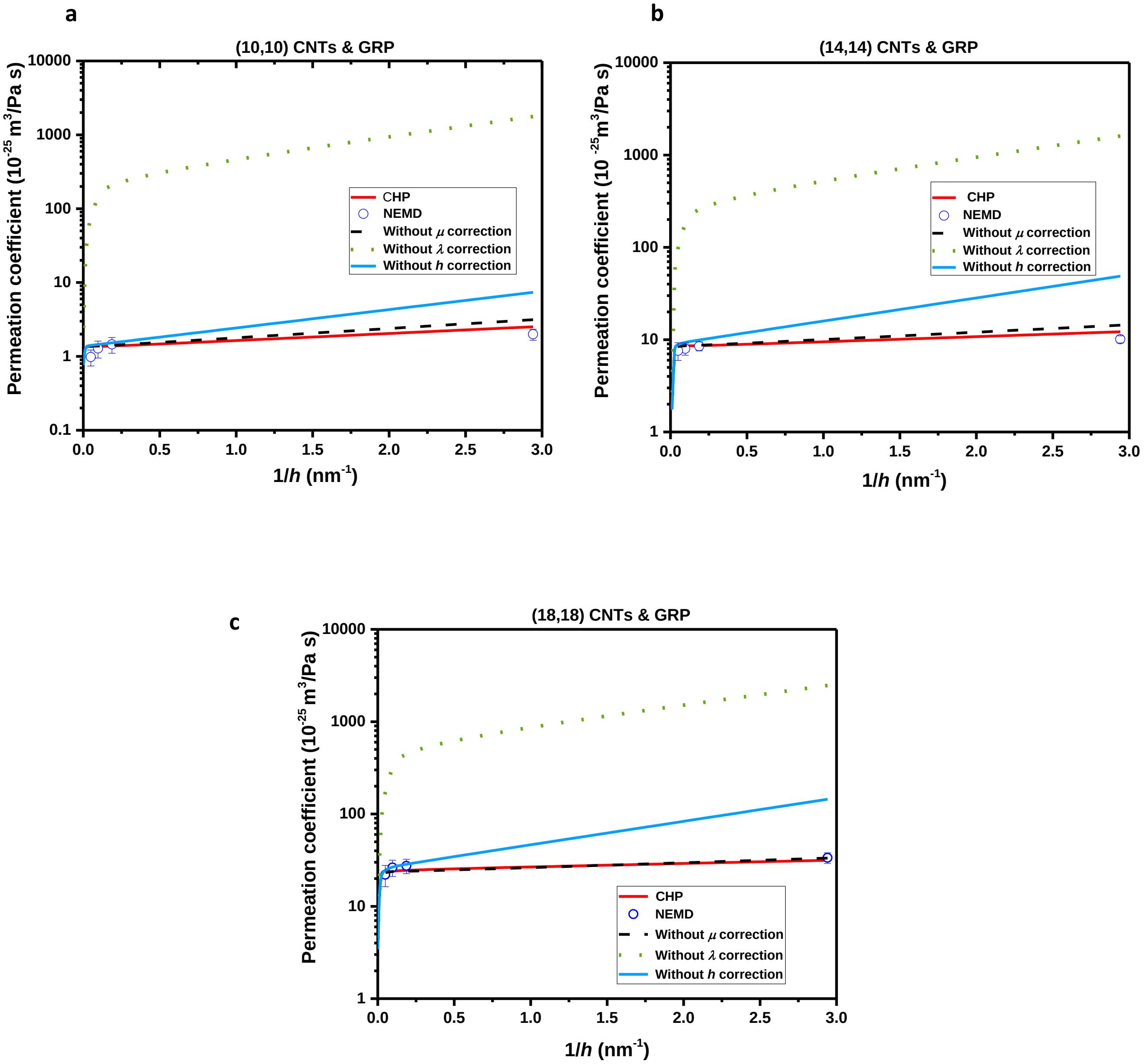

Figure B.9. Figure 3.4 is replotted with the individual contribution of the correction of viscosity, friction and hydrodynamic pressure drop length. Dashed black curve shows the CHP without viscosity correction, the dotted green curve represents the CHP without friction correction and the solid blue curve shows the CHP without correction to the hydrodynamic pressure drop length. Viscosity correction is important only for small diameter pores as it approaches the bulk value for larger-diameter pores.

Appendix C: Supplementary Information for Chapter 4

C.1 MD Simulation Methods

MD simulations were performed using the LAMMPS package[72]. A typical simulation box consists of water molecules and a graphene sheet (see Figure C.1). A nanopore is drilled in graphene sheet with carbon center-to-center diameter of 0.83 nm, 1.10 nm, 1.36 nm, 1.90 nm, 2.44 nm, 3.53 nm and 7.42 nm. The Cartesian coordinate (*1*,*2*,*3*) is defined such that the *1-2* plane lies in the plane of graphene and the *3*-axis lies on the z-axis in the cylindrical coordinates. The graphene sheet lies in the *1-2* plane and the *3*-axis is along the axis of the pore (in the Cartesian coordinates). The system dimensions vary from 3.75 nm to 16.3 nm along *1* and *2* axes, and 6 nm to 12 nm along the *3*-axis depending on the diameter. The dimensions along the *1* and *2* axes change with the radius of the pore to account for the porosity of the nanopore (the ratio of pore area to membrane area is <0.148). The simulations contain up to ~320,000 atoms. The SPC/E water model was used and the SHAKE algorithm was employed to maintain the rigidity of the water molecule. The carbon-water interactions were modeled by the force-field parameters given in Wu *et al*.[68]. The carbon-water Lennard-Jones (LJ) parameters were varied to generate different slip lengths. A summary of the MD simulations performed is provided in Table S1. Since the carbon atoms are fixed in space, the interactions between carbon atoms were turned off. The LJ cutoff distance was 1.2 nm. The long range electrostatic interactions were calculated by the Particle-Particle-Particle-Mesh (PPPM) method[172]. Periodic boundary conditions were applied in all the three directions. For each simulation, first the energy of the system was minimized for 10000 steps. Next, the system was equilibrated using NPT ensemble for 1 ns at a pressure of 1 atm (both at the start and the end of the simulations with a damping time of 100fs) and a temperature of 300 K with a time-step of 1fs. With the graphene atoms held fixed in space, the NPT simulations (the three dimensions are controlled independently using the components of the stress tensor) allow the water to reach its equilibrium density (1 g/cm^3). Then, an additional NVT simulation was performed for 2 ns to further equilibrate the system. Temperature was maintained at 300 K by using the Nosè-Hoover thermostat[75,76] with a time constant of 0.1 ps. Finally, the non-equilibrium pressure-driven simulations were carried out in NVT ensemble for 10 ns to calculate the volumetric flow rates and subsequently obtain the hydrodynamic resistance for the applied pressures. The external pressures were applied using the method used in ref[59,115]. External forces are applied on individual oxygen atoms of water within 1 nm of the end of the simulation box. The applied pressure drop is then obtained from $\Delta P = \frac{fN}{A}$ where f is the individual force on the oxygen atom, N is the number of oxygen atoms within the 1 nm slab region and A is the area of the cross section (or the graphene membrane). Different pressure drops of 10MPa, 50MPa and 100MPa are applied and normalized by their corresponding volumetric flow rates to get the average hydrodynamic resistance (presented as the data points in Figure 4.3). Slip lengths (as shown in Figure 4.1a) are computed from MD simulations[115] using $\delta = \frac{\mu U_{\mathrm{slip}}}{\tau_{\mathrm{int}\,erface}}$, where U_{slip} is the slip velocity (which is directly obtained from the velocity profiles), and $\tau_{\mathrm{int}\,erface}$ is the friction force (parallel to the axis of the pore) per unit pore area. The friction force is calculated between the water molecules and the wall atoms.

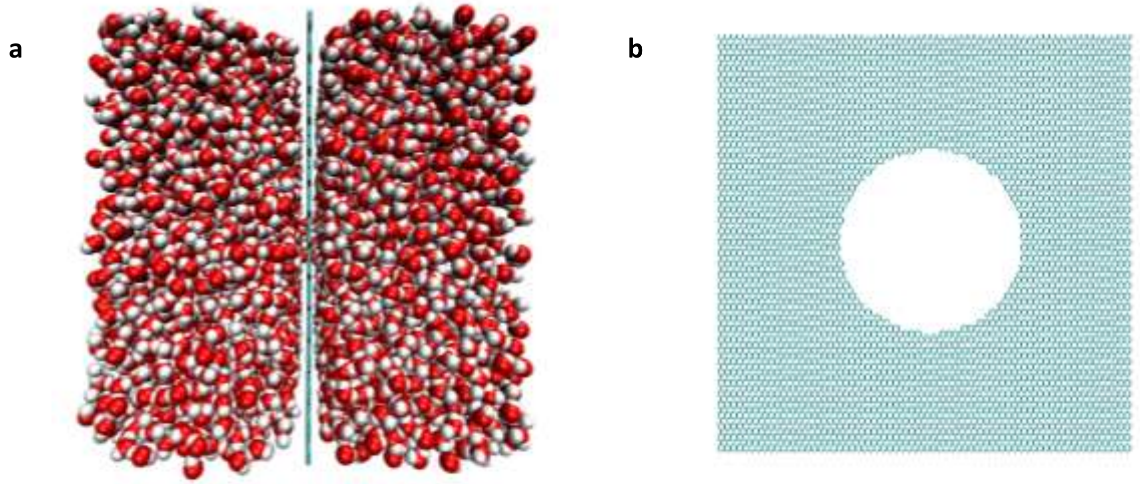

Figure C.1 a) Simulation box for water across a single-layer graphene nanopore. **b)** Membrane view of a nanopore with a diameter of 3.54 nm. Oxygen, hydrogen and carbon atoms are shown in red, white and cyan, respectively.

Table C.1 Summary of the MD simulations performed in this work. LJ parameter $\varepsilon_{\text{C-O}}$ (between carbon atom of graphene and oxygen atom of water) is varied for some of the simulations to generate different slip lengths. In the force-field by Wu *et al.*[68], $\varepsilon_{\text{C-O}}$ is 0.085 kcal/mol.

# of simulations	# of C atoms in each simulation	*x*, *y* and *z* dimensions of simulation box (nm)	a (nm)	$\varepsilon_{\text{C-O}}$ (kcal/mol)
2	8,563	3.75, 3.75 and 6	0.24	0.00001 and 0.0850
2	8,553	3.75, 3.75 and 6	0.37	0.00001 and 0.0850
2	8,541	3.75, 3.75 and 6	0.51	0.00001 and 0.0850
1	30,508	5, 5 and 12	0.78	0.0850
1	30,447	5, 5 and 12	1.05	0.0850
1	64,802	7.3, 7.3 and 12	1.56	0.0850
11	323,577	16.3, 16.3 and 12	3.54	0.001, 0.0850, 0.1, 0.2, 0.3, 0.4, 0.5, 0.6, 0.7, 0.8 and 0.9

C.2 Fictitious Hydrophilic Material with a No-Slip Condition

The interaction parameter between the oxygen atoms of water and carbon atoms of graphene ($\varepsilon_{\text{C-O}}$, LJ parameter) is increased from the value ($\varepsilon_{\text{C-O}}$=0.085 kcal/mol) given in the developed force-field by Wu *et al*.[68] until the graphene surface becomes highly hydrophobic and results in a no-slip condition as shown in Figure 4.1b. The varied $\varepsilon_{\text{C-O}}$ values for the 3.54 nm-radius pore (this is a large enough pore where the viscosity in the pore converges that of the bulk water) are provided in Table S1. The velocity profiles for an applied pressure of 50MPa are shown in Figure C.2. Note that increasing the interaction energy further leads to negative slip lengths which are avoided in this study. In Figure C2c, the density profile of water molecules as a function of the radial distance from the center of the pore are shown. The density profiles are very similar except for their peak (which increases with $\varepsilon_{\text{C-O}}$) for the different varied values of $\varepsilon_{\text{C-O}}$.

The volume bins in the simulations are circular shells inside the pore with a thickness of 0.34 nm (the thickness of the graphene membrane) in the 3-aixs (the axis of the pore), and a thickness of 0.2 nm in the radial direction. The velocity and density profiles are used to calculate the mass flow rates. Volumetric flow rates, Q, are then obtained by normalizing the mas flow rates by the bulk water density. Using the volumetric flow rates and the applied pressures, the hydrodynamic resistance values are obtained ($R = \frac{\Delta P}{Q}$). The hydrodynamic resistance is calculated to be $5.78 \pm 0.03 \times 10^{22}$ Pa s/m^3 and $4.21 \pm 0.04 \times 10^{22}$ Pa s/m^3, for the hydrophilic pore (with the no slippage) and real graphene pore, respectively (the errors are computed based on three different applied pressures of 10MPa, 50MPa and 100MPa).

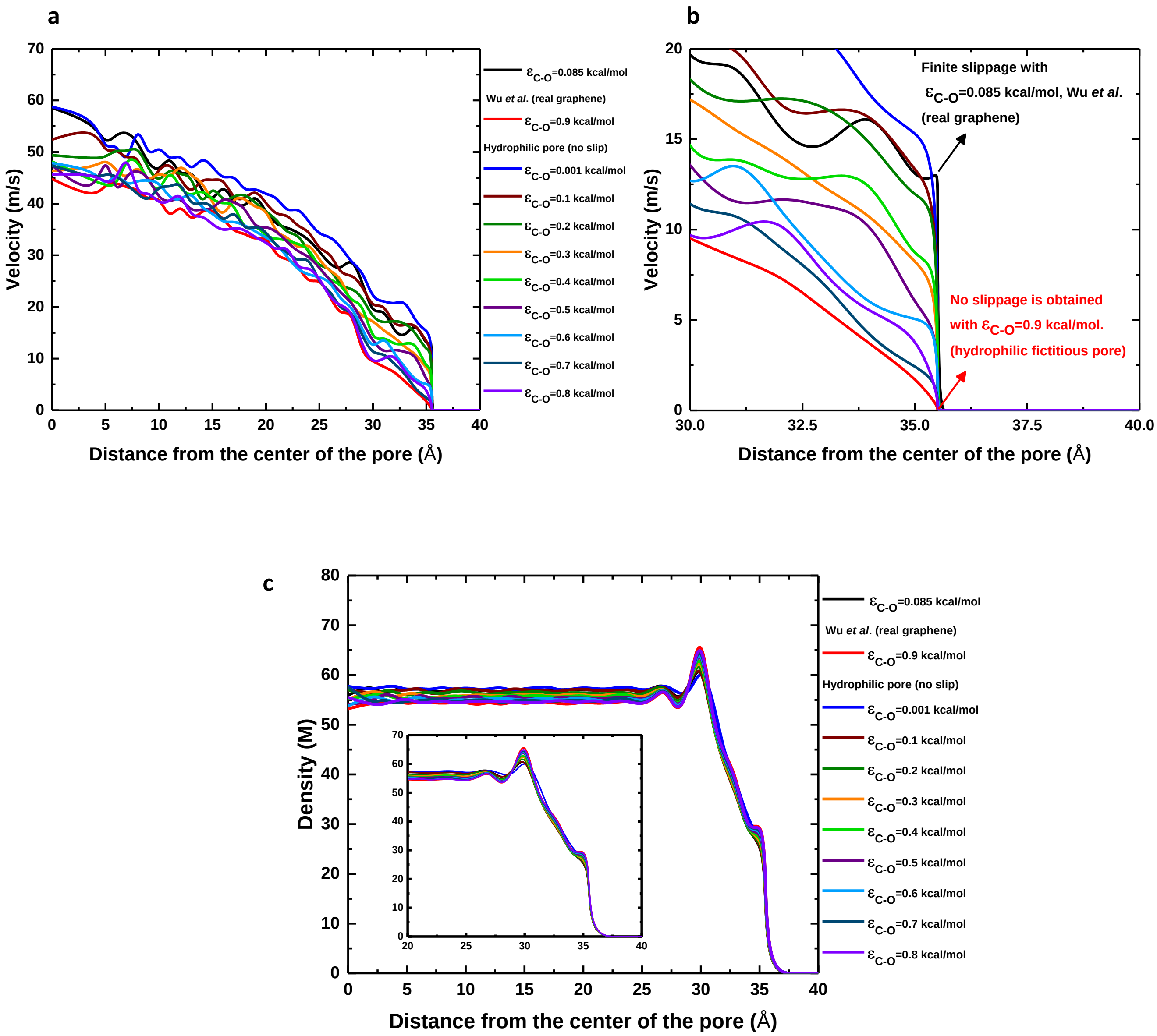

Figure C.2 a) Axial velocity profile in the single-layer graphene nanopore (a =3.54 nm) as a function of the radial distance from the center of the pore is plotted for an applied pressure 50 MPa using the Wu *et al.*[68] force-field (real graphene) and other fictitious force-fields (by varying $\varepsilon_{\text{C-O}}$) until a no-slip condition achieved ($\varepsilon_{\text{C-O}}$ =0.9 kcal/mol) **b)** A zoomed-in part of velocity profile in (**a**) is presented to clearly show the slippage (in the form of slip velocity) for the real graphene and fictitious hydrophilic pores . **c)** Density profile in the single-layer graphene nanopore (for the same systems in (**a**) and (**b**)) as a function of the radial distance from the center of the pore is plotted using different force-fields (for the same systems in (**a**) and (**b**)).

C.3 Continuum Simulations Methods

We performed continuum simulations by numerically solving the steady state Navier-Stokes (NS) continuity and momentum equations ($\nabla \cdot \mathbf{u} = 0$ and $\mathbf{u} \cdot \nabla \mathbf{u} = -\frac{\nabla p}{\rho} + \nu \nabla^2 \mathbf{u}$). **u** is the velocity of the fluid, p is the pressure, ρ and ν are the density and the kinematic viscosity of the fluid. We solved the NS equations using OpenFOAM v4.1 (http://www.openfoam.com/) based on the finite volume method. The values of ρ and ν are set to the bulk values of water (1000 kg/m^3 and 0.85×10^{-6} m^2/s, respectively). We used a 2D domain as shown in Figure C.3 with an unstructured non-uniform mesh with a high resolution around the pore and the membrane walls. The meshing is carried out using Gmsh software[173]. The mesh convergence is tested by decreasing the mesh size until the change in the maximum velocity between two successive mesh resolutions is 2%. The steady state solution is reached when the residual error between two successive solutions for velocity and pressure is less than 10^{-6}. The imposed boundary conditions are summarized in Figure C.3. The thickness of the pore is fixed to 2 nm in all simulations, except for the velocity profile in Figure C.4 in which we also used 0.34 nm. We used a higher than graphene thickness to ensure the velocity is developed inside the pore.

We further obtained the hydrodynamic resistance from the NS continuum simulations for pores with h=2 nm, $\mathrm{a} = 1 - 5$ nm, and $\Delta \mathrm{P_o} = 20 - 100$ MPa (see Table S2 for NS simulation details). The slip length,δ, is determined by extrapolating the velocity profiles. The obtained resistance values agree well with those of the slip-corrected Sampson theory (see Figure 4.3). Note that since the NS simulations have a uniform viscosity, the appropriate comparison should be made with the slip-corrected Sampson theory (not the viscosity-corrected theory with a two-viscosity model). The deviation between the resistance values of the NS continuum and the slip-corrected Sampson theory can be related to the following sources of error: 1) continuum simulations at scales of less than 10 nm requires cell size mesh of utmost less than 0.1 nm which produces larger numerical errors in the spatial discretization 2) we assumed a perfect slip condition at the side walls of the graphene membrane for all cases for simplicity whereas it is zero in the Sampson theory and 3) the thickness of the membrane is 2 nm in the NS simulations whereas it is zero in the Sampson theory.

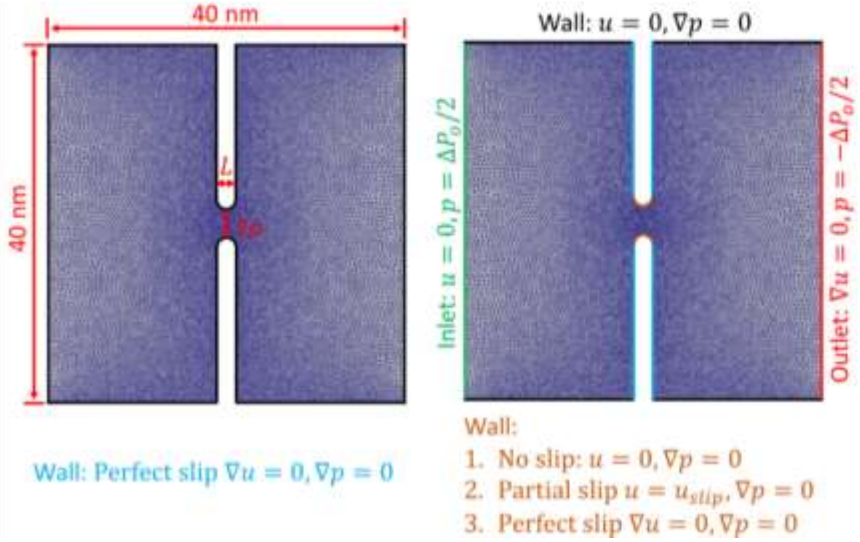

Figure C.3 The 2D computational domain, mesh, and boundary conditions which are used in the NS continuum simulations. The pressure difference, ΔP_o, and the pore radius, a, are varied in the simulations. The boundary conditions are indicated in different colors. Inside the pore, we considered three different slip conditions at the wall: no slip, partial slip and perfect slip. For the partial slip, we imposed a partial velocity, U_{slip}. The slip length, δ, is then obtained by extrapolating the velocity profile. For simplicity (avoiding singularities in the simulations), we consider a perfect slip condition at the graphene membrane walls (blue boundaries) for all cases.

Table C2. Summary of the NS continuum simulations for a pore with thickness of 2 nm to obtain the hydrodynamic resistance. Radii, slip lengths, pressure drops, volumetric flow rates and normalized hydrodynamic resistance are tabulated

a (nm)	δ(nm)	ΔP_o (MPa)	Q $(10^{-15}\ \mathrm{m}^3/\mathrm{s})$	$R/R^{Samspon}$
1	0.21	50	1.23	0.707
1.1	0.001	70	1.16	1.050
1.15	0.01	70	1.84	0.948
1.25	0.32	50	2.01	0.433
1.25	0.25	100	2.45	0.498
1.5	1.13	50	5.02	0.173
1.5	0.90	50	4.36	0.199
1.5	0.69	50	3.70	0.690
1.5	0.50	50	3.05	0.286
2	0.28	50	1.14	0.765
2	0.20	50	1.07	0.814
2	0.33	50	1.21	0.721
2	0.41	50	1.28	0.682
2	0.50	50	1.34	0.647
5	4.50	20	17.14	0.021
5	10	20	9.16	0.038

C.4 Comparison of Velocity Field from MD and NS Continuum Simulations with the Velocity Profiles Obtained from the Corrected Sampson Theory

We have drawn a schematic of the velocity profiles inside and outside the orifice based on the corrected Sampson theory in Figure C.4. Similar to the original Sampson theory, the velocity is set to zero right at the boundaries of the orifice wall inside and outside the pore. Inside the pore, the velocity is only nonzero a distance d away from the orifice boundary based on our proposed stream function in equation (4.6). Outside the pore, d corresponds to $x = b$ (in the oblate spheroidal coordinates) where the velocity is set to zero for $0 < x \leq b$ based on the proposed stream function (equation (4.6)). As shown, this treatment of the velocity field results in a smooth change in the velocity direction along a streamline. As explained in equation (4.7), (4.8) and (4.9), the velocity jump (slip velocity) at a distance d away from the orifice boundary (or when $r = a$, water assessable radius) is used to obtain its corresponding slip length as a function of d and a (equation (4.9)). As shown in Figure C.4, the treatment used in the corrected Sampson theory results in consistent velocity fields between the corrected theory and the MD-NS simulations. In graphene nanopores, the diameter is larger than its finite thickness (~0.34 nm) and therefore the flow will not be fully developed to produce a plug-like flow even in the case of perfect slip condition for the NS simulations. To show the velocity profile of different pore thickness and the velocity field of different boundary conditions (no slip, partial slip, and perfect slip), we performed simulations the steady state NS simulations. Our continuum simulations show that the velocity profile across the nanopore is not a plug-like profile at thickness of 0.34 nm using the perfect slip condition, however, as we increase the thickness to 2 nm the velocity profile flattens and approaches the plug-like profile at the same boundary condition (see Figure C.4c). The velocity field profiles for the no-slip, partial slip, and perfect slip conditions for the 2 nm thickness pore are shown in Figure C.4d-f. In both MD simulations and NS simulations (with a partial slip length), near the graphene surface (inside and outside the pore), the velocity almost vanishes similar to the velocity field in the corrected Sampson theory. The velocity jump (also shown in Fig 4.1b) inside the pore resembles the velocity jump ($r = a$, water assessable radius) modeled in the corrected Sampson.

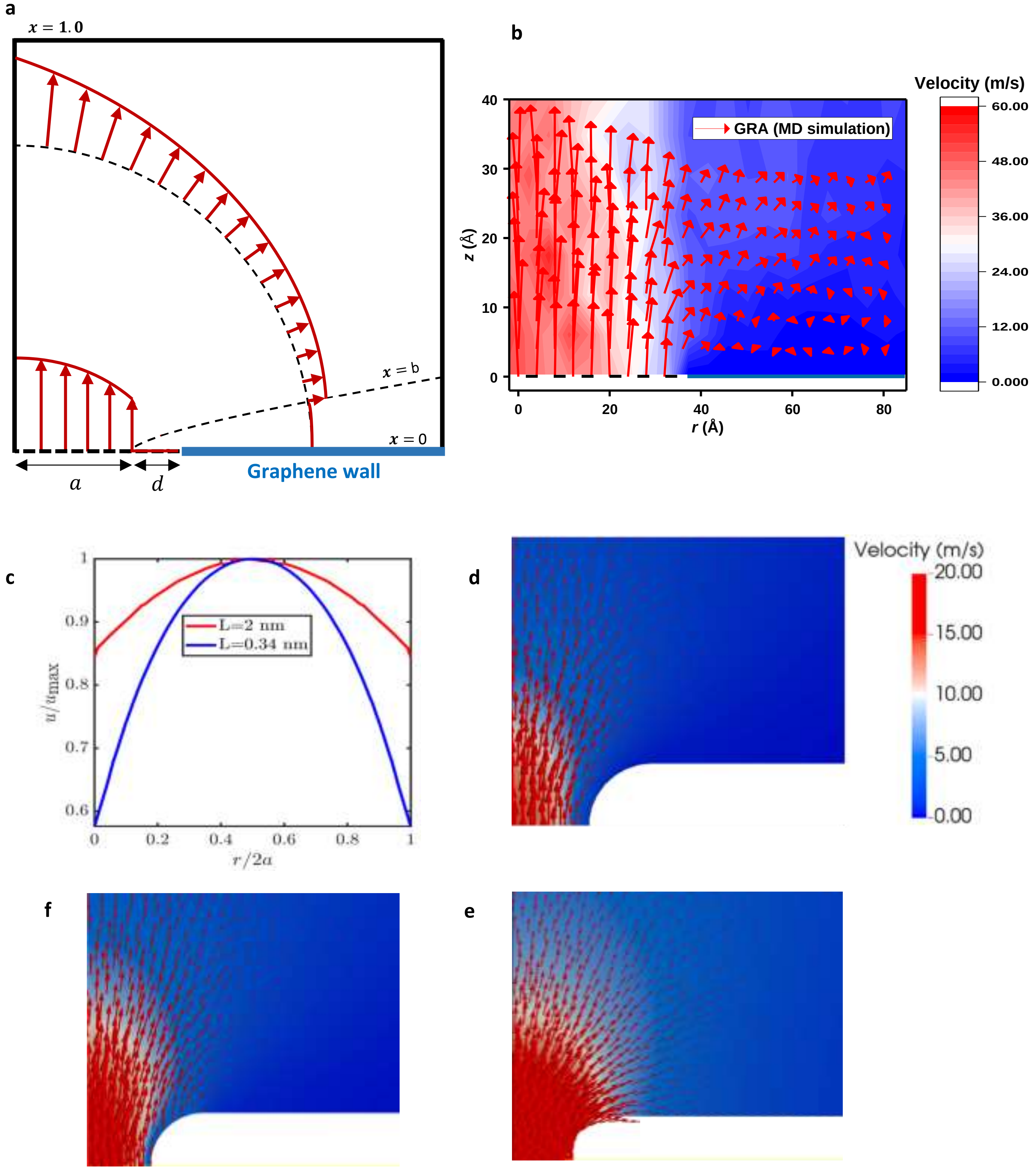

Figure C.4 a. The schematic of the velocity profiles (red) inside and outside the orifice pore in the corrected Sampson formulation are shown. Inside the orifice, based on the stream function in equation (4.6), the velocity is only nonzero a distance d away from boundary of the orifice (blue). d corresponds to $x = b$ outside the orifice. **b.** The velocity vector field (red arrows) is obtained in the MD simulation for a pressure

Figure C.4 (cont.) drop of 50MPa. Near the graphene surface (inside and outside the pore), the velocity almost vanishes similar to the velocity field in the corrected Sampson theory (**a**). The velocity jump (also shown in Figure 4.1b) inside the pore resembles the velocity jump ($r = a$, water assessable radius) modeled in the corrected Sampson. Velocity profile and velocity fields: **c-f.** obtained by NS model for pores with $a = 1.2$ nm, and pressure difference of 50 MP, **c.** Velocity profile, u , normalized by the maximum velocity, $u_{\max}$, as a function of the radial distance normalized by the pore diameter for thicknesses of 2 nm and 0.34 nm. **d-f.** Velocity field vectors of the pore with thickness of 2 nm for **d)** no-slip, **e)** partial slip (slip velocity of 5 m/s), and **f)** perfect slip conditions.

C.5 Viscosity Calculations

Viscosity is obtained using the Green-Kubo formalisms[91,92] $\mu_{ab} = \frac{V}{K_B T}\int_0^{\infty}\langle P_{ab}\,(0)\cdot P_{ab}(t)\rangle\,dt$ in equilibrium MD simulations. K_B, T, V, and $P_{ab}(t)$ are the Boltzmann constant, temperature, volume of the interested region and stress tensor, respectively. ab are the components of the stress tensor, $P_{ab} = \frac{1}{V}\left(\sum_i^N \frac{p_{ia}p_{ib}}{m_i} + \frac{1}{2}\sum_i^N \sum_{j\neq i}^N r_{ija}F_{ijb}\right)$ where i and j are atom indices, N is the number of atoms within the interested region, p_i is the momentum of atom i, m_i is the mass of atom i, r_{ij} and F_{ij} are the distance and force between the pair of atoms i and j, respectively. To find the thickness of the interfacial layer within which the water viscosity varies, a separate MD simulation is carried out (Figure C.5a; a flat graphene membrane (no pores) with water molecules (containing ~118,000 atoms with dimensions of 16.3nm along *1* and *2* axes, and 3nm along the *3*-axis)). In Figure C.5b, considering all the shear components of the stress tensor, the average viscosity $\left(\mu_{\text{ave}} = \frac{\mu_{12}+\mu_{13}+\mu_{23}}{3}\right)$ is calculated in different slabs (parallel to the graphene sheet) with a thickness of 0.3nm each (the black symbols). As shown, most of the variation takes place within ~0.8nm of the graphene wall. Therefore, L_{int} is set to be 0.8nm and the average effective interfacial viscosity is calculated to be $\mu_{\text{int}} = 0.98$ mPa.s within a slab with a thickness of 0.8nm ($V = 0.8\text{nm}\cdot 16.3\text{nm}\cdot 16.3\text{nm} = 212.56\text{nm}^3$).

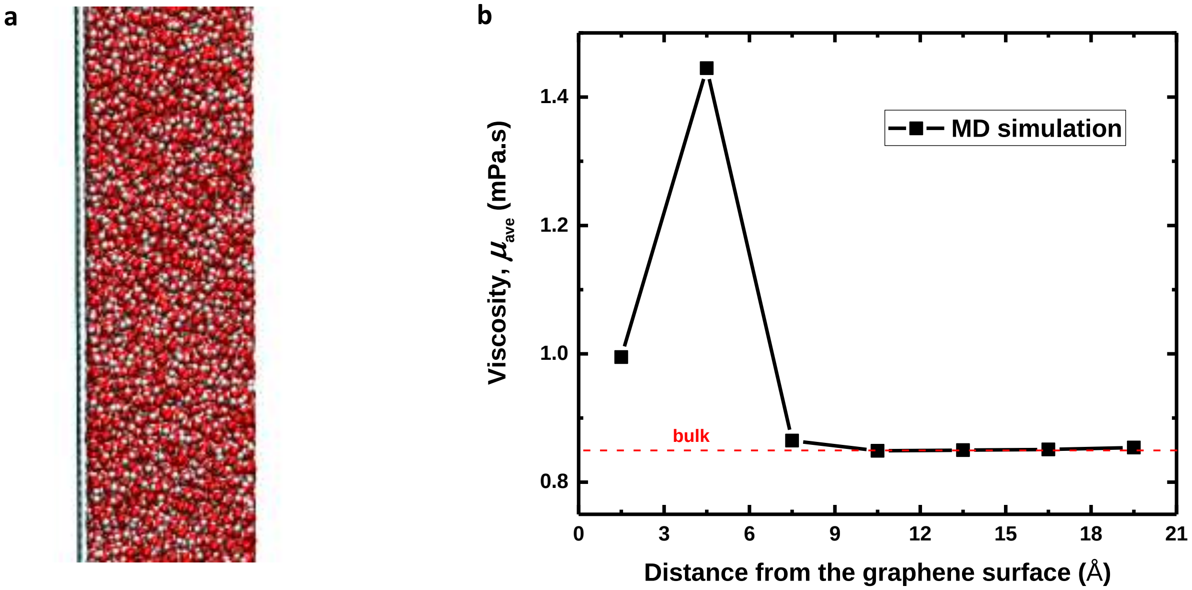

Figure C.5 a) Simulation box for water viscosity calculation near a water-graphene interface. Oxygen, hydrogen and carbon atoms are shown in red, white and cyan, respectively. **b)** Viscosity as a function of the distance from the graphene surface is shown (black symbols). The bulk viscosity (μ_{bulk} =0.85 mPa.s) is indicated by the dashed red line.

C.6 Oblate Spheroidal Coordinates

The differential operator in equation (4.4) is given by

$$D^2 = \frac{h_\phi}{h_t h_x}\left[\frac{\partial}{\partial t}\left(\frac{h_x}{h_\phi h_t}\frac{\partial}{\partial t}\right)+\frac{\partial}{\partial x}\left(\frac{h_t}{h_\phi h_x}\frac{\partial}{\partial x}\right)\right].$$

h_x, h_t and h_ϕ are the scale factors in the oblate spheroidal coordinates given by

$$h_x = \frac{\left(t^2+(a+d)^2 x^2\right)^{\frac{1}{2}}}{\left(1-x^2\right)^{\frac{1}{2}}}, \quad h_t = \frac{\left(t^2+(a+d)^2 x^2\right)^{\frac{1}{2}}}{\left(t^2+(a+d)^2\right)^{\frac{1}{2}}} \quad \& \quad h_\phi = \frac{\left(t^2+(a+d)^2\right)^{\frac{1}{2}}}{\left(1-x^2\right)^{\frac{1}{2}}} .$$

C.7 Comparison between Permeation Coefficients Predicted by the Corrected Sampson Theory and Measured Experiments

the permeation coefficients (or the inverse of hydrodynamic resistance) predicted by the corrected Sampson theory agree well with the experimentally measured coefficients. In Figure C.6, the filled square symbols are the experimental data taken directly from the ref.[30,34,103,174], the filled triangle symbols are the MD simulations data from other studies[29,175] and the circle symbols are the predicted permeation coefficients from the corrected Sampson theory. Based on the pore radius, the slip length is estimated using the data in Figure 4.1a. Knowing the ratio of radius to slip length $\left(\dfrac{\delta}{a}=\alpha\right)$, the permeation coefficient is predicted using equation (4.13).

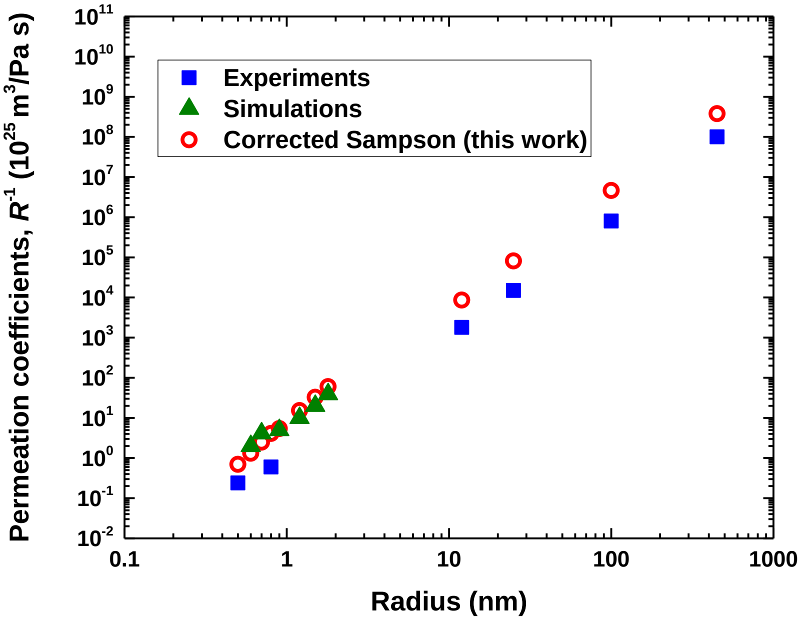

Figure C.6 Comparison of the predicted permeation coefficients from the correct Sampson theory with the experimentally[30,34,103,174] and computationally[29,175] measured permeation coefficients.

C.8 Nanotube Slip Length Estimation from Experimentally Measured Permeations

Estimation of slip lengths from experimentally measured permeation coefficients (or hydrodynamic resistance) depends on the models used to describe the resistance at the ends as well as in the inside of the CNT. The total resistance, which is directly obtained from experiments[85], can be written as the sum of the Sampson resistance and HP resistance, $R_{\text{total}} = R_{\text{Entrance-exit}} + R^{\text{HP}}_{\text{CNT}} = \dfrac{C\mu}{a^3} + \dfrac{8\mu h}{\pi\left(a^4 + 4a^3\delta_{\text{CNT}}\right)}$. δ_{CNT} is the slip length inside the CNTs (not at the entrance/exit). C is the pre-factor in the Sampson formula (C =3 in the original Sampson formula and $C = 3\left[\dfrac{1+2\left(\dfrac{\alpha}{1+\alpha}\right)^{\frac{3}{2}} - 3\left(\dfrac{\alpha}{1+\alpha}\right)}{\left(1+\alpha\right)^{\frac{3}{2}}}\right]$ for the slip and viscosity-corrected Sampson formula developed here). In Figure C.7, the estimated slip length inside CNTs (δ_{CNT}) is plotted as a function of different values of entrance/exit resistance (varying the pre-factor in Sampson formula) for one of the experimental data points in Secchi *et al.*[85] ($R_{\text{total}} = 12.96 \times 10^{20}$ Pa s/m^3 with a radius of 15 nm and $h = 700$ nm). Sampson formula (C =3) and the continuum fluid mechanics simulations in Secchi *et al.*[85] (where $C > 3$) result in large CNT slip lengths of 204 nm and 300 nm, respectively. However, the corrected Sampson formula, from which a value of C =1.8 is obtained (accessible radius of $a =$15-0.17=14.83nm with a graphene (entrance/exit) slip length of ~1.5nm is assumed. Hydrodynamic resistance is about 60% of that of the original Sampson theory as $\dfrac{a}{\delta} = \dfrac{1}{\alpha} = 9.88$), results in a smaller CNT slip length of 129.4 nm which is much closer to the slip lengths computed from the MD simulations. Therefore, we show when the entrance/exit resistance is estimated correctly, the experimentally measured total resistance values by Secchi *et al.*[85] lead to consistent CNT slip lengths with that of MD simulations, and that the slip lengths (whether at the entrance/exit or in the middle of CNTs) calculated by MD simulations are accurate by its very nature. This rules out the role of the possible electronic effects suggested by Secchi *et al*.[85] and shows that the CNT slip lengths calculated from MD simulations are consistent with experiments.

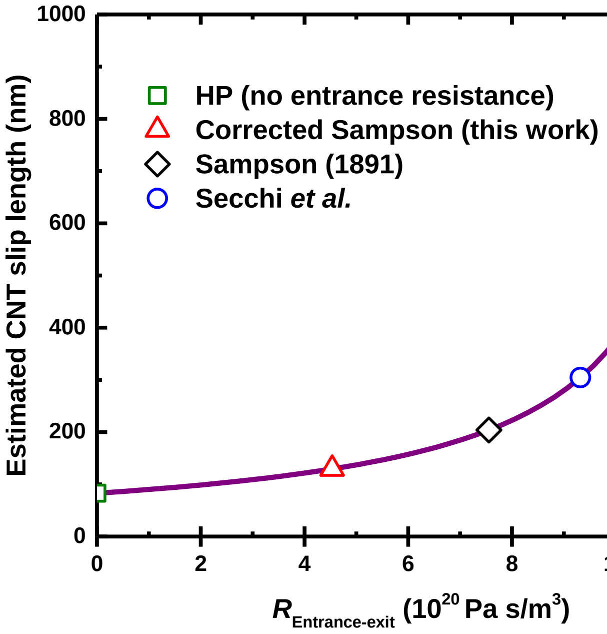

Figure C.7 Slip length in a 15 nm-radius CNT (with a length of 700 nm), estimated from the experimental total hydrodynamic resistance R_{total} (or inverse of permeation coefficient) given in Secchi *et al.* [85], is plotted as a function of varying entrance/exit hydrodynamic resistance $R_{\text{Entrance-exit}}$. The estimated CNT slip length varies significantly depending on the entrance/exit resistance obtained from different models. An accurate theory, therefore, is necessary to estimate the slip lengths inside CNTs (or any other nanotubes) from the experimentally measured permeation coefficients.

C.9 Estimation of Accessible Radius

The water accessible radius (a) is the length within which the water density is nonzero. In Table S1, a is calculated based on the water density profiles (the non-zero region excluding the depletion region) from MD simulations. The accessible radius is especially important for small-radius pores. Ideally, however, one should be able to calculate the accessible radius without performing MD simulations. The accessible radius can be systematically obtained by subtracting half of the LJ parameter $\left(\frac{\sigma_{\text{c-c}}}{2} = 0.17\text{nm}\right)$ from the carbon center-to-center radius. For the small-radius pores in Table S1, the accessible radii are almost identical to the calculated radii using LJ parameter (*e.g.*, the calculated radii in the first four rows are 0.2365, 0.3725, 0.508 and 0.775, respectively). As shown in Figure C.8, the recalculated data points (orange triangle symbols), based on the calculated accessible radius $a = a_{\text{center-to-center}} - \frac{\sigma_{\text{c-c}}}{2}$, are on top of the data points (black symbols) where the accessible radius is obtained along the distance within which the water density is zero. Therefore, subtracting $\frac{\sigma_{\text{c-c}}}{2} = 0.17\text{nm}$ from center-to-center radius is a good measure of calculating the accessible radius in graphitic pores.

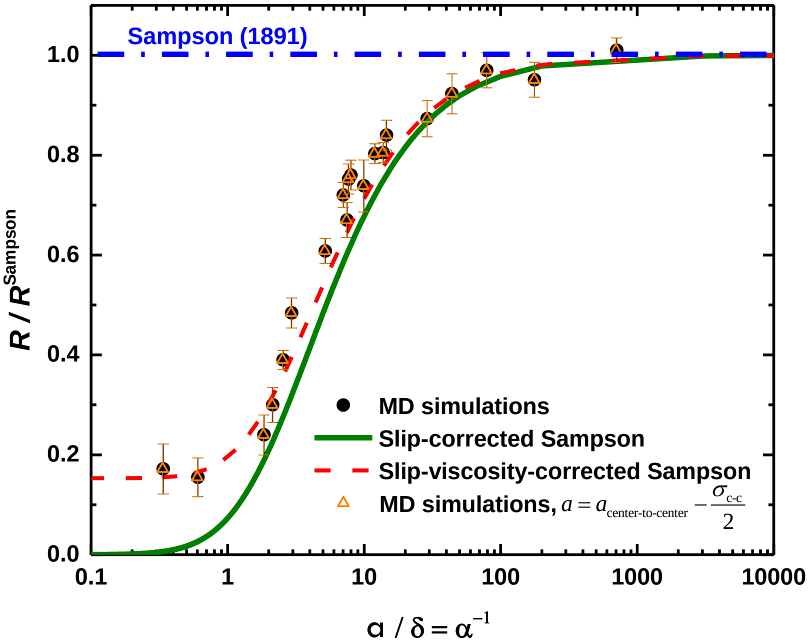

Figure C.8 Figure 4.3 is replotted with MD simulation data (orange hollow triangles) where the accessible radius (a) is calculated by subtracting half of the LJ parameter $\left(\frac{\sigma_{\text{c-c}}}{2} = 0.17\text{nm}\right)$ from the center-to-center radius $\left(a = a_{\text{center-to-center}} - \frac{\sigma_{\text{c-c}}}{2}\right)$.

Appendix D: Supplementary Information for Chapter 5

D.1 Simulation Boxes

In Figure D.1, the simulation schematics for the 5.01 nm-diameter graphene pore and 5.34 nm-long (37,37) CNT are shown. Ions are presented as green and purple spheres, and carbon atoms are shown in grey. Water molecules are mapped into a light blue continuum medium for a clear presentation.

D.2 Water Concentration

In Figure D.2, the water concentration is plotted as a function of the distance from the center of nanopores for the cases shown in Figure 5.2. In the thick nanopores (10.34nm-long CNTs), the water molecules are highly concentrated between the diffuse layer and Stern layer. In the low surface charge density CNT, the order of the nearest layers of molecules are water molecules and counter-ions (diffuse layer). In the high surface charge density CNT, the order is counter-ions (Stern layer), water molecules and co-ions/counter-ions of the diffuse layer. In the ultrathin graphene nanopores, the water molecules are the nearest molecules (highly concentrated) to the surface regardless of the strength of the surface charge density.

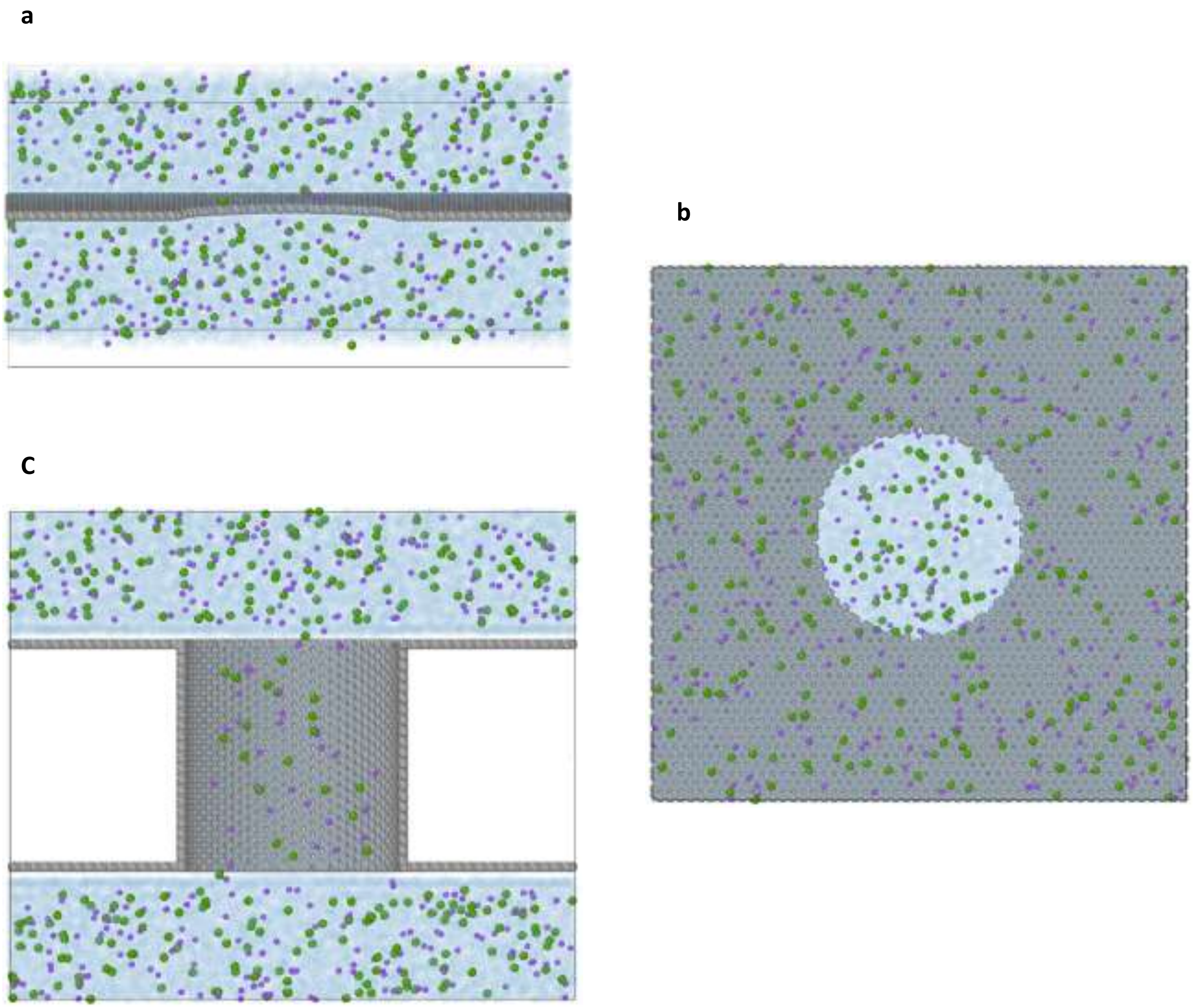

Figure D.1 a) Simulation box for the electrolyte solution across a single-layer graphene nanopore (side view). **b)** Membrane view of the graphene nanopore for a diameter of 5.01 nm. **c)** Simulation box for the electrolyte solution across a 5.34nm-long (37,37) CNT with a graphene sheet (with a pore similar to the size of the CNT) is drilled in each graphene sheet) at the both ends of the tube. The chloride ion, potassium ion, graphene and water are shown in green, purple, grey and light blue, respectively.

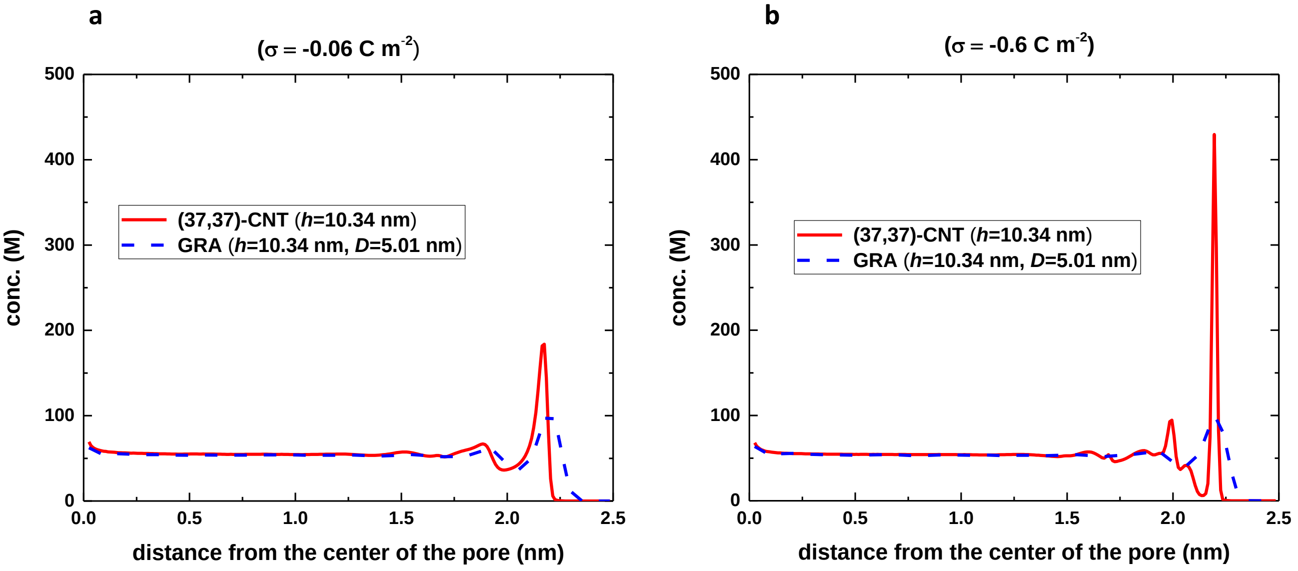

Figure D.2 Concentration of water as a function the distance from the center of a 10.34nm- (37,37) CNT and a similar diameter (5.01nm) graphene nanopore for **a)** low surface charge density of -0.06 C m^{-2} and **b)** high surface charge density of -0.6 C m^{-2}.

Appendix E: Supplementary Information for Chapter 6

E.1 Molecular Structure of DNA Bases

The molecular representations of DNA nucleotides (A, C, G and T) are illustrated in Figure E.1. The interaction of each nucleotide with the MscL pore depends on the structure and type of the atoms of each base. These interactions involve both VdW and Coulombic forces which are parameterized by the Lennard-Jones parameters (σ and ε) and the partial charges on each atom (tabulated in Table E.1 and Table E.2). The Lennard-Jones interaction energy is highest for oxygen atoms (ε_O=0.210), therefore, bases containing these protruding oxygen atoms exhibit stronger VdW interactions with the atoms of the pore. As shown in Figure E.1, base T has two oxygen atoms while base A does not contain any oxygen atoms which are consistent with the interaction forces calculated in the main article. The other Lennard-Jones parameter σ, which is representative of the size of an atom, plays an important role in the ionic current blockade.

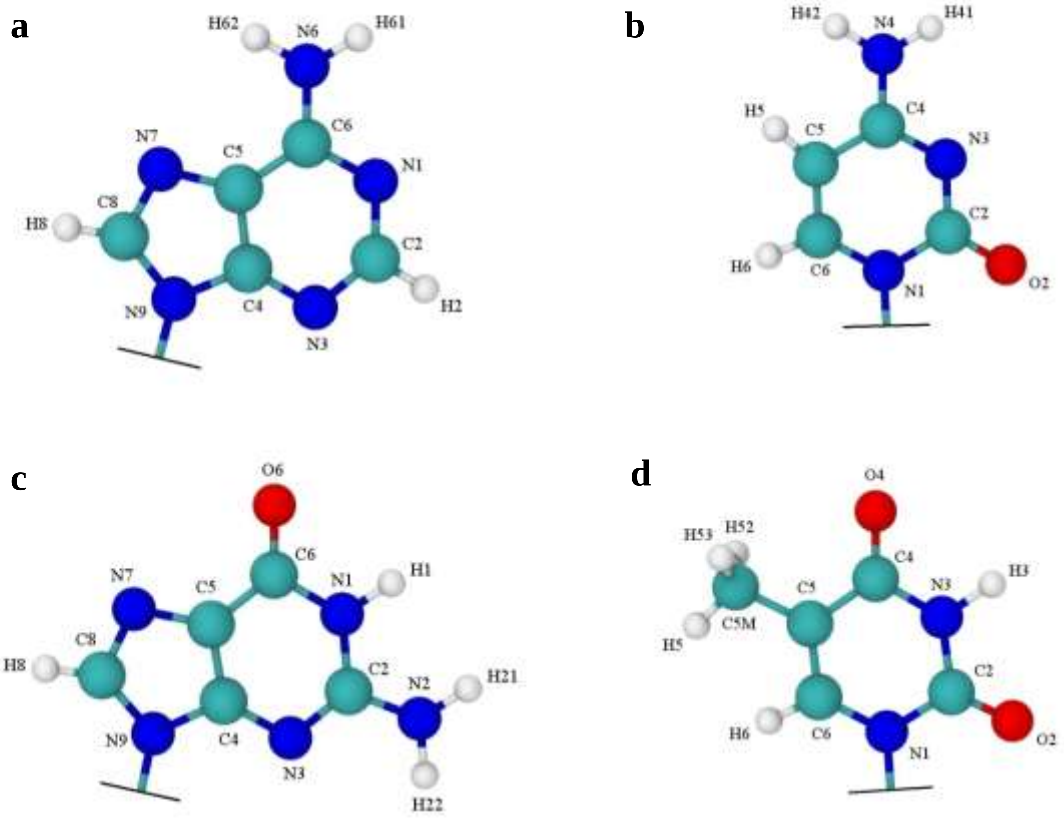

Figure E.1 Representation of DNA bases with their atom types (white: hydrogen atoms, blue: nitrogen atoms, cyan: carbon atoms and red: oxygen atoms). **a|** Base A. **b|** Base C. **c|** Base G. **d|** Base T.

Table E.1 Lennard-Jones parameters for atoms of bases.

Atom	σ (Å)	ε (kcal/mol)
O	2.96	0.210
N	3.25	0.170
C in C=O	3.75	0.105
All C (not in C=O)	3.50	0.080
H bonded to N	0.00	0.000
H Bonded to C	2.50	0.050

Table E.2 Partial charges on atoms of DNA bases.

Base A atom	Charge (e)	Base C atom	Charge (e)	Base G atom	Charge (e)	Base T atom	Charge (e)
N1	-0.6710	N1	-0.8420	N1	-0.6710	N1	-0.8680
C2	0.3434	C2	0.9470	H1	0.4050	C2	1.0340
H2	0.1610	O2	-0.6190	C2	0.9748	O2	-0.6040
N3	-0.6360	N3	-0.721	N2	-0.9560	N3	-0.1850
C4	0.6380	C4	0.6740	H21	0.3990	H3	0.4250
C5	0.0860	N4	-0.9240	H22	0.4170	C4	0.8270
C6	0.6510	H41	0.3940	N3	-0.7200	O4	-0.5880
N6	-0.7800	H42	0.4110	C4	0.6480	C5	-0.185
H61	0.3280	C5	-0.3830	C5	-0.0290	C5M	-0.1100
H62	0.3370	H5	0.2160	C6	0.8300	H5	0.0700
N7	-0.5877	C6	0.1950	O6	-0.5950	H52	0.0700
C8	0.3510	H6	0.2400	N7	0.5090	H53	0.0700
H8	0.1820			C8	0.2730	C6	0.1500
N9	-0.7430			H8	0.2220	H6	0.2400
				N9	-0.8240		

E.2 Ionic Current in MspA and MscL

To understand the effect of pore elasticity on the ionic current signals we acquired in MscL, we compared the ionic current signals obtained from translocation of ssDNAs in MspA and MscL pores (Figure E.2). In the main text, we already computed the time averaged ionic current for 4 different nucleotides in MscL. Here, we simulated the translocation of 4 ssDNA (PolydA(60), PolydT(60), PolydG(60) and PolydC(60)) through MspA. The only difference between MscL and MspA simulations is the type of protein. For MspA, we used the crystallography data with the PDB code:1UUN. The snapshots of the initial simulation of PolydA through MspA and MscL are shown in Figure E.2.

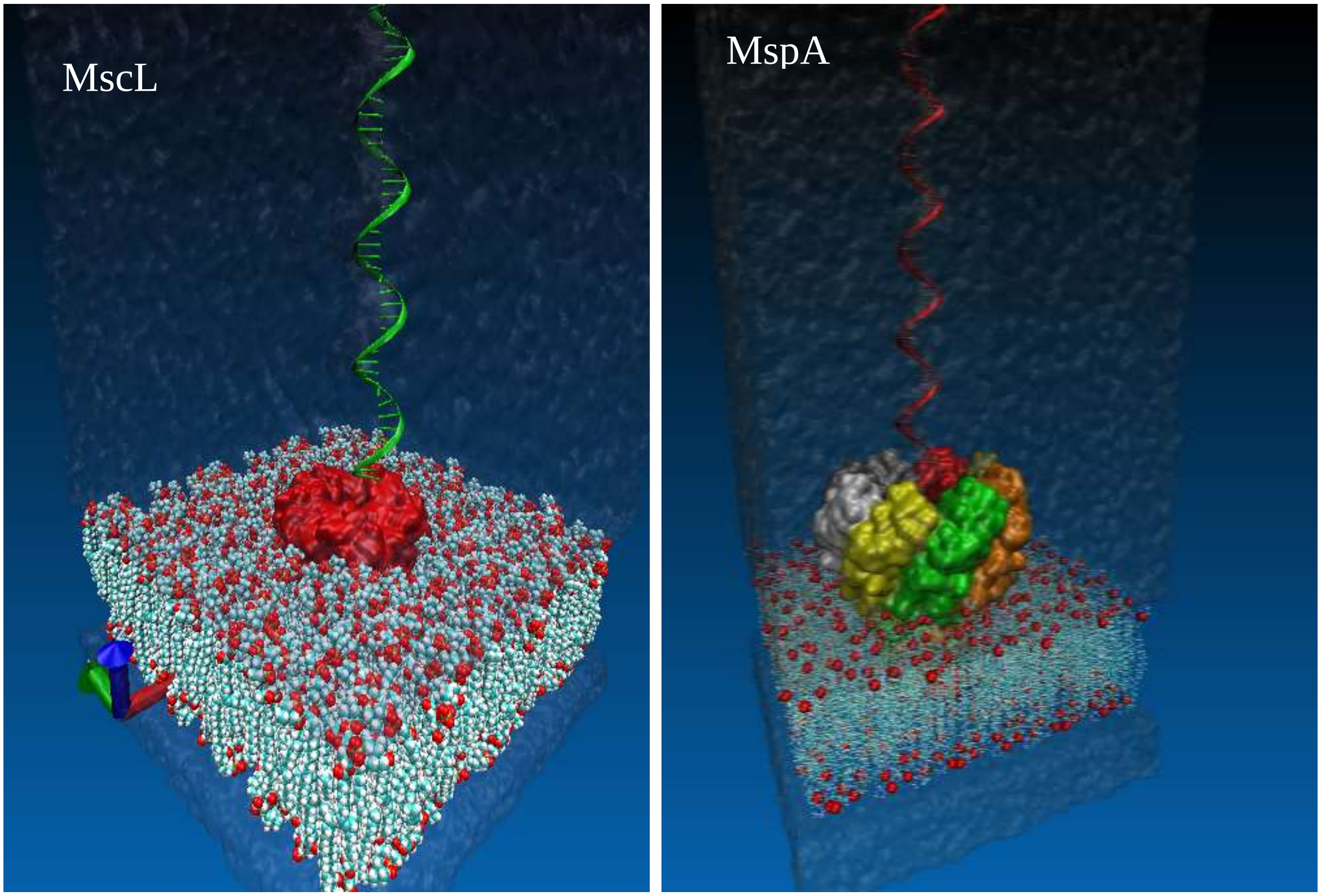

Figure E.2 Snapshots of simulation set up Left) MscL and Right) MspA.

The transmembrane bias of 0.5 V is applied in all cases. The average ionic current for bases A, C, G, and T through MspA and MscL are shown in Figure E.3. The level of currents for MspA is lower than the one in MscL. Also the order of currents for 4 bases is different in the two pores.

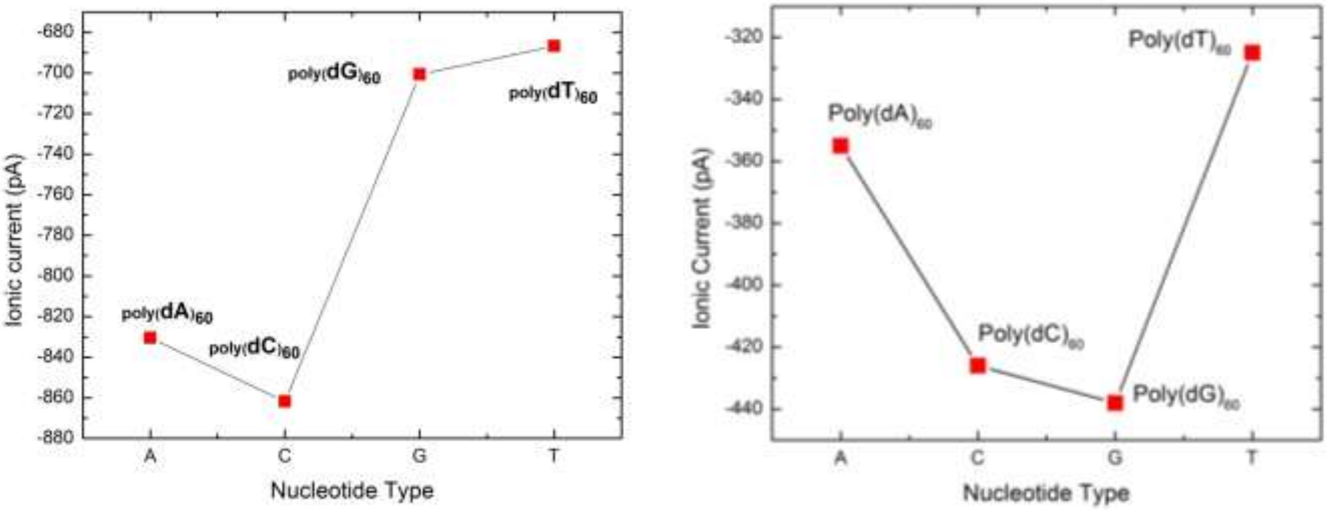

Figure E.3. Averaged ionic current for Poly(dA)$_{60}$, Poly(dC)$_{60}$, Poly(dT)$_{60}$ and Poly(dG)$_{60}$ for Left) MscL and Right) MspA

The maximum and minimum current difference, ΔI, is 113.1 pA and 189.2 pA for MspA and MscL, respectively. The signal strength is higher for MscL compared to MspA.

E.3 Signal to Noise (SNR) Calculation

SNR is defined as[66]

$$SNR = \frac{|\Delta I|}{I_{noise,RMS}}$$

where $|\Delta I|$ is the absolute current change due to protein translocation and $I_{noise,RMS}$ is the root-mean-square current noise. It is noteworthy that $I_{noise,RMS}$ equals the square root of the integral of the high-frequency current power spectral densities, which is defined as:

$$I_{noise,RMS} = \left(\int_0^{BW} S_I df \right)^{\frac{1}{2}}$$

where BW is the bandwidth and S_I is the power spectral density. The current power spectral density (S_I) is defined as:

$$S_I = \int_0^{\infty} < I(t) \cdot I(0) > \cos(\omega t) dt$$

where $I(t)$ is the instantaneous ionic current.

References

1 Heiranian, M., Farimani, A. B. & Aluru, N. R. Water desalination with a single-layer MoS_2 nanopore. *Nat. Commun.* **6**, 6, doi:10.1038/ncomms9616 (2015).

2 Feng, J. D. *et al.* Single-layer MoS_2 nanopores as nanopower generators. *Nature* **536**, 197, doi:10.1038/nature18593 (2016).

3 Farimani, A. B., Heiranian, M. & Aluru, N. R. Electromechanical Signatures for DNA Sequencing through a Mechanosensitive Nanopore. *J. Phys. Chem. Lett.* **6**, 650-657, doi:10.1021/jz5025417 (2015).

4 Barati Farimani, A., Heiranian, M., Min, K. & Aluru, N. R. Antibody Subclass Detection Using Graphene Nanopores. *The Journal of Physical Chemistry Letters* **8**, 1670-1676, doi:10.1021/acs.jpclett.7b00385 (2017).

5 Farimani, A. B., Heiranian, M. & Aluru, N. R. Identification of amino acids with sensitive nanoporous MoS_2: towards machine learning-based prediction. *Npj 2d Materials and Applications* **2**, 1-9, doi:10.1038/s41699-018-0060-8 (2018).

6 Wei, R. S., Gatterdam, V., Wieneke, R., Tampe, R. & Rant, U. Stochastic sensing of proteins with receptor-modified solid-state nanopores. *Nat. Nanotechnol.* **7**, 257-263, doi:10.1038/nnano.2012.24 (2012).

7 Yusko, E. C. *et al.* Controlling protein translocation through nanopores with bio-inspired fluid walls. *Nat. Nanotechnol.* **6**, 253-260, doi:10.1038/nnano.2011.12 (2011).

8 Han, A. *et al.* Label-free detection of single protein molecules and protein-protein interactions using synthetic nanopores. *Anal. Chem.* **80**, 4651-4658, doi:10.1021/ac7025207 (2008).

9 Han, A. P. *et al.* Sensing protein molecules using nanofabricated pores. *Appl. Phys. Lett.* **88**, doi:10.1063/1.2180868 (2006).

10 Kowalczyk, S. W. *et al.* Single-molecule transport across an individual biomimetic nuclear pore complex. *Nat. Nanotechnol.* **6**, 433-438, doi:10.1038/nnano.2011.88 (2011).

11 Majd, S. *et al.* Applications of biological pores in nanomedicine, sensing, and nanoelectronics. *Curr. Opin. Biotechnol.* **21**, 439-476, doi:10.1016/j.copbio.2010.05.002 (2010).

12 Aksimentiev, A., Heng, J. B., Timp, G. & Schulten, K. Microscopic kinetics of DNA translocation through synthetic nanopores. *Biophys. J.* **87**, 2086-2097, doi:10.1529/biophysj.104.042960 (2004).

13 Steinbock, L. J. *et al.* Probing the size of proteins with glass nanopores. *Nanoscale* **6**, 14380-14387, doi:10.1039/c4nr05001k (2014).

14 Farimani, A. B., Dibaeinia, P. & Aluru, N. R. DNA Origami-Graphene Hybrid Nanopore for DNA Detection. *ACS Appl. Mater. Interfaces* **9**, 92-100, doi:10.1021/acsami.6b11001 (2017).

15 Branton, D. *et al.* The potential and challenges of nanopore sequencing. *Nat. Biotechnol.* **26**, 1146-1153, doi:10.1038/nbt.1495 (2008).

16 Bayley, H. & Cremer, P. S. Stochastic sensors inspired by biology. *Nature* **413**, 226-230, doi:10.1038/35093038 (2001).

17 Larkin, J., Henley, R. Y., Muthukumar, M., Rosenstein, J. K. & Wanunu, M. High-Bandwidth Protein Analysis Using Solid-State Nanopores. *Biophys. J.* **106**, 696-704, doi:10.1016/j.bpj.2013.12.025 (2014).

18 Venkatesan, B. M. & Bashir, R. Nanopore sensors for nucleic acid analysis. *Nat. Nanotechnol.* **6**, 615-624, doi:10.1038/nnano.2011.129 (2011).

19 Elimelech, M. & Phillip, W. A. The Future of Seawater Desalination: Energy, Technology, and the Environment. *Science* **333**, 712-717, doi:10.1126/science.1200488 (2011).

20 Zhao, S. F., Zou, L., Tang, C. Y. Y. & Mulcahy, D. Recent developments in forward osmosis: Opportunities and challenges. *J. Membr. Sci.* **396**, 1-21, doi:10.1016/j.memsci.2011.12.023 (2012).

21 Shannon, M. A. *et al.* Science and technology for water purification in the coming decades. *Nature* **452**, 301-310, doi:10.1038/nature06599 (2008).

22 Fritzmann, C., Lowenberg, J., Wintgens, T. & Melin, T. State-of-the-art of reverse osmosis desalination. *Desalination* **216**, 1-76, doi:10.1016/j.desal.2006.12.009 (2007).

23 Khawaji, A. D., Kutubkhanah, I. K. & Wie, J. M. Advances in seawater desalination technologies. *Desalination* **221**, 47-69, doi:10.1016/j.desal.2007.01.067 (2008).

24 Humplik, T. *et al.* Nanostructured materials for water desalination. *Nanotechnology* **22**, doi:10.1088/0957-4484/22/29/292001 (2011).

25 Geise, G. M. *et al.* Water Purification by Membranes: The Role of Polymer Science. *J. Polym. Sci. Pt. B-Polym. Phys.* **48**, 1685-1718, doi:10.1002/polb.22037 (2010).

26 Lee, K. P., Arnot, T. C. & Mattia, D. A review of reverse osmosis membrane materials for desalination-Development to date and future potential. *J. Membr. Sci.* **370**, 1-22, doi:10.1016/j.memsci.2010.12.036 (2011).

27 Liu, K., Feng, J. D., Kis, A. & Radenovic, A. Atomically Thin Molybdenum Disulfide Nanopores with High Sensitivity for DNA Translocation. *ACS Nano* **8**, 2504-2511, doi:10.1021/nn406102h (2014).

28 Fornasiero, F. *et al.* Ion exclusion by sub-2-nm carbon nanotube pores. *Proc. Natl. Acad. Sci. U. S. A.* **105**, 17250-17255, doi:10.1073/pnas.0710437105 (2008).

29 Suk, M. E. & Aluru, N. R. Water Transport through Ultrathin Graphene. *J. Phys. Chem. Lett.* **1**, 1590-1594, doi:10.1021/jz100240r (2010).

30 O'Hern, S. C. *et al.* Selective Molecular Transport through Intrinsic Defects in a Single Layer of CVD Graphene. *ACS Nano* **6**, 10130-10138, doi:10.1021/nn303869m (2012).

31 Zhao, Y. D. *et al.* Two-Dimensional Material Membranes: An Emerging Platform for Controllable Mass Transport Applications. *Small* **10**, 4521-4542, doi:10.1002/smll.201401549 (2014).

32 Zhang, D. S. *et al.* Enhanced capacitive deionization performance of graphene/carbon nanotube composites. *J. Mater. Chem.* **22**, 14696-14704, doi:10.1039/c2jm31393f (2012).

33 Mishra, A. K. & Ramaprabhu, S. Functionalized graphene sheets for arsenic removal and desalination of sea water. *Desalination* **282**, 39-45, doi:10.1016/j.desal.2011.01.038 (2011).

34 Celebi, K. *et al.* Ultimate Permeation Across Atomically Thin Porous Graphene. *Science* **344**, 289-292, doi:10.1126/science.1249097 (2014).

35 Joseph, S. & Aluru, N. R. Why are carbon nanotubes fast transporters of water? *Nano Letters* **8**, 452-458, doi:10.1021/nl072385q (2008).

36 Suk, M. E., Raghunathan, A. V. & Aluru, N. R. Fast reverse osmosis using boron nitride and carbon nanotubes. *Appl. Phys. Lett.* **92**, doi:10.1063/1.2907333 (2008).

37 Cohen-Tanugi, D. & Grossman, J. C. Water Desalination across Nanoporous Graphene. *Nano Lett.* **12**, 3602-3608, doi:10.1021/nl3012853 (2012).

38 Sint, K., Wang, B. & Kral, P. Selective Ion Passage through Functionalized Graphene Nanopores. *J. Am. Chem. Soc.* **130**, 16448, doi:10.1021/ja804409f (2008).

39 Tang, Q., Zhou, Z. & Chen, Z. F. Graphene-related nanomaterials: tuning properties by functionalization. *Nanoscale* **5**, 4541-4583, doi:10.1039/c3nr33218g (2013).

40 Farimani, A. B., Min, K. & Aluru, N. R. DNA Base Detection Using a Single-Layer MoS_2. *Acs Nano* **8**, 7914-7922, doi:10.1021/nn5029295 (2014).

41 Radisavljevic, B., Radenovic, A., Brivio, J., Giacometti, V. & Kis, A. Single-layer MoS_2 transistors. *Nat. Nanotechnol.* **6**, 147-150, doi:10.1038/nnano.2010.279 (2011).

42 Bertolazzi, S., Brivio, J. & Kis, A. Stretching and Breaking of Ultrathin MoS2. *ACS Nano* **5**, 9703-9709, doi:10.1021/nn203879f (2011).

43 Gravelle, S. *et al.* Optimizing water permeability through the hourglass shape of aquaporins. *Proc. Natl. Acad. Sci. U. S. A.* **110**, 16367-16372, doi:10.1073/pnas.1306447110 (2013).

44 Waduge, P. *et al.* Direct and Scalable Deposition of Atomically Thin Low-Noise MoS_2 Membranes on Apertures. *ACS Nano*, doi:10.1021/acsnano.5b02369 (2015).

45 Feng, J. *et al.* Electrochemical Reaction in Single Layer MoS_2: Nanopores Opened Atom by Atom. *Nano Lett.* **15**, 3431-3438, doi:10.1021/acs.nanolett.5b00768 (2015).

46 Lee, Y. H. *et al.* Synthesis of Large-Area MoS_2 Atomic Layers with Chemical Vapor Deposition. *Adv. Mater.* **24**, 2320-2325, doi:10.1002/adma.201104798 (2012).

47 Dumcenco, D. *et al.* Large-Area Epitaxial Mono layer MoS_2. *ACS Nano* **9**, 4611-4620, doi:10.1021/acsnano.5b01281 (2015).

48 Coleman, J. N. *et al.* Two-Dimensional Nanosheets Produced by Liquid Exfoliation of Layered Materials. *Science* **331**, 568-571, doi:10.1126/science.1194975 (2011).

49 Smith, R. J. *et al.* Large-Scale Exfoliation of Inorganic Layered Compounds in Aqueous Surfactant Solutions. *Adv. Mater.* **23**, 3944, doi:10.1002/adma.201102584 (2011).

50 Liu, K. K. *et al.* Growth of Large-Area and Highly Crystalline MoS_2 Thin Layers on Insulating Substrates. *Nano Letters* **12**, 1538-1544, doi:10.1021/nl2043612 (2012).

51 Zhan, Y. J., Liu, Z., Najmaei, S., Ajayan, P. M. & Lou, J. Large-Area Vapor-Phase Growth and Characterization of MoS2 Atomic Layers on a SiO_2 Substrate. *Small* **8**, 966-971, doi:10.1002/smll.201102654 (2012).

52 Jeon, J. *et al.* Layer-controlled CVD growth of large-area two-dimensional MoS_2 films. *Nanoscale* **7**, 1688-1695, doi:10.1039/c4nr04532g (2015).

53 Mann, J. *et al.* 2-Dimensional Transition Metal Dichalcogenides with Tunable Direct Band Gaps: $MoS_{2(1-x)}Se_{2x}$ Monolayers. *Adv. Mater.* **26**, 1399-1404, doi:10.1002/adma.201304389 (2014).

54 van der Zande, A. M. *et al.* Grains and grain boundaries in highly crystalline monolayer molybdenum disulphide. *Nat. Mater.* **12**, 554-561, doi:10.1038/nmat3633 (2013).

55 Yu, Y. F. *et al.* Controlled Scalable Synthesis of Uniform, High-Quality Monolayer and Few-layer MoS_2 Films. *Scientific Reports* **3**, 6, doi:10.1038/srep01866 (2013).

56 Mizan, T. I., Savage, P. E. & Ziff, R. M. Molecular-dynamics of supercritical water using a flexible SPC model. *J. Phys. Chem.* **98**, 13067-13076, doi:10.1021/j100100a042 (1994).

57 Rosenberg, P. A. & Finkelstein, A. Water permeability of gramicidin-a-treated lipid bilayer membranes. *J. Gen. Physiol.* **72**, 341-350, doi:10.1085/jgp.72.3.341 (1978).

58 Suk, M. E. & Aluru, N. R. Effect of induced electric field on single-file reverse osmosis. *Phys. Chem. Chem. Phys.* **11**, 8614-8619, doi:10.1039/b903541a (2009).

59 Zhu, F. Q., Tajkhorshid, E. & Schulten, K. Pressure-induced water transport in membrane channels studied by molecular dynamics. *Biophys. J.* **83**, 154-160, doi:10.1016/s0006-3495(02)75157-6 (2002).

60 Liu, Y. H. *et al.* The preparation of a strawberry-like super-hydrophilic surface on the molybdenum substrate. *Colloid Surf. A-Physicochem. Eng. Asp.* **404**, 52-55, doi:10.1016/j.colsurfa.2012.04.008 (2012).

61 Gravelle, S., Joly, L., Ybert, C. & Bocquet, L. Large permeabilities of hourglass nanopores: From hydrodynamics to single file transport. *J. Chem. Phys.* **141**, doi:10.1063/1.4897253 (2014).

62 Bocquet, L. & Tabeling, P. Physics and technological aspects of nanofluidics. *Lab Chip* **14**, 3143-3158, doi:10.1039/c4lc00325j (2014).

63 Farimani, A. B., Aluru, N. R. & Tajkhorshid, E. Thermodynamic insight into spontaneous hydration and rapid water permeation in aquaporins. *Appl. Phys. Lett.* **105**, 83702-83702 (2014).

64 Jung, J. S., Preston, G. M., Smith, B. L., Guggino, W. B. & Agre, P. Molecular-structure of the water channel through aquaporin chip - the hourglass model. *J. Biol. Chem.* **269**, 14648-14654 (1994).

65 Hou, X., Guo, W. & Jiang, L. Biomimetic smart nanopores and nanochannels. *Chem. Soc. Rev.* **40**, 2385-2401, doi:10.1039/c0cs00053a (2011).

66 Dekker, C. Solid-state nanopores. *Nat. Nanotechnol.* **2**, 209-215, doi:10.1038/nnano.2007.27 (2007).

67 Heins, E. A., Siwy, Z. S., Baker, L. A. & Martin, C. R. Detecting single porphyrin molecules in a conically shaped synthetic nanopore. *Nano Letters* **5**, 1824-1829, doi:10.1021/nl050925i (2005).

68 Wu, Y. B. & Aluru, N. R. Graphitic Carbon-Water Nonbonded Interaction Parameters. *Journal of Physical Chemistry B* **117**, 8802-8813, doi:10.1021/jp402051t (2013).

69 Pendergast, M. M. & Hoek, E. M. V. A review of water treatment membrane nanotechnologies. *Energy Environ. Sci.* **4**, 1946-1971, doi:10.1039/c0ee00541j (2011).

70 Li, L. X., Dong, J. H., Nenoff, T. M. & Lee, R. Desalination by reverse osmosis using MFI zeolite membranes. *J. Membr. Sci.* **243**, 401-404, doi:10.1016/j.memsci.2004.06.045 (2004).

71 Guillen, G. & Hoek, E. M. V. Modeling the impacts of feed spacer geometry on reverse osmosis and nanofiltration processes. *Chem. Eng. J.* **149**, 221-231, doi:10.1016/j.cej.2008.10.030 (2009).

72 Plimpton, S. Fast parallel algorithms for short-range molecular-dynamics. *J. Comput. Phys.* **117**, 1-19, doi:10.1006/jcph.1995.1039 (1995).

73 Humphrey, W., Dalke, A. & Schulten, K. VMD: Visual molecular dynamics. *Journal of Molecular Graphics & Modelling* **14**, 33-38, doi:10.1016/0263-7855(96)00018-5 (1996).

74 Hockney, R. W. & Eastwood, J. W. *Computer simulation using particles*. (Taylor-Francis, Inc., 1988).

75 Nose, S. A unified formulation of the constant temperature molecular-dynamics methods. *J. Chem. Phys.* **81**, 511-519 (1984).

76 Hoover, W. G. Canonical dynamics - equilibrium phase-space distributions. *Phys. Rev. A* **31**, 1695-1697, doi:10.1103/PhysRevA.31.1695 (1985).

77 Koga, K., Gao, G. T., Tanaka, H. & Zeng, X. C. Formation of ordered ice nanotubes inside carbon nanotubes. *Nature* **412**, 802-805, doi:10.1038/35090532 (2001).

78 Mashl, R. J., Joseph, S., Aluru, N. R. & Jakobsson, E. Anomalously immobilized water: A new water phase induced by confinement in nanotubes. *Nano Lett.* **3**, 589-592, doi:10.1021/nl0340226 (2003).

79 Majumder, M., Chopra, N., Andrews, R. & Hinds, B. J. Nanoscale hydrodynamics - Enhanced flow in carbon nanotubes. *Nature* **438**, 44-44, doi:10.1038/43844a (2005).

80 Holt, J. K. *et al.* Fast mass transport through sub-2-nanometer carbon nanotubes. *Science* **312**, 1034-1037, doi:10.1126/science.1126298 (2006).

81 Falk, K., Sedlmeier, F., Joly, L., Netz, R. R. & Bocquet, L. Molecular Origin of Fast Water Transport in Carbon Nanotube Membranes: Superlubricity versus Curvature Dependent Friction. *Nano Lett.* **10**, 4067-4073, doi:10.1021/nl1021046 (2010).

82 Farimani, A. B., Heiranian, M. & Aluru, N. R. Nano-electro-mechanical pump: Giant pumping of water in carbon nanotubes. *Sci Rep* **6**, 6, doi:10.1038/srep26211 (2016).

83 Feng, J. D. *et al.* Identification of single nucleotides in MoS_2 nanopores. *Nat. Nanotechnol.* **10**, 1070, doi:10.1038/nnano.2015.219 (2015).

84 Hummer, G., Rasaiah, J. C. & Noworyta, J. P. Water conduction through the hydrophobic channel of a carbon nanotube. *Nature* **414**, 188-190, doi:10.1038/35102535 (2001).

85 Secchi, E. *et al.* Massive radius-dependent flow slippage in carbon nanotubes. *Nature* **537**, 210-213, doi:10.1038/nature19315 (2016).

86 Xie, Q. *et al.* Fast water transport in graphene nanofluidic channels. *Nat. Nanotechnol.* **13**, 238, doi:10.1038/s41565-017-0031-9 (2018).

87 Suk, M. E. & Aluru, N. R. Molecular and continuum hydrodynamics in graphene nanopores. *Rsc Advances* **3**, 9365-9372, doi:10.1039/c3ra40661j (2013).

88 Buchheim, J., Schlichting, K. P., Wyss, R. M. & Park, H. G. Assessing the Thickness-Permeation Paradigm in Nanoporous Membranes. *ACS Nano* **13**, 134-142, doi:10.1021/acsnano.8b04875 (2019).

89 Thomas, J. A. & McGaughey, A. J. H. Water Flow in Carbon Nanotubes: Transition to Subcontinuum Transport. *Physical Review Letters* **102**, doi:10.1103/PhysRevLett.102.184502 (2009).

90 Thomas, J. A. & McGaughey, A. J. H. Reassessing fast water transport through carbon nanotubes. *Nano Lett.* **8**, 2788-2793, doi:10.1021/nl8013617 (2008).

91 Bocquet, L. & Barrat, J. L. Hydrodynamic boundary-conditions, correlation-functions, and Kubo relations for confined fluids. *Physical Review E* **49**, 3079-3092, doi:10.1103/PhysRevE.49.3079 (1994).

92 Zwanzig, R. Time-correlation functions and transport coefficients in statistical mechanics. *Annual Review of Physical Chemistry* **16**, 67-&, doi:10.1146/annurev.pc.16.100165.000435 (1965).

93 Babu, J. S. & Sathian, S. P. The role of activation energy and reduced viscosity on the enhancement of water flow through carbon nanotubes. *J. Chem. Phys.* **134**, doi:10.1063/1.3592532 (2011).

94 Suk, M. E. & Aluru, N. R. Modeling Water Flow Through Carbon Nanotube Membranes with Entrance/Exit Effects. *Nanoscale and Microscale Thermophysical Engineering* **21**, 247-262, doi:10.1080/15567265.2017.1355949 (2017).

95 Farimani, A. B. & Aluru, N. R. Spatial Diffusion of Water in Carbon Nanotubes: From Fickian to Ballistic Motion. *Journal of Physical Chemistry B* **115**, 12145-12149, doi:10.1021/jp205877b (2011).

96 Dagan, Z., Weinbaum, S. & Pfeffer, R. An infinite-series solution for the creeping motion through an orifice of finite length. *Journal of Fluid Mechanics* **115**, 505-523, doi:10.1017/s0022112082000883 (1982).

97 Verweij, H., Schillo, M. C. & Li, J. Fast mass transport through carbon nanotube membranes. *Small* **3**, 1996-2004, doi:10.1002/smll.200700368 (2007).

98 Schrader, M. E. Ultrahigh-vacuum techniques in the measurement of contact angles .5. Leed study of the effect of structure on the wettability of graphite. *Journal of Physical Chemistry* **84**, 2774-2779, doi:10.1021/j100458a021 (1980).

99 Sam, A., Kannam, S. K., Hartkamp, R. & Sathian, S. P. Water flow in carbon nanotubes: The effect of tube flexibility and thermostat. *J. Chem. Phys.* **146**, doi:10.1063/1.4985252 (2017).

100 Darden, T., York, D. & Pedersen, L. Particle mesh ewald method for Ewald sums in large systems. *J. Chem. Phys.* **98**, 10089-10092, doi:10.1063/1.464397 (1993).

101 Qin, X. C., Yuan, Q. Z., Zhao, Y. P., Xie, S. B. & Liu, Z. F. Measurement of the Rate of Water Translocation through Carbon Nanotubes. *Nano Lett.* **11**, 2173-2177, doi:10.1021/n1200843g (2011).

102 Kim, S. *et al.* Fabrication of flexible, aligned carbon nanotube/polymer composite membranes by in-situ polymerization. *Journal of Membrane Science* **460**, 91-98, doi:10.1016/j.memsci.2014.02.016 (2014).

103 Surwade, S. P. *et al.* Water desalination using nanoporous single-layer graphene. *Nat. Nanotechnol.* **10**, 459-464, doi:10.1038/nnano.2015.37 (2015).

104 Walther, J. H., Ritos, K., Cruz-Chu, E. R., Megaridis, C. M. & Koumoutsakos, P. Barriers to Superfast Water Transport in Carbon Nanotube Membranes. *Nano Lett.* **13**, 1910-1914, doi:10.1021/nl304000k (2013).

105 Bui, N. *et al.* Ultrabreathable and Protective Membranes with Sub-5 nm Carbon Nanotube Pores. *Advanced Materials* **28**, 5871, doi:10.1002/adma.201600740 (2016).

106 Qin, Y. Z. *et al.* Ultrafast Nanofiltration through Large-Area Single-Layered Graphene Membranes. *ACS Appl. Mater. Interfaces* **9**, 9239-9244, doi:10.1021/acsami.7b00504 (2017).

107 Yang, Y. B. *et al.* Large-area graphene-nanomesh/carbon-nanotube hybrid membranes for ionic and molecular nanofiltration. *Science* **364**, 1057, doi:10.1126/science.aau5321 (2019).

108 Stanford, M. G., Rack, P. D. & Jariwala, D. Emerging nanofabrication and quantum confinement techniques for 2D materials beyond graphene. *Npj 2d Materials and Applications* **2**, doi:10.1038/s41699-018-0065-3 (2018).

109 Faucher, S. *et al.* Critical Knowledge Gaps in Mass Transport through Single-Digit Nanopores: A Review and Perspective. *J. Phys. Chem. C* **123**, 21309-21326, doi:10.1021/acs.jpcc.9b02178 (2019).

110 Kurotobi, K. & Murata, Y. A Single Molecule of Water Encapsulated in Fullerene C-60. *Science* **333**, 613-616, doi:10.1126/science.1206376 (2011).

111 Farimani, A. B., Wu, Y. B. & Aluru, N. R. Rotational motion of a single water molecule in a buckyball. *Physical Chemistry Chemical Physics* **15**, 17993-18000, doi:10.1039/c3cp53277a (2013).

112 Joseph, S. & Aluru, N. R. Pumping of confined water in carbon nanotubes by rotation-translation coupling. *Physical Review Letters* **101**, doi:10.1103/PhysRevLett.101.064502 (2008).

113 Li, H. *et al.* Experimental Realization of Few Layer Two-Dimensional MoS_2 Membranes of Near Atomic Thickness for High Efficiency Water Desalination. *Nano Lett.* **19**, 5194-5204, doi:10.1021/acs.nanolett.9b01577 (2019).

114 Farimani, A. B., Aluru, N. R. & Tajkhorshid, E. Thermodynamic insight into spontaneous hydration and rapid water permeation in aquaporins. *Appl. Phys. Lett.* **105**, doi:10.1063/1.4893782 (2014).

115 Mohammad Heiranian, N. R. A. Nanofluidic transport theory with enhancement factors 1.

116 Couette, M. Studies relating to the motion of liquids. *Ann. Chim. Phys.* **21**, 433-510 (1890).

117 Hagen, G. H. L. Uber die Bewegung des Wassers in engen cylindrischen Rohren. *Poggendorf's Annalen der Physik und Chemie* **46**, 423-442 (1839).

118 Poiseuille, J. L. M. Recherches experimentales sur Ie mouvement des liquides dans les tubes de tres petits diametres; 1. Influence de la pression sur la quantite de Iiquide qui traverse les tubes de tres petits diametres. *C. R. Acad. Sci.* **11**, 961-967 (1840).

119 Sampson, R. A. XII. On Stokes's current function. *Philosophical transctions of the royal society A* **182**, 449 (1891).

120 Weissberg, H. L. End correction for slow viscous flow through long tubes. *Physics of Fluids* **5**, 1033-1036, doi:10.1063/1.1724469 (1962).

121 Milne-Thomson, L. M. *Theoretical Hydrodynamics*. (Dover Publications, 2013).

122 Goldstein, S. & Council, A. R. *Modern Developments in Fluid Dynamics: An Account of Theory and Experiment Relating to Boundary Layers, Turbulent Motion and Wakes*. (The Clarendon Press, 1938).

123 Wang, E. N. & Karnik, R. Water desalination Graphene cleans up water. *Nat. Nanotechnol.* **7**, 552-554 (2012).

124 Rollings, R. C., Kuan, A. T. & Golovchenko, J. A. Ion selectivity of graphene nanopores. *Nat. Commun.* **7**, 7, doi:10.1038/ncomms11408 (2016).

125 Cazade, P. A., Hartkamp, R. & Coasne, B. Structure and Dynamics of an Electrolyte Confined in Charged Nanopores. *J. Phys. Chem. C* **118**, 5061-5072, doi:10.1021/jp4098638 (2014).

126 Karnik, R. *et al.* Electrostatic control of ions and molecules in nanofluidic transistors. *Nano Lett.* **5**, 943-948, doi:10.1021/nl050493b (2005).

127 Buie, C. R. *et al.* Water management in proton exchange membrane fuel cells using integrated electroosmotic pumping. *Journal of Power Sources* **161**, 191-202, doi:10.1016/j.jpowsour.2006.03.021 (2006).

128 Kulkarni, G. S. & Zhong, Z. H. Detection beyond the Debye Screening Length in a High-Frequency Nanoelectronic Biosensor. *Nano Lett.* **12**, 719-723, doi:10.1021/nl203666a (2012).

129 Zhang, L. L. & Zhao, X. S. Carbon-based materials as supercapacitor electrodes. *Chemical Society Reviews* **38**, 2520-2531, doi:10.1039/b813846j (2009).

130 Zhai, Y. P. *et al.* Carbon Materials for Chemical Capacitive Energy Storage. *Advanced Materials* **23**, 4828-4850, doi:10.1002/adma.201100984 (2011).

131 Simon, P. & Gogotsi, Y. Materials for electrochemical capacitors. *Nat. Mater.* **7**, 845-854, doi:10.1038/nmat2297 (2008).

132 Helmholtz, H. Ueber einige Gesetze der Vertheilung elektrischer Ströme in körperlichen Leitern mit Anwendung auf die thierisch-elektrischen Versuche. (1853).

133 Schmid, G. M. Electrical double-layer at a metal-dilute electrolyte solution interface - MARTYNOV,GA, SALEM,RR. *J. Am. Chem. Soc.* **106**, 1176-1176 (1984).

134 Stern, O. Zur Theorie der Elektrolytischen Doppelschicht". Zeitschrift für Elektrochemie. (1924).

135 Jiang, G. P., Cheng, C., Li, D. & Liu, J. Z. Molecular dynamics simulations of the electric double layer capacitance of graphene electrodes in mono-valent aqueous electrolytes. *Nano Research* **9**, 174-186, doi:10.1007/s12274-015-0978-5 (2016).

136 Joseph, S. & Aluru, N. R. Hierarchical multiscale simulation of electrokinetic transport in silica nanochannels at the point of zero charge. *Langmuir* **22**, 9041-9051, doi:10.1021/la0610147 (2006).

137 Joung, I. S. & Cheatham, T. E. Determination of alkali and halide monovalent ion parameters for use in explicitly solvated biomolecular simulations. *Journal of Physical Chemistry B* **112**, 9020-9041, doi:10.1021/jp8001614 (2008).

138 Kasianowicz, J. J., Brandin, E., Branton, D. & Deamer, D. W. Characterization of individual polynucleotide molecules using a membrane channel. *Proceedings of the National Academy of Sciences of the United States of America* **93**, 13770-13773, doi:10.1073/pnas.93.24.13770 (1996).

139 Braha, O. *et al.* Designed protein pores as components for biosensors. *Chem. Biol.* **4**, 497-505, doi:10.1016/s1074-5521(97)90321-5 (1997).

140 Gu, L. Q., Braha, O., Conlan, S., Cheley, S. & Bayley, H. Stochastic sensing of organic analytes by a pore-forming protein containing a molecular adapter. *Nature* **398**, 686-690 (1999).

141 Howorka, S., Cheley, S. & Bayley, H. Sequence-specific detection of individual DNA strands using engineered nanopores. *Nat. Biotechnol.* **19**, 636-639, doi:10.1038/90236 (2001).

142 Clarke, J. *et al.* Continuous base identification for single-molecule nanopore DNA sequencing. *Nat. Nanotechnol.* **4**, 265-270, doi:10.1038/nnano.2009.12 (2009).

143 Kircher, M. & Kelso, J. High-throughput DNA sequencing - concepts and limitations. *Bioessays* **32**, 524-536, doi:10.1002/bies.200900181 (2010).

144 Akeson, M., Branton, D., Kasianowicz, J. J., Brandin, E. & Deamer, D. W. Microsecond time-scale discrimination among polycytidylic acid, polyadenylic acid, and polyuridylic acid as homopolymers or as segments within single RNA molecules. *Biophys. J.* **77**, 3227-3233 (1999).

145 Butler, T. Z., Pavlenok, M., Derrington, I. M., Niederweis, M. & Gundlach, J. H. Single-molecule DNA detection with an engineered MspA protein nanopore. *Proc. Natl. Acad. Sci. U. S. A.* **105**, 20647-20652, doi:10.1073/pnas.0807514106 (2008).

146 Chang, G., Spencer, R. H., Lee, A. T., Barclay, M. T. & Rees, D. C. Structure of the MscL homolog from Mycobacterium tuberculosis: A gated mechanosensitive ion channel. *Science* **282**, 2220-2226, doi:10.1126/science.282.5397.2220 (1998).

147 Siwy, Z. S. & Davenport, M. NANOPORES Graphene opens up to DNA. *Nat. Nanotechnol.* **5**, 697-698, doi:10.1038/nnano.2010.198 (2010).

148 Wells, D. B., Belkin, M., Comer, J. & Aksimentiev, A. Assessing Graphene Nanopores for Sequencing DNA. *Nano Lett.* **12**, 4117-4123, doi:10.1021/nl301655d (2012).

149 Min, S. K., Kim, W. Y., Cho, Y. & Kim, K. S. Fast DNA sequencing with a graphene-based nanochannel device. *Nat. Nanotechnol.* **6**, 162-165, doi:10.1038/nnano.2010.283 (2011).

150 Saha, K. K., Drndic, M. & Nikolic, B. K. DNA Base-Specific Modulation of Microampere Transverse Edge Currents through a Metallic Graphene Nanoribbon with a Nanopore. *Nano Lett.* **12**, 50-55, doi:10.1021/nl202870y (2012).

151 Liu, Y. X., Dong, X. C. & Chen, P. Biological and chemical sensors based on graphene materials. *Chem. Soc. Rev.* **41**, 2283-2307, doi:10.1039/c1cs15270j (2012).

152 Prasongkit, J., Grigoriev, A., Pathak, B., Ahuja, R. & Scheicher, R. H. Transverse Conductance of DNA Nucleotides in a Graphene Nanogap from First Principles. *Nano Lett.* **11**, 1941-1945, doi:10.1021/nl200147x (2011).

153 Sukharev, S., Durell, S. R. & Guy, H. R. Structural models of the MscL gating mechanism. *Biophysical Journal* **81**, 917-936 (2001).

154 Sukharev, S., Betanzos, M., Chiang, C. S. & Guy, H. R. The gating mechanism of the large mechanosensitive channel MscL. *Nature* **409**, 720-724, doi:10.1038/35055559 (2001).

155 Sukharev, S. & Anishkin, A. Mechanosensitive channels: what can we learn from 'simple' model systems? *Trends in Neurosciences* **27**, 345-351, doi:10.1016/j.tins.2004.04.006 (2004).

156 Jeon, J. & Voth, G. A. Gating of the mechanosensitive channel protein MscL: The interplay of membrane and protein. *Biophysical Journal* **94**, 3497-3511, doi:10.1529/biophysj.107.109850 (2008).

157 Sukharev, S. I., Blount, P., Martinac, B., Blattner, F. R. & Kung, C. A large-conductance mechanosensitive channel in E. Coli encoded by MscL alone. *Nature* **368**, 265-268, doi:10.1038/368265a0 (1994).

158 Perozo, E., Cortes, D. M., Sompornpisut, P., Kloda, A. & Martinac, B. Open channel structure of MscL and the gating mechanism of mechanosensitive channels. *Nature* **418**, 942-948, doi:10.1038/nature00992 (2002).

159 Gullingsrud, J., Kosztin, D. & Schulten, K. Structural determinants of MscL gating studied by molecular dynamics simulations. *Biophysical Journal* **80**, 2074-2081 (2001).

160 Gullingsrud, J. & Schulten, K. Gating of MscL studied by steered molecular dynamics. *Biophysical Journal* **85**, 2087-2099, doi:10.1016/s0006-3495(03)74637-2 (2003).

161 Gullingsrud, J. & Schulten, K. Lipid bilayer pressure profiles and mechanosensitive channel gating. *Biophysical Journal* **86**, 3496-3509, doi:10.1529/biophysj.103.034322 (2004).

162 Barriga, H. M. G. *et al.* Droplet interface bilayer reconstitution and activity measurement of the mechanosensitive channel of large conductance from Escherichia coli. *J. R. Soc. Interface* **11**, doi:10.1098/rsif.2014.0404 (2014).

163 Yang, L. M. *et al.* Three Routes To Modulate the Pore Size of the MscL Channel/Nanovalve. *Acs Nano* **6**, 1134-1141, doi:10.1021/nn203703j (2012).

164 Kale, L. *et al.* NAMD2: Greater scalability for parallel molecular dynamics. *J. Comput. Phys.* **151**, 283-312, doi:10.1006/jcph.1999.6201 (1999).

165 MacKerell, A. D. & Banavali, N. K. All-atom empirical force field for nucleic acids: II. Application to molecular dynamics simulations of DNA and RNA in solution. *J. Comput. Chem.* **21**, 105-120, doi:10.1002/(sici)1096-987x(20000130)21:2<105::aid-jcc3>3.0.co;2-p (2000).

166 Gosse, C. & Croquette, V. Magnetic tweezers: Micromanipulation and force measurement at the molecular level. *Biophysical Journal* **82**, 3314-3329 (2002).

167 Monajemi, M., Ketabi, S., Zadeh, M. H. & Amiri, A. Simulation of DNA bases in water: Comparison of the Monte Carlo algorithm with molecular mechanics force fields. *Biochem.-Moscow* **71**, S1-S8, doi:10.1134/s0006297906130013 (2006).

168 Deamer, D. W. & Branton, D. Characterization of nucleic acids by nanopore analysis. *Accounts Chem. Res.* **35**, 817-825, doi:10.1021/ar000138m (2002).

169 Derrington, I. M. *et al.* Nanopore DNA sequencing with MspA. *Proc. Natl. Acad. Sci. U. S. A.* **107**, 16060-16065, doi:10.1073/pnas.1001831107 (2010).

170 Faller, M., Niederweis, M. & Schulz, G. E. The structure of a mycobacterial outer-membrane channel. *Science* **303**, 1189-1192, doi:10.1126/science.1094114 (2004).

171 Liang, T., Phillpot, S. R. & Sinnott, S. B. Parametrization of a reactive many-body potential for Mo-S systems. *Phys. Rev. B* **79**, doi:10.1103/PhysRevB.79.245110 (2009).

172 Buneman, O. Computer-simulation using particles - HOCKNEY,RW, EASTWOOD,JW. *SIAM Rev.* **25**, 425-426, doi:10.1137/1025102 (1983).

173 Geuzaine, C. & Remacle, J.-F. Gmsh: A 3-D finite element mesh generator with built-in pre- and post-processing facilities. *International Journal for Numerical Methods in Engineering* **79**, 1309-1331, doi:10.1002/nme.2579 (2009).

174 Madauss, L. *et al.* Fabrication of nanoporous graphene/polymer composite membranes. *Nanoscale* **9**, 10487-10493, doi:10.1039/c7nr02755a (2017).

175 Cohen-Tanugi, D. & Grossman, J. C. Water permeability of nanoporous graphene at realistic pressures for reverse osmosis desalination (vol 141, 074704, 2014). *J. Chem. Phys.* **141**, doi:10.1063/1.4896215 (2014).